組成・構造制御した新規希土類マンガナイトの相状態のその場観察と機能発現の試み

（研究課題番号 18560662）

平成１８年度~１９年度科学研究費補助金　（基盤（c））

研究成果報告書

平成 20 年４月

研究代表者　　中野裕美

（龍谷大学理工学部電子顕微鏡室）

はしがき

本冊子は、平成 18 年度から 19 年度の 2 年間にわたり交付された、「組成・構造制御した新規希土類マンガナイトの相状態のその場観察と機能発現の試み」を研究課題とする科学研究費補助金　基盤（c）（研究課題番号 18560662）の研究成果報告書である。

研究期間に関わる２年間は、主に希土類マンガナイトやペロブスカイト関連構造を有する新規化合物を合成し、各温度における相状態や新規機能性発現を模索し、結晶構造と物性の関連性を議論してきた。酸化物合成においては、研究分担者である豊橋技術科学大学の亀頭直樹名誉教授や佐藤裕久助手および学生さんらにより進められ、いくつかの興味深い新規酸化物合成に成功した。それらの各温度での相状態を詳しく知るために、X線回折や電子回折等の機器分析による構造解析を行い、青井芳史講師には X 線光電子分光測定の協力を頂いた。そして、これまでに報告されていない新しい対称性の結晶構造を有することを明らかにし、論文にまとめることができた。また、層状ペロブスカイト構造を有する酸化物においては、高温透過型電子顕微鏡や高温 X 線回折を用いてその場観察を行い、これまでに報告例のない一次相転移を偶然見出すことができ、次年度の研究につながる新しい発見に心を躍らせている。

少人数の研究グループにあって、この２年間はグループ以外の共同研究者の方々にもご協力を頂いた。石沢伸夫教授（名古屋工業大学）には、精度の高い高温 X 線回折測定や構造解析に関する多大な助言を頂き、大変お世話になった。陶山容子教授（島根大学）や小林美学准教授（沼津高専）には新規酸化物の合成において、田中英彦博士（物質材料研究機構）には、高温での電子顕微鏡の動画から初期の粒子成長過程をモデル化する研究においてご尽力頂いた。その他にも、電子顕微鏡に関わる研究を通して沢山の研究者の方にご指導を頂き、新しい発見との出会いにわくわくしながら研究を進めることができた。

すてきな研究者の方々と共同研究ができ、ここに一定の成果をまとめられたことを心から喜び、感謝の意を表する。

平成 20 年４月吉日

龍谷大学理工学部
電子顕微鏡室
中野裕美

科学研究費補助金　（基盤（c））

期間：平成 18 年度から 19 年度

研究課題：組成・構造制御した新規希土類マンガナイトの相状態のその場観察と機能発現の試み

研究課題番号；18560662

研究代表者：中野裕美（龍谷大学理工学部実験講師）

研究分担者：佐藤裕久　（豊橋技術科学大学工学部助手）

研究分担者：青井芳史　（龍谷大学理工学部講師）

研究分担者：亀頭直樹　（豊橋技術科学大学工学部名誉教授）

研究経費：　平成 18 年度 1,400 千円

平成 19 年度 1,430 千円（内　間接経費 330 千円）

総合計 2,830 千円（内　間接経費 330 千円）

1. **Original papers**

Structure of new oxide $SrGdMnO_4$ H. Nakano, N. Ishizawa, N. Kamegashira, Zulhadjiri and T. Shishido, *J. Alloys and Compounds*. 408-412,（2006）593-597.

Crystal structure of a new compound $Er_2MnW_{0.8}O_{6.4}$ phase, G. Chen, Y. Imagawa, H. Satoh, H. Nakano, N. Kamegashira, *J. Alloys and Compounds*. 408-412,（2006）1230-1233.

Thermal diffusivity and phase transition of rare erath manganites, M. Kobayashi. H. Satoh, Y. Hiyoshi, N. Kamegashira, D.-J. Lee and H. –J. Kim, *Key Engineering Materials*, 321-323 (2006) 1695-98.

Phase behavior of layered manganites $BaLn_2Mn_2O_7$ (Ln = rare earth), H. Nakano, H. Satoh, N. Kamegashira, N. Ishizawa *Physica Status Solidi*（c） **3**(8) (2006) 2812-2815.

Thermal behavior of $BaTiO_3$ particles synthesized by prasma CVD" H. Nakano, K. Suzuki, K. Kizima, *J. Am. Ceram. Soc.* 89[4] (2006) 1461-1464.

Phase Behavior and Crystal Structure of Perovskite-Type Rare Earth Complex Oxides M. Kobayashi, M. Yamaguchi, R. Katsuraya, T. Nara, Y. Tomita, H. Nakano, N. Kamegashira, *J. Rare Earths* 24, (2006) 668-672.

Novel phase transition in $BaPr_2Mn_2O_7$, H. Nakano and N. Kamegashira *J. Rare Earths* 24**(**special**)**, (2006)1-3

Grain shrinkage driven by surface and grain boundary energy in $Ba_5Nb_4O_{15}$ powder, H. Tanaka, H. Nakano, Y. Suyama, *Acta Materialia* 55 (2007) 2423-32.

Saturation in degradation of thermal diffusivity of neutron-irradiated ceramics at 3×10^{26} n/m^2" M. Akiyoshi, T. Yano, Y. Tachi, H. Nakano, J. Nuclear Materials 367-370, (2007) 1023-1027.

In-situ transmission electron microscopy observation of multiple phase transitions in $BaGd_2Mn_2O_7$ H. Nakano, N. Ishizawa, N. Kamegashira, M. Yashima, *J. Am. Ceram. Soc*. 90(4) (2007) 1342-1345.

Microstructure of nano-porous $NaNbO_3$ particles synthesized by sol-crystal method H. Nakano, Y. Hirano, Y. Suyama, *J. The Society of Materials Science Jpn*. 56(6), (2007) 500-504.

Nano-domain twin structure formed by phase transition in new perovskite oxide $(Sr_{0.67}Sm_{0.33})(Mn_{0.33}Ti_{0.67})O_3$ H. Nakano, M. Kobayashi, N. Kamegashira, *J. Am. Ceram. Soc*. 90(4) (2007) 1276-1279.

Phase Transition of Gd_3RuO_7 From a structure of view, H. Nakano, K. Tateishi**,** N. Ishizawa,*セラミック基盤工学センター年報* Vol.7 (2007) 6-15

New phase of $BaLaMnO_{4-x}$ formed by annealing in a reducing atmosphere, H. Nakano, N. Kawabata, N. Kamegashira, *J. Ceram. Soc. Jpn.* 116(3) (2008) 361-364.

Stability of Phases in (Ba, Gd)MnO_3 Solid Solution, M. Kobayashi, H. Tamura, H. Nakano, H. Satoh and Naoki Kamegashira, *J Rare Earth* in press.

Structural analysis of new phase of $BaNdMnO_4$" Hiromi Nakano, Norikatsu Kawabata, Hirohisa Satoh, and Naoki Kamegashira *J Rare Earth* in press

Synthesis and Crystal Structure of a New Layered Carbide $[Zr_{1.97}Y_{0.03}]Al_4C_5$, Koichiro Fukuda, Miyuki Hisamura, Tomoyuki Iwata, Shinobu Hashimoto, and Hiromi Nakano, *J. Am. Ceram. Soc*. in press

2. Proceedings

Phase relation in double layered rare earth manganites" N. Kamegashira, J. Meng, H. Nakano, *proc. of 2nd China-Japan-Korea Joint symposium on new rare earth-related materials* ,Changchun, China, (2006) pp. 8.

Multiple phase transitions in $BaLn_2Mn_2O_7$ (Ln = rare earth), H. Nakano, Y. Aoi, N. Kamegashira, *Proc. of The 7th Korea-Japan joint workshop on advanced semiconducter process and equipments*, Nara, (2006) pp. 286-289.

Synthesis, Phase Behavior and Crystal Structure of Perovskite-Type Rare Earth Complex Oxides, N. Kamegashira, H. Nakano, M. Kobayashi, *Proc. of The 7th Korea-Japan joint workshop on advanced semiconducter process and equipments*, Nara, (2006) pp. 270-273.

On the formation of (Ba,Gd)MnO_3 solid solution in Air" N. Kamegashira, H. Naknao, M. Kobayashi, *Proc. of 2007 Korea-Japan Joint Workshop*, Busan, Korea, pp.292-295.

Phase Transition of Gd_3RuO_7 -From a structure of view-" N. Ishizawa, K. Tateishi and H. Nakano, *Proc. of 32nd annual Australian Condensed Matter and Materials Meeting, Australia*, Melbourne (2008) in press

3. 学会発表

Novel phase transition in $BaPr_2Mn_2O_7$, H. Nakano, N. Kamegashira, International conference on rare earth research and application (ICRERA) (Beijing, China) (2006 年 6/25-30)

Phase Behavior and Crystal Structure of Perovskite-Type Rare Earth Complex Oxides M. Kobayashi, M. Yamaguchi, R. Katsuraya, T. Nara, Y. Tomita, H. Nakano, N. Kamegashira, International conference on rare earth research and application (ICRERA) (Beijing, China) (2006 年 6/25-30)

層状ペロブスカイト構造を有する $BaLn_2Mn_2O_7$(Ln=希土類)の相転移その場観察 中野裕美、石沢伸夫、亀頭直樹　日本セラミックス協会　第 1 回関西支部学術講演会　（京都大）(2006 年 7 /20)

Phase relation in double layered rare earth manganites, N. Kamegashira, J. Meng, H. Nakano, 2nd China-Japan-Korea Joint symposium on new rare earth-related materials (Changchun, China) (2006)

Multiple phase transitions in $BaLn_2Mn_2O_7$ (Ln = rare earth), H. Nakano, Y. Aoi, N. Kamegashira, The 7th Korea-Japan joint workshop on advanced semiconducter process and equipments, (Nara, Japan) (2006,11/16)

Synthesis, Phase Behavior and Crystal Structure of Perovskite-Type Rare Earth Complex Oxides, N. Kamegashira, H. Nakano, M. Kobayashi, The 7th Korea-Japan joint workshop on advanced semiconducter process and equipments, (Nara, Japan) (2006,11/16)

相転移により形成されたナノツイン構造　中野裕美、小林美学、亀頭直樹、第57回金属組織写真賞作品展　（2006年）

ナノスケールの双晶構造を有する$(Sr_{0.67}Ln_{0.33})(Mn_{0.33}Ti_{0.67})O_3$ (Ln = 希土類)のTEMによる相転移その場観察、中野裕美、　桂谷涼子　小林美学、亀頭直樹、50回日本学術会議材料光学連合講演会　（京大会館）　（2006年12/13）

$(A_{0.67}Ln_{0.33})(Mn_{0.33}Ti_{0.67})O_3$ (A: Sr or Ca, Ln = 希土類)の構造と相転移、　中野裕美、　沼津高専、桂谷涼子、小林美学、亀頭直樹、日本セラミックス協会年会（武蔵工業大）（2007年3/21-23）

新奇なナノポーラス $NaNbO_3$ 粒子　中野裕美、陶山容子、日本セラミックス協会写真展　（武蔵工業大）（2007年3/21-23）

層状ペロブスカイト型マンガン酸化物の一次相転移その場観察、中野裕美、石沢伸夫、亀頭直樹、日本顕微鏡学会63回学術講演会　（朱鷺メッセ）　（2007年5/20）

Stability of Phases in (Ba, Gd)MnO_3 Solid Solution, M. Kobayashi, H. Tamura, H. Nakano, H. Satoh and Naoki Kamegashira、The fifth international conference on rare earth development and application (Baotou, China) (2007, 8/7-11)

Structural analysis of new phase of $BaLnMnO_4$ (Ln = La, Nd), H. Nakano, N. Kawabata, H. Satoh, and N. Kamegashira、The fifth international conference on rare earth development and application (Baotou, China) (2007, 8/7-11)

Roles of Rare-Earth Oxide Additives in Millimeter-Wave Sintering of AlN and Si_3N_4, Y. Makino, T. Yoshioka, H. Nakano, T. Ueno and S. Miyake, The fifth international conference on rare earth development and application (Baotou, China) (2007, 8/7-11)

層状ペロブスカイト型$BaPr_2Mn_2O_7$の高温構造変化、近藤早、石澤伸夫、中野裕美、日本セラミックス協会秋季シンポジウム　(名古屋工業大学)　（2007年 9/12-14）

TEM によるミリ波焼結セラミックスの微構造の特徴、中野裕美、巻野勇喜雄、日本セラミックス協会秋季シンポジウム、(名古屋工業大学)　（2007年　9/12-14）

On the formation of (Ba,Gd)MnO_3 solid solution in Air, N. Kamegashira, H. Naknao, M. Kobayashi, 2007 Korea-Japan Joint Workshop, (Busan, Korea) (2007,10/4-6)

層状ペロブスカイト型希土類マンガナイト相の相挙動, 佐藤裕久、川畑勝範、荒木幹昌、大串達夫、亀頭直樹、中野裕美、宍戸統悦、中嶋一雄, 中部化学関係学協会支部連合協議会 (三重大学)　（2007,11/10-11）

$Ln(Mn,B)O_3$ の合成と構造解析（Ln=希土類、B=Al,Ga）, 奈良翼、小川洋平、佐藤裕久、大串達夫、亀頭直樹, 中部化学関係学協会支部連合協議会 (三重大学)　（2007,11/10-11）

Ln_3RuO_7(Ln=Gd,Tb,Dy)の相転移、近藤早、石澤伸夫、中野裕美、第46回セラミックス基礎科学討論会　（名古屋工業大）（2008年1/10-11）

新化合物$(Ca,Nd)_{11}Ru_4O_{24}$の合成と構造、岡田敬太、石澤伸夫、中野裕美、第46回セラミックス基礎科学討論会　（名古屋工業大）（2008年1/10-11）

層状ペロブスカイト $BaGd_2Mn_2O_7$ の一次相転移のその場観察、中野裕美、石沢伸夫、亀頭直樹、日本セラミックス協会年会写真展 （長岡技術科学大）（2008、3/20-22）

$BaLn_2Mn_2O_7$ の一次相転移のその場観察、中野裕美、石沢伸夫、亀頭直樹、日本セラミックス協会年会 （長岡技術科学大）（2008、3/20-22）

層状ペロブスカイト $BaGd_2Mn_2O_7$ の一次相転移その場観察 –高温相出現から単一相に至までの変化— 中野裕美、石沢伸夫、亀頭直樹 日本セラミックス協会写真展 （長岡技術科学大）（2008、3/20-22）

4. **招待講演**

高熱伝導セラミックスの熱伝導率に及ぼす微構造の影響、○中野裕美、第 1 回 EMAP 研究会 （大阪大学 2006.7.21）

電子顕微鏡による結晶質無機材料のキャラクタリゼーション –材料開発のためのキーワード- ○中野裕美、（村田製作所材料開発センター 2006.11.10）

ミリ波焼結 Al_2O_3 の TEM による微構造解析、○中野裕美、巻野勇喜雄、佐野三郎、粉末冶金秋季大会 （大阪大）（2006 年 12/5）

$Ba_5Nb_4O_{15}$ 粉末におこる小粒子の消滅 ○田中英彦、中野裕美、陶山容子、日本セラミックス協会秋季シンポジウム、(名古屋工業大学) （2007 年 9/12-14）

透過型電子顕微鏡（ＴＥＭ）によるナノワールド –ナノ構造から得られる材料設計のためのキーワード-、 ○中野裕美（横浜国大 2007 年 11/1）

First-Order Phase Transition of Gd_3RuO_7 at High Temperature, ○N. Ishizawa, H. Nakano, 32 nd Annual condensed mater and materials meeting, (Melbourne, Australia) (2008,1/30-2/1)

5. 解説、著書等

解説:高強度を示したミリ波焼結アルミナのTEMによる微構造解析　中野裕美、巻野勇喜雄、粉末冶金　54(8) (2007)　549-555

解説：原子をみる・さぐる　–TEM でなぜ原子が見えるのか-　中野裕美、化学と教育 56 巻 5 号　(2008)

解説:ミクロの世界を見る　–電子顕微鏡写真から得られる多彩な情報-　中野裕美　龍谷理工ジャーナル Vol.20(1)（2008）19-24

著書：希土類の材料技術、　第 1 部　10.2　「エンジニアリングセラミックスの特性に及ぼす希土類焼結助剤の添加効果と微構造」中野裕美、渡利広司　シー.エム.シー出版　印刷中

著書:次世代構造材料の最新の研究開発と社会・産業へのインパクト 4.4.1　「高熱伝導率セラミックスの最近の進歩」渡利広司、粂正市、山田伊久子、中野裕美　シー.エム.シー出版　印刷中

著書：　希土類の機能と応用、第 9 章-2　「エンジニアリングセラミックスと希土類助剤」シー.エム.シー出版　渡利広司、中野裕美（pp. 302-311）(2006)　印刷中

研究成果の概要

イ　K_2NiF_4型構造を有する希土類マンガナイトの新相の探求

$BaLnMnO_4$ (Ln = Nd, La)について、フローティングゾーン法により、K_2NiF_4構（*I*4/*mmm* tetragonal）を有する単結晶を作成することに成功した。その後、還元雰囲気下で熱処理を行うことにより、新相が発現した。$BaNdMnO_4$については、3%H_2-Ar気流中で、573Kで240時間熱処理後急冷することにより斜方晶（*Fmmm*）に変化した。また、$BaLaMnO_4$については、1%-H_2-Ar気流中で773Kで168時間熱処理後急冷により、斜方晶（*Cccm*）が発現した。この変化は、還元雰囲気下での熱処理により、Mn^{3+}の一部がMn^{2+}に還元され、このため酸素欠損による不定比性により発現したことを、TEM-EELS分析やICPによる元素分析の結果から明らかにした。La系のほうがNd系に比べてより対称性が低くなったのは、La系のほうは酸素欠損量が多くても相が安定しやすく、このためMnO_6八面体の傾斜が大きくなり、結晶の対称性が低下したと結論づけた。

ロ　ペロブスカイト型関連構造を有する酸化物の新相の探求と物性評価

$(A_{0.67}Ln_{0.33})(Mn_{0.33}Ti_{0.67})O_3$ (A: Ca, Sr, Ln: rare erath)をAr雰囲気下で合成し、単相を得ることに成功した。Ca系については、LaからYbまでの希土類で合成できたが、Sr系については、Gd以下のイオン半径の小さい希土類では単相を得ることができなかった。陽イオンのクーロンポテンシャルの計算から電気特性との関連性を議論した。またSr系では、La以外ではCa系と同様の斜方晶*Pnma*を有する結晶構造であったが反射強度が弱く、このことは、Srのイオン半径が大きくこのためセルサイズが大きくなたったためである。またSr系では多くのナノサイズのドメイン形成が観察され、冷却過程内での構造相転移が示唆された。このため高温TEMによる相転移を観察した結果、Smについては、723K以上で*Pnma*から*Imma*への相転移を見出すことができた。このことから他のSr系希土類でも同様の相転移の可能性が示唆され、相転移温度と希土類のイオン半径、Mn-O角度、トーレランスファクター（t-因子）と電気伝導度との相関性について議論し今後の新酸化物設計において指針を得ることができた。

これ以外のペロブスカイト関連化合物においても、新規データが出つつあり、現在も研究を継続中である。

ハ　高温測定による相状態のその場観察

上述したようにペロブスカイト構造を有するマンガナイトは、酸素八面体の傾斜に基づいた結晶構造を有しており、一般に高温では対称性の高いの結晶構造へ相転移を起こすことが知られている。今回、高温 TEM によるその場観察を行い、相転移挙動をリアルタイムで撮影することに成功し、希土類イオン半径、Mn-O 距離、角度との相関性を議論した。またこれらの相転移の中には電気伝導度データには現れないような微小回転に基づくものも多く、高温 TEM の精度の高さを実感した。

層状構造を有するペロブスカイト $BaLn_2Mn_2O_7$ については、構造相転移を利用し、熱処理温度により多彩な構造を有する酸化物の合成に成功してきた。これまでにも高温 XRD や電気伝導度、熱分析による相転移が観察され議論がなされてきた。今回高温 TEM によるその場観察の結果、これまでに報告例のない一次相転移を高温域で起こすことを偶然見出した。通常、酸素八面体の傾斜にもとづく相転移の場合、高温では対称の良い結晶構造に相転移をする。しかし、$BaGd_2Mn_2O_7$ については、orthorhombic-tetragonal-monoclinic と相転移を起こし、特に、tetragonal-monoclinic への相転移は一次相転移であることを見出した。これは、*c*-面に平行に岩塩構造とペロブスカイト構造が交互に形成しており、面間のひずみや電子構造と関連し、*c*-軸が大きく伸びた構造が層状に入り込み、一定の時間を経て高温相に変化する過程を動画でも記録することができた。また、この結果を受けて、$BaPr_2Mn_2O_7$ の酸素八面体が傾斜していない層状構造でも明らかに 1040 K で一次相転移を起こすことを高温 TEM により明らかにした。$BaPr_2Mn_2O_7$ の場合、5〜10 分間程度の短い時間において *c*-軸方向の反射がスプリットし、これは *c*-軸長の 1.5%長い高温相が出現したことを意味した。従って、この相転移は明らかに通常報告されている酸素八面体の傾斜による逐次相転移とは性格の異なるものである。他の希土類においても同様の一次相転移を起こす可能性が示唆され、今後電子構造や、Mn 価数の揺動など精密な高温 XRD 測定結果と合わせてさらに研究を展開する予定である。

層状構造を有する Gd_3RuO_7 については、一次相転移の際に出現した中間相（サテライト反射）を高温 TEM により観察することに成功し、この中間相の詳細な検討と他の希土類系での相転移を含め、今後の研究課題としたい。

新規希土類マンガナイトの構造、機能性、および相転移に関する研究成果

Journal of the Ceramic Society of Japan 116 [3] 445-448 2008 Paper

New phase of $BaLaMnO_{4-x}$ formed by annealing in a reducing atmosphere

Hiromi NAKANO,† Norikatsu KAWABATA* and Naoki KAMEGASHIRA*

Ryukoku University, Seta, Otsu 520-2194
*Toyohasi University of Technology, Tenpaku-cho, Toyohashi 441-8580

A single crystal of $BaLaMnO_4$ with $I4/mmm$ has been synthesized by a floating zone method. A new phase of $BaLaMnO_{4-x}$ was obtained by annealing the single crystal in a reducing atmosphere at 773 K for 168 h. The structural change was analyzed by four-circle X-ray diffractometry (XRD) and transmission electron microscopy (TEM). The new phase has an orthorhombic unit cell ($Cccm$) of $a=0.5504(7)$ nm, $b=0.5502(5)$ nm, and $c=1.3265(1)$ nm. The structural change from $I4/mmm$ into $Cccm$ was caused by an oxygen deficiency, and a small amount of Mn^{2+} ions was formed by annealing in a reducing atmosphere.

Key-words : Rare earth manganite, Structure, Transmission electron microscopy, X-ray diffractometry, Nonstoichiometory

[Received December 11, 2007; Accepted January 17, 2008]

1. Introduction

Compounds of $Ba_{1+x}Ln_{1-x}MnO_4$ (Ln = La and Nd) with the K_2NiF_4-type structure were first synthesized by Benabad *et al.*.[1] The cell size of the *c*-axis elongates due to the Jahn-Teller effect of the Mn^{3+} ion. Therefore, the cell size of the *c*-axis is the longest when the *x* value is 0. The oxygen non-stichiometry of $BaNdMnO_{4+x}$ was investigated and, consequently, limited to $x=0.17$.[2] A poly-crystalline structure of $BaPrMnO_4$ was first synthesized by Ueno *et al.*.[3] These oxides possess a tetragonal structure with a space group of $I4/mmm$. Single crystals of $BaLnMnO_4$ (Ln = rare earth) were synthesized for the first time in an Ar atmosphere by a floating zone (FZ) method by Kamegashira *et al.*.[4] The phases also have a tetragonal structure (K_2NiF_4-type) with $I4/mmm$.

Recently, a new phase of $BaNdMnO_4$ with an orthorhombic structure ($Fmmm$) was synthesized by annealing the single crystal in a reducing atmosphere (3%H_2-Ar flow) at 523 K.[5] The structural change is related to an oxygen deficiency. In this study, a new phase of $BaLaMnO_4$ was successfully synthesized by annealing in a 1%H_2-Ar flow at 723 K. Structural change from a tetragonal to an orthorhombic form was analyzed by using four-circle X-ray diffractometry (XRD) and transmission electron microscopy (TEM). The TEM data revealed that this crystal symmetry was lower than that of $BaNdMnO_4$.

2. Experimental procedure

Starting materials of high-purity (99.9%) $BaCO_3$, La_2O_3, and Mn_2O_3 underwent heat treatment for purification before weighing.[5] These materials were mixed in an agate mortar and pressed. The pellet was heated at 1073 K in Ar for 24 h and subsequently at 1723 K in Ar for 72 h. The obtained product was confirmed by XRD to be a single phase of poly-crystalline $BaLaMnO_4$. The product was placed in a floating zone (FZ) furnace equipped with a bi-ellipsoidal halogen lamp. The detailed procedure is described elsewhere.[4] The single crystal was annealed in a 1% H_2-Ar flow at 773 K for 168 h and then quenched.

The chemical ratio of Ba, La and Mn was measured by inductively coupled plasma (ICP). The oxygen deficiency was measured by titration analysis and calculated from the ICP result.

The structure of the crystal was analyzed by four-circle XRD (Rigaku-AFC7R, Tokyo) using the software Shelx 97. The crushed specimen was scooped with carbon-coated copper microgrids for TEM observation. The TEM observation was performed using a high-resolution TEM at 300 kV (JEOL-3000F, Tokyo). Electron energy-loss spectroscopy (EELS) was performed by using a TEM device (JEOL 2000F equipped with GIF).

3. Results and discussion

The structure of the annealed crystal $BaLaMnO_4$ was analyzed by TEM. **Figure 1** shows selected area electron diffraction (SAED) patterns taken from the [001] zone axis for as-grown crystal in (a) and annealed crystal in (b). We found a difference in those SAED patterns, as shown by the extra reflections detected in the annealed crystal in (b). The cell parameter of $a \approx b = 0.550$ nm for annealed crystal is larger by 1.41 times than that of as-grown crystal. Typical

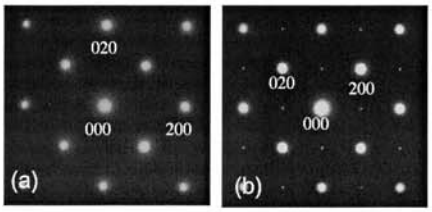

Fig. 1. SAED patterns of $BaLaMnO_4$ (a) as-grown crystal and (b) annealed crystal.

† Corresponding Author; E-mail: hiromi@rins.ryukoku.ac.jp

SAED patterns of the annealed crystal are shown in **Fig. 2** (a)–(c), which were taken from the [101], [121] and [301] zone axes, respectively. The reflections with strong intensities satisfy a condition for *Fmmm* symmetry as reported for $BaNdMnO_4$.[5] However, the SAED pattern in Fig. 1 (b) indicates the presence of 110 reflections with weak intensities, and this does not conform to the *Fmmm* symmetry that excludes the $hk0$ reflections with h, k odd. The 100, 010 $10\bar{1}$, $01\bar{2}$ reflections were not observed in Fig. 1 (b) and 2. These results disagree with the $P4_2/ncm$ symmetry reported for $La_{0.875}Ba_{0.125}CuO_4$,[6] *Cmca* symmetry for $La_{1.91}Sr_{0.09}CuO_{4.12}$,[7] *Pccm* symmetry for $SrGdMnO_4$[8] and $La_{0.9}Ba_{0.1}CuO_4$,[9] and *Pccn* symmetry for $La_2CuO_{3.98}$.[10] These extinction rules uniquely lead to *Cccm* as a possible space group for annealed crystal of $BaLaMnO_4$. The orthorhombicity of the crystal was measured by four-circle XRD. The refinement was carried out using crystal structures with some possible space groups. The XRD result shows that the crystal structure with *Fmmm* symmetry had a lowest value (4.98%) of the reliability factor based on the integrated intensity R_I. The reason for this is that the weak reflections caused by *Cccm* symmetry could not be detected by XRD measurement. The refined atomic parameters based on *Ccmm* symmetry are shown in **Table 1**. Ba and La ions randomly occupied the 8*k* site in the orthorhombic structure with *Cccm* symmetry. The reliability factor R_I is 7.06%, and the goodness of fit S is 1.371 but anisotropic displacement parameters were not reasonable values. The crystal symmetry is related to the octahedral distortion of layered perovskite K_2MgF_4, found by Alksandrov.[11] The relationship between $I4/mmm$ and *Cccm* was described by the distortion of (Mn, Ti)O_6 octahedra as 000 and $\phi\phi0$, respectively. The rotations of ϕ type are characterized by alternating signs of the rotations around the rotation axis.[11]

Figure 3 shows high-resolution TEM (HRTEM) images taken from the [110] and [001] axes. The periodic distance of 0.67 nm is the (002) spacing along the *c*-axis. In Fig. 3 (b), weak periodicity of about 0.4 nm was observed, which is (110) spacing. This periodicity clearly shows that the phase has a new structure.

This structural change from tetragonal ($I4/mmm$) to orthorhombic (*Cccm*) form might have been caused by the oxygen deficiency during annealing for a long time in a reducing atmosphere. The nonstichiometry of the as-grown crystal and the annealed crystal were measured by chemical analysis. The chemical compositions are $Ba_{0.966}La_{1.005}Mn_{1.000}O_{3.9774}$ and $Ba_{0.966}La_{1.005}Mn_{1.000}O_{3.898}$ for as-grown crystal and annealed crystal, respectively. The oxygen deficiency is relat-

Table 1. Atomic Parameters of Annealed Crystal $BaLaMnO_4$

atom	site	*x*	*y*	*z*
Ba/La	8*k*	0.25	0.25	0.35725(1)
Mn	4*e*	0.25	0.25	0
O1	4*c*	0	0	0
O2	4*d*	0	0.5	0
O3	8*k*	0.25	0.25	0.17046(7)

Space group: *Cccm* R_I 7.06 % S 1.371

Lattice parameters : a = 0.5504(7) nm, b = 0.5502(5) nm, c = 1.3265(1) nm

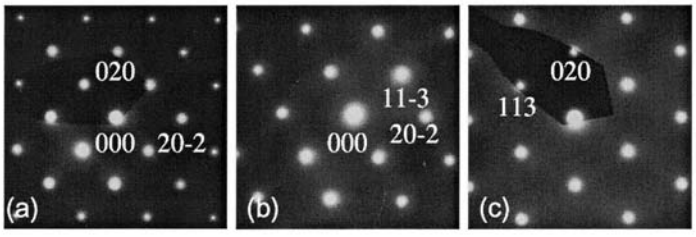

Fig. 2. SAED patterns of annealed crystal of $BaLaMnO_4$ taken from (a) [101], (b) [121], and (c) [301].

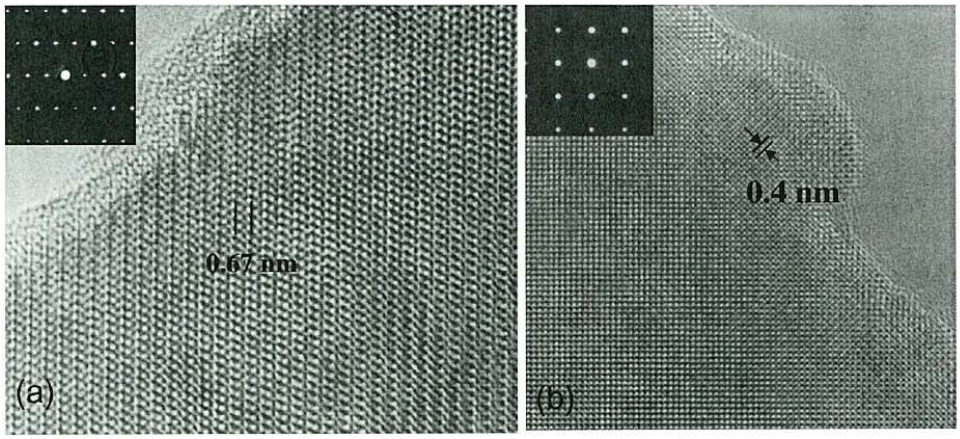

Fig. 3. High-resolution TEM images of annealed crystal $BaLaMnO_4$ taken from [110] zone axis in (a) and [001] in (b).

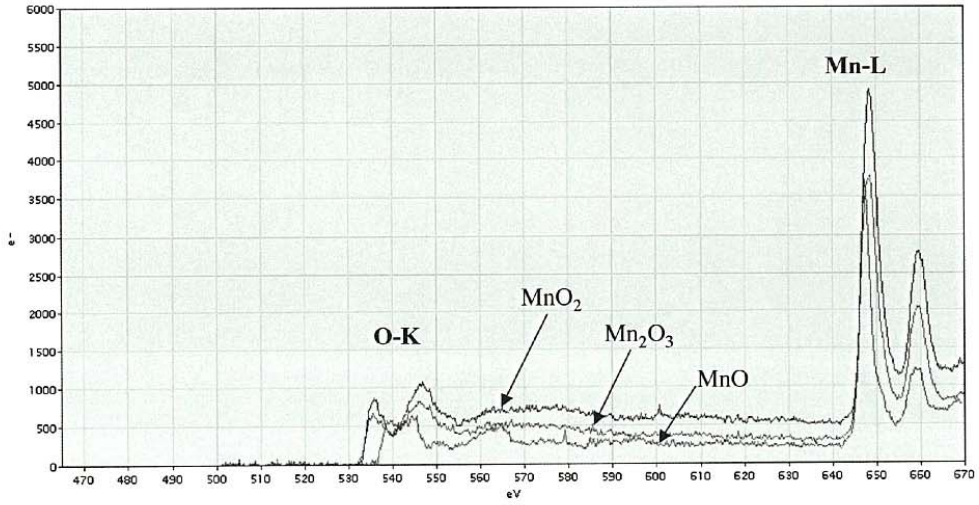

Fig. 4. EELS peaks of standard materials MnO, Mn_2O_3 and MnO_2.

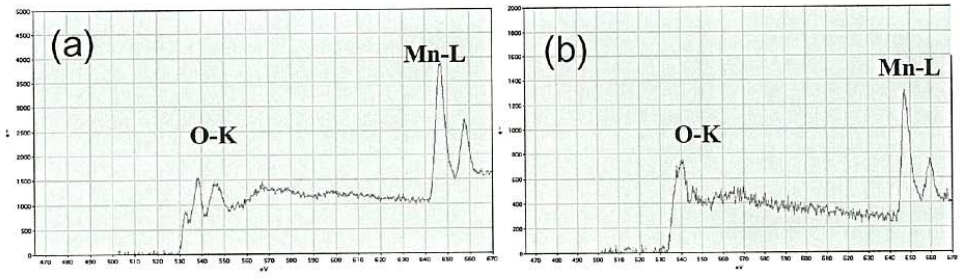

Fig. 5. EELS peaks of $BaLaMnO_4$ (a) As-grown crystal and (b) annealed crystal.

ed to the valence of the Mn ion. When the Mn oxidation state changes from trivalent to divalent, an oxygen defect would occur during the annealing. It was calculated that 15% of Mn^{3+} ions changed into Mn^{2+} ions by annealing. **Figure 4** shows EELS peaks of standard materials MnO, Mn_2O_3, and MnO_2. The two peaks of the O-K line at 535 eV and 545 eV were detected for Mn_2O_3 and MnO_2, respectively, and no difference in the oxidation state between Mn^{3+} and Mn^{4+} could be observed. On the other hand, one broad peak of O-K was detected at around 540 eV for MnO, and the oxidation state of Mn^{2+} was confirmed. **Figure 5** shows EELS peaks of as-grown crystal and annealed crystal of $BaLaMnO_4$. The O-K line peak was affected by Ba-O and La-O bonding in $BaLaMnO_4$. However, the difference between (a) and (b) for EELS peak of O-K line was caused by the oxidation state of Mn ion. We found the existence of Mn^{2+} ion in the partially grain of $BaLaMnO_4$. Our findings also indicate that the nonstoichiometry of the annealed crystal was caused by a reduction in Mn ions to some extent.

Finally, the structural change from *I*4/*mmm* to *Cccm* was related to the nonstoichiometry of $BaLaMnO_{4-x}$ due to oxygen deficiency. In addition to the octahedral tilting, the Jahn-Teller (J-T) distortion occurred in the case of $Mn^{3+}O_6$. This effect manifested itself in the changes in unit cell size and c/a ratio of $Sr_{1+x}La_{1-x}MnO_4$ ($0<x<1$).[1] This sort of J-T distortion may contribute slightly to the symmetry changes from tetragonal to orthorhombic. Therefore, the appearance of weak reflections on the a^*-b^* plane is assumed to be related to the tilting of MnO_6 octahedra.[11]

4. Conclusion

We successfully synthesized a new phase of $BaLaMnO_{4-x}$ by annealing in a reducing atmosphere. A structural characterization was performed using four-circle X-ray diffractometry (XRD) and transmission electron microscopy (TEM) equipped with electron energy-loss spectroscopy (EELS). The presence of extra reflections with weak intensities was detected on the a^*-b^* plane, and the extinction rule led to *Cccm* as a possible space group. The orthorhombicity was measured by XRD analysis, where the cell parameters were a = 0.5504(7) nm, b = 0.5502(5) nm, and c = 1.3265(1) nm. The structural change from *I*4/*mmm* to *Cccm* was related to the nonstoichiometry of $BaLaMnO_{4-x}$ due to oxygen deficiency. This nonstoichiometry was caused by a reduction in Mn ions during annealing in the reducing atmosphere. Furthermore, the EELS data revealed the existence of Mn^{2+} ion in the annealed crystal of $BaLaMnO_4$.

Acknowledgements This work was partially supported by a Grant-in Aid for Scientific Research (c) No. 18560662 from the Japan Society for the Promotion of Science. We thank Dr. T. Oikawa of JEOL Ltd. for his help with the EELS analysis and Dr. H. Satoh of Toyohashi University of Technology for his suggestion.

References

1) A. Benabad, A. Daoudi and R. Salmon and G. Leflem, *J. Solid State Chem.*, 22, 121-126 (1977).
2) N. Kamegashira, S. Ueno, H. Nakano and K. Enami, *Mater. Res. Bull.*, 29(2), 185-193 (1994).
3) S. Ueno, K. Iwasaki, N. Kamegashira and H. Nakano, *Mater. Chem. Lett.*, 42, 201-205 (1995).
4) N. Kamegashira et al. "Synthesis of single crystal of $BaLnMnO_4$ (Ln = rare earth)" in preparation.
5) H. Nakano, N. Kawabata, H. Satoh and N. Kamegashira "Structural analysis of a new phase of $BaNdMnO_4$," Journal of Rare Earth (in press).
6) S. Katano, J. A. Fernadez-Baca, S. Funahashi, N. Mori, Y. Ueda and K. Koga, *Physica C* (Amsterdam), 214, 64-72 (1993).
7) C. Rial, U. Amador, E. Moran, M. A. Alario-Franco and N. H. Andersen, *Physica C* (Amsterdam), 234, 237-248 (1994).
8) H. Nakano, N. Ishizawa, N. Kamegashira, Zulhadjri and T. Shishido, *J. Alloys and Compounds*, 408-412, 593-597 (2006).
9) Y. Hirorsu, S. Nagakura, Y. Murata, T. Nishihara, M. takata and T. Yamashita, *Jpn. J. Appl. Phys.* Part 2, 26, 380-82 (1987).
10) K. Yamada, E. kudo, Y. Endoh, K. Tsuda, M. Tanaka, K. kokusho, H. Asano, F. Izumi, M. Oda, Y. Hidaka and M. Suzuki, *Jpn. J. Appl. Phys.* Part 1, 27, 1132-37 (1998).
11) K. S. Aleksandrov, *Sov. Phys. Crystallogr.*, 32(4), 551-555 (1987).

JOURNAL OF RARE EARTHS
Vol.25, Spec. Issue, Dec. 2007, p.1

Structural Analysis of a New Phase of $BaNdMnO_4$*

Hiromi Nakano[1*], Norikatsu Kawabata[2], Hirohisa Satoh[2], Naoki Kamegashira[2]
(*1. Ryukoku University, Seta, Otsu, 520-2194, Japan; 2. Toyohasi University of Technology, 441-8580, Japan*)

Abstract: Single crystal of $BaNdMnO_4$ with *I4/mmm* was synthesized by a floating zone method. A new phase of $BaNdMnO_4$ was obtained by annealing the single crystal in a reducing atmosphere at 573 K for 10 d. The structural change was analyzed by four-circle X-ray diffractometry and transmission electron microscopy. The new phase has an orthorhombic unit cell (*Fmmm*) of $a = 0.5486(2)$ nm, $b = 0.5484(2)$ nm, and $c = 1.3059(2)$ nm.

Key words: rare earth manganite; structure; transmission electron microscopy; X-ray diffractometry
CLC number: O614.33 **Document code:** A **Article ID:** 1002 - 0721(2007) - 0001 - 03

Compounds of $Ba_{1+x}Ln_{1-x}MnO_4$ (Ln = La and Nd) with the K_2NiF_4-type structure were first synthesized by Benabad et al.[1]. The cell size of the *c*-axis elongates due to the Jahn-Teller effect of the Mn^{3+} ion. Therefore, the cell size of the *c*-axis is the longest when the *x* value is 0. The oxygen nonstichiometry of $BaNdMnO_{4+x}$ was investigated and, consequently, limited to $x = 0.17$[2]. A poly-crystalline structure of $BaPrMnO_4$ was first synthesized by Ueno et al.[3]. These oxides possess a tetragonal structure with a space group of *I4/mmm*.

Recently, single crystals of $BaLnMnO_4$ (Ln = rare erath) were synthesized for the first time in an Ar atmosphere by a floating zone (FZ) method by Kamegashira et al[4]. The phases also have a tetragonal structure (K_2NiF_4-type) with *I4/mmm*. In the present study, a new phase of $BaNdMnO_4$ with an orthorhombic structure was successfully synthesized by annealing the single crystal in a reducing atmosphere. Structural characterization of the oxide was performed using four-circle X-Ray Diffractometry (XRD) and Transmission Electron Microscopy (TEM).

1 Experimental

Starting materials of high-purity (99.9%) $BaCO_3$, Nd_2O_3, and Mn_2O_3 underwent heat treatment for purification before weighing. These materials were mixed in an agate mortar and pressed. The pellet was heated at 1073 K in Ar for 24 h and subsequently at 1723 K in Ar for 72 h. The obtained product was confirmed by XRD to be a single phase of polycrystalline $BaNdMnO_4$. The product was placed in a floating zone (FZ) furnace equipped with a bi-ellipsoidal halogen lamp. The detailed procedure has been described elsewhere[4]. The single crystal was annealed in a 3% H_2-Ar flow at 573 K for 10 d and then quenched.

The structure of the crystal was analyzed by four-circle XRD (Rigaku-AFC7R, Tokyo, Japan) using the software Shelx 97. The crushed specimen was scooped with carbon-coated copper microgrids for TEM observation. The specimen's microstructure was characterized at high-resolution TEM (JEM-3000F, JEOL, Tokyo) operating at 300 kV with spherical aberration of Cs = 1.0 nm (0.19 nm theoretical resolution, -53.3 nm Sherzer focus). The HRTEM images were calculated with a Macintosh computer and the calculation program Mac Tempas (Total Resolution, Inc., U.S.A.).

2 Results and Discussion

The structure of the annealed crystal of $BaNdMnO_4$ was analyzed by four-circle XRD. The crystal had an orthorhombic structure with a space group of *Fmmm* (69), and cell parameters were $a = 0.5486(2)$ nm, $b = 0.5484(2)$ nm, and $c = 1.3059(2)$ nm. The atomic parameters are refined and shown in Table 1. Ba and Nd ions randomly occupied the 8i site. The reliability factor based on the integrated intensity RI is 5.8%, and goodness S is 1.286. Fig.1 shows a structural model constructed by the atomic parameters. The bond angles of O1-Mn-O1 and O1-Mn-O2 are 180 degrees and 90 degrees, respectively. On

* **Received date:** 2007 - 08 - 15; **revised date:** 2007 - 12 - 25
Foundation item: Project supported by a Grant-in Aid for Scientific Research (c) (18560662) from the Japan Society for the Promotion of Science
Biography: Hiromi Nakano, Doctor
* **Corresponding author** (E-mail: hiromi@rins.ryukoku.ac.jp)

Table 1 Atomic parameters of $BaNdMnO_4$

Atom	Site	x	y	z
Ba/Nd	8i	0	0	0.35672(3)
Mn	4a	0	0	0
O1	8i	0	0	0.164(1)
O2	8e	0.25	0.25	0

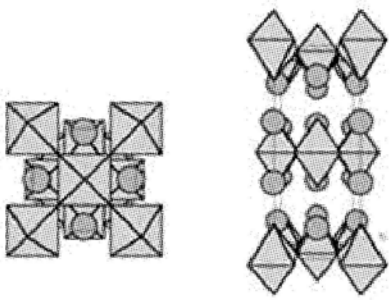

Fig. 1 Structural model of $BaNdMnO_4$ (spheres are Ba or Nd ion and octahedra are MnO_6)

the other hand, the bond angles of O2-Mn-O2 are 90.02 degrees and 89.98 degrees, and distortion was caused by the difference in parameters between the a-axis and b-axis. The bond lengths of Mn-O1 and Mn-O2 are 0.214 and 0.1938 nm, respectively. This difference in the bond length was caused by the Jahn-Teller effect in Mn^{3+} ion.

Fig. 2 shows selected area electron diffraction (SAED) patterns of $BaNdMnO_4$, which were taken from [001], [100], [110] and [031] zone axes. The reflections with strong intensities satisfy a condition for *Fmmm* symmetry. No other extra reflections appeared, as seen in $SrGdMnO_4$ with *Pccm*[5]. Compounds of $(La, Sr)_2MO_4$ (Ln = La, M = Cu, Ni) with K_2NiF_4-type structure have been investigated by some scientists, and various types of structures have been reported[6-8]. A similar structure to the orthorhombic (*Fmmm*) one was reported in $La_{1.76}Sr_{0.24}NiO_4$[8].

High-resolution TEM (HRTEM) images were taken from the [100] and [110] axes as shown in Figs. 3 and 4, respectively. Insets are SAED patterns and simulated images. The calculations were carried

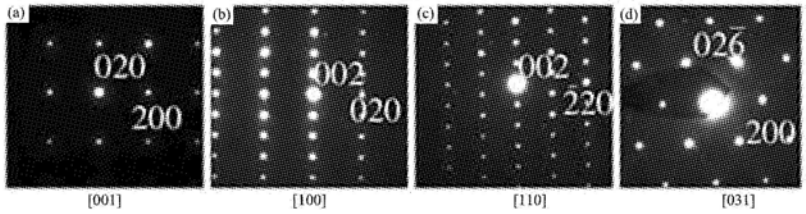

Fig. 2 Selected area electron diffraction patterns of $BaNdMnO_4$ taken from [001](a), [100](b), [110](c) and [031](d)

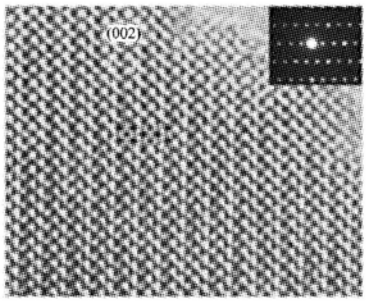

Fig. 3 High-resolution TEM images of $BaNdMnO_4$ taken from the [110] zone axis (insets are SAED pattern and simulated image)

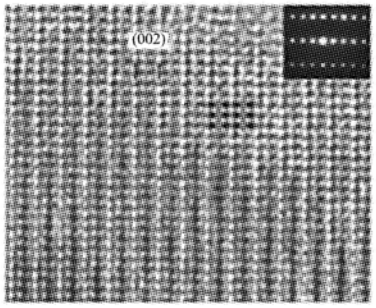

Fig. 4 High-resolution TEM images of $BaNdMnO_4$ taken from the [100] zone axis (insets are SAED pattern and simulated image)

out using the atomic parameters in Table 1. The film thickness was estimated to be 2 nm, by comparison of the observed images with calculated ones for different thickness. The simulated images at $\Delta f = -35$ nm along the [100] and [110] axes are demonstrated in Figs. 3 and 4, respectively. These calculated images were in good agreement with the observed images. These SAED data and HRTEM images supported the XRD results. In the case of the polycrystalline structure of $BaNdMnO_4$[2] and $BaPrMnO_4$[3], many stacking disorders were observed along the c-axis. The disorders were easily formed by the insertion of a layered perovskite $BaLn_2Mn_2O_7$ caused by the sublimation of BaO during heating. No stacking disorder was observed in the HRTEM image, and no streaks appeared in the SAED pattern (Fig.3). The present study used a single crystal, which was produced by the addition of excessive $BaCO_3$ to avoid the sublimation of BaO.

The structural change from *I4/mmm* into *Fmmm* might be related to the nonstoichiometry. The structural distortion could have been caused by an oxygen deficiency in the $BaNdMnO_{4-x}$ through annealing for a long time in the reducing atmosphere. Similar structural change occurred in $BaLaMnO_4$, while the symmetry was lower than that of $BaNdMnO_4$. The lower symmetry of $BaLaMnO_{4-x}$ was made by a larger distortion with a larger value of x. The detailed results of $BaLaMnO_4$ will be reported elsewhere[9].

3 Conclusion

We successfully synthesized a new phase of $BaNdMnO_4$ by annealing in a reducing atmosphere. A structural analysis was performed using four-circle X-ray diffractometry (XRD) and transmission electron microscopy (TEM). The new phase was found to have an orthorhombic structure with *Fmmm* (69), whose cell parameters were $a = 0.5486(2)$ nm, $b = 0.5484(2)$ nm, and $c = 1.3059(2)$ nm. The electron diffraction data also supported the XRD results, and the reflection conditions permitted Fmmm symmetry. Finally, we found that the structural change from *I4/mmm* into Fmmm was related to the nonstoichiometry of $BaNdMnO_{4-x}$ due to oxygen deficiency.

References:

[1] Benabad, A, Daoudi A, Salmon R, and Leflem G. Les phases $SrLnMnO_4$ (Ln = La, Nd, Sm, Gd), $BaLnMnO_4$ (Ln = La, Nd) et $M_{1+x}La_{1-x}MnO_4$ (M = Sr, Ba) [J]. *J. Solid State Chem.*, 1977, **22**: 121.

[2] Kamegashira N, Ueno S, Nakano H, Enami K. Physical properties and high resolution electron microscope study of barium neodymium manganeses tetra oxide [$BaNdMnO_4$] [J]. *Mater. Res. Bull.*, 1994, **29**(2): 185.

[3] Ueno S, Iwasaki K, Kamegashira N, Nakano H. Physical properties and electron microscopy study of $BaPrMnO_4$ [J]. *Mater. Chem. Lett.*, 1995, **42**: 201.

[4] Kamegashira N, et al. Synthesis of single crystal of $BaLnMnO_4$ (Ln = rare earth) in preparation.

[5] Nakano H, Ishizawa N, Kamegashira N, Zulhadjri, Shishido T. Electron microscopic study on $SrGdMnO_4$[J]. *J. Alloys and Compounds*, 2006, **408-412**: 593.

[6] Muradyan L A, Tamazyan R A, Kevorkov A M, Bagfasarov Kh S, Simonov V I. Atomic structure of $(La_{1-x}Sr_x)_2CuO_4$ with various strontium content [J]. *Kristallografiya*, 1990, **35**: 861.

[7] Rial C, Amador U, Moran E, Alario-Franco M A, Andersen N H. Evidence of interstitial oxygen in room temperature oxidized $La_{(2-x)}Sr_{(x)}CuO_{(4+y)}$ ($0 < x < 0.1$) [J]. *Physica C (Amsterdam)*, 1994, **234**: 237.

[8] Neaney P J, Mehta A, Sarosi G, Lamberti V E, Navrotsky A. Structural effects of Sr substitution in $La_{(2-x)}Sr_{(x)}NiO_{(4-delta)}$[J]. *Physical Review 3B-Condensed Matter*, 1998, **57**: 10370.

[9] Nakano H, Kawabata N, Kamegashira N. New phase of $BaLaMnO_{4-x}$ formed by annealing in a reducing atmosphere [J]. *J. Ceram. Soc. Jpn.*, 2008: in press.

ELSEVIER

Journal of Alloys and Compounds 408–412 (2006) 593–597

Journal of ALLOYS AND COMPOUNDS

www.elsevier.com/locate/jallcom

Electron microscopic study on $SrGdMnO_4$

Hiromi Nakano [a,*], Nobuo Ishizawa [b], Naoki Kamegashira [c], Zulhadjri [c], Toetsu Shishido [d]

[a] *Ryukoku University, Seta, Otsu 520-2194, Japan*
[b] *Nagoya Institute of Technology, 10-6-29 Asahigaoka, Tajimi 507-0071, Japan*
[c] *Toyohashi University of Technology, Tempaku-cho, Toyohashi 441-8580, Japan*
[d] *IMR in Tohoku University, Sendai 980-8577, Japan*

Received 30 July 2004; received in revised form 27 September 2004; accepted 15 December 2004
Available online 1 July 2005

Abstract

Single crystals of $SrGdMnO_4$ have been synthesized by the floating zone method. The structure was characterized as the K_2NiF_4-type, using X-ray diffraction (XRD) and a transmission electron microscope (TEM). Presence of weak reflections breaking the archetypal tetragonal symmetry was observed from the selected area diffraction (SAD). The compound was found to have an orthorhombic unit cell of $a \cong b = 0.532(4)$ nm, $c = 1.271(6)$ nm, by taking the a and b axes along the diagonal directions on the basal plane of the tetragonal archetype. Structural change occurred around 1018 K. The weak reflections disappeared in the SAD pattern, suggesting that crystal is of the archetype above 1018 K.

Keywords: Crystal growth; Transmission electron microscopy; X-ray diffraction; Crystal structure and symmetry

1. Introduction

Compounds of $(La, Sr)_2MO_4$ (M = Mn, Cu, Ni, Cr or Fe) with the K_2NiF_4-type structure have been the focus of research attention due to their electric and magnetic behaviours. Crystals of $La_{2-x}Sr_xMnO_4$ with $0.7 \leq x \leq 1.2$ were reported to take a tetragonal structure with the space group of *I4/mmm* [1]. Omata et al. prepared ceramics of $La_{2-x}Sr_xMnO_4$ with a wider range of $1.0 \leq x \leq 2.0$ and reported the lattice parameters and electrical conductivities [2]. Benabad et al. reported that the compounds of $SrLnMnO_4$ (Ln = La, Nd, Sm and Gd) take the K_2NiF_4-type structure with c/a ratios ranging from 3.445 to 3.428 [3].

In recent years, modifications having lower symmetries than that of the archetypal *I4/mmm* have been reported for the K_2NiF_4-type structure. For example, $La_{1.54}Sr_{0.46}NiO_4$ and $La_{1.91}Sr_{0.09}CuO_{4.12}$ take the monoclinic [4] and orthorhombic [5] structures, respectively. The structure relationship and phase transitions among these modifications and the archetype have been investigated and discussed in terms of the octahedral tilting system [6–9].

Recently, we succeeded in synthesizing a new compound $SrGdMnO_4$ by the floating zone method [10]. Structural characterization of the compound was thus performed using X-ray diffraction (XRD), and transmission electron microscope (TEM) with energy-dispersive spectroscopy (EDS).

2. Experimental procedure

Starting materials of high-purity (99.9%) $SrCO_3$, Gd_2O_3 and Mn_2O_3 went through the heat treatment for purification before weighing. These materials were mixed in an agate mortar in a stoichiometric composition of Sr:Gd:Mn being equal to 1:1:1. The mixture was compressed in a rubber tube into a rod shape under hydrostatic pressures. The rod was heated at 1273 K for 9 h in Ar gas atmosphere, and then at

* Corresponding author. Tel.: +81 77 543 7774.
E-mail address: hiromi@rin.ryukoku.ac.jp (H. Nakano).

0925-8388/$ – see front matter © 2005 Elsevier B.V. All rights reserved.
doi:10.1016/j.jallcom.2004.12.181

1673 K for 48 h. The obtained product was confirmed to be a single phase of polycrystalline $SrGdMnO_4$ by XRD. The rod was placed in a floating zone (FZ) furnace equipped with the bi-ellipsoidal halogen lamp. Crystals were grown from the melt at the growth rate of 20 mm/h. Details of the growth experiment will be published elsewhere [10]. Crystals used for the present study are as-grown crystals except for the quench experiment described in Section 3.2. The quenched sample used in 3.2 was annealed in a 1% H_2–Ar atmosphere at 1273 K for 5 days, followed by rapid quenching to room temperature.

The crystal was crushed into powder for powder XRD experiment. The crushed specimen was scooped with carbon-coated copper microgrids for the TEM observation. The TEM (JEOL-3000F) can provide electron probes with a full width at half maximum of around 0.5 nm as well as a sufficiently high current for the point- and mapping-analyses by EDS.

The in situ observation was performed using a thermal stage in TEM (JEM-2000EX, EM-SHTH specimen holder, Japan). The temperature of the stage was controlled manually from room temperature to 1018 K with a heating rate of approximately 973 K/h. The temperature was kept at 973 K for 30 min, and again increased to 1018 K. The observation was done at 673, 973 and 1018 K.

3. Results and discussion

3.1. Symmetry

The stability of the A_2BX_4-structure is often discussed in terms of the tolerance factor t [11]. The t-values of various K_2NiF_4-type compounds fall in the range of $0.8 < t < 1.0$ [9]. When t approaches the lower limit, the structure is subject to distortion and the symmetry changes from tetragonal to orthorhombic or monoclinic [9]. The t-value of 0.881 for $SrGdMnO_4$ is slightly smaller than 0.901 for $LaSrMnO_4$ with archetypal K_2NiF_4 structure [9].

Powder X-ray diffraction pattern of $SrGdMnO_4$ showed that the peaks could be indexed based on a tetragonal unit cell with lattice parameters $a = 0.532(4)$ nm and $c = 1.271(6)$ nm. Although the electron microscopy experiments revealed a faint but clear sign of symmetry changes from tetragonal to orthorhombic as described later, the difference between the a and b lengths was too small to be detected by the use of conventional powder XRD.

Geometrical relationship of the present crystal to the underlying archetypal structure with unit cell vectors $\boldsymbol{a}_t$, $\boldsymbol{b}_t$ and $\boldsymbol{c}_t$ can be given as $\boldsymbol{a}_t = (\boldsymbol{a} - \boldsymbol{b})/2$, $\boldsymbol{b}_t = (\boldsymbol{a} + \boldsymbol{b})/2$ and $\boldsymbol{c}_t = \boldsymbol{c}$. The space group of the archetype can be converted from *I*4/*mmm* to *F*4/*mmm* when the unit cell vectors are taken along the same directions as the present crystal.

Typical SAD patterns of the compound are shown in Fig. 1a–c, which were taken from [0 0 1], [$\bar{1}$ 1 0] and [2 1 $\bar{1}$] zone axes, respectively. The reflections with strong intensities satisfy a condition, $h\,k\,l$ all even or all odd, and are those allowed for the *F*4/*mmm* symmetry. On the other hand, the SAD patterns in Figs. 1a and 2c indicate a presence of extra reflections with weak intensities which do not conform to the archetypal symmetry. Presence of 1 2 0 and 2 1 0 reflections in Fig. 1a disagrees with the $P4_2/ncm$ symmetry reported for La_2CuO_4 [7], which excludes the $h\,k\,0$ reflections with $h + k$ odd. Possibility of the double diffraction effect was examined but ended with a conclusion that this was not the case for the 1 2 0 and 2 1 0 reflections. Detailed, though limited, search to find systematic extinction rules was performed from the SAD patterns. The 1 1 0, 1 0 1 and 0 1 1 reflections were not observed. The apparent presence of $0\,k\,0$ and $h\,0\,0$ reflections with h and k taking odd numbers in the [0 0 1] zone axis SAD pattern were explained by the double diffraction effect because no such reflections were observed in the [0 $\bar{1}$ 0] and [$\bar{2}$ 0 1] zone axis SAD patterns. The series of $0\,0\,l$ reflections with l odd were systematically absent as shown in Fig. 1b. The $h\,0\,l$, $0\,k\,l$ reflections with l odd were also systematically absent.

Orthorhombicity of the crystal was examined by measuring the distances of $(2\,0\,0)^*$ and $(0\,2\,0)^*$ in Fig. 1a using vernier calipers. The measurement was referenced to the polycrystalline rings of the Au film. The ratio of the $(0\,2\,0)^*/(2\,0\,0)^*$ spacing was thus determined to be

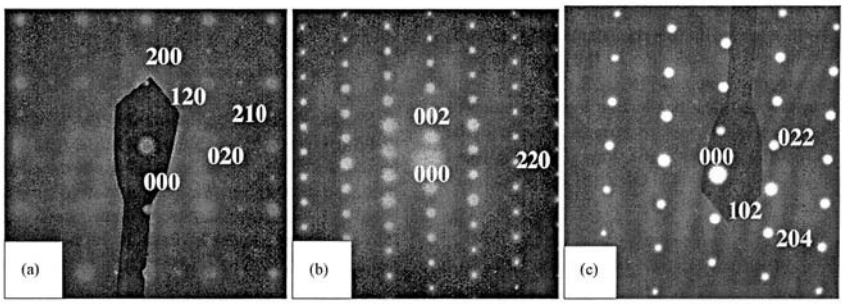

Fig. 1. Typical SAD patterns of $SrGdMnO_4$ taken from (a) the [0 0 1] zone axis, (b) [$\bar{1}$ 1 0] and (c) [2 1 $\bar{1}$].

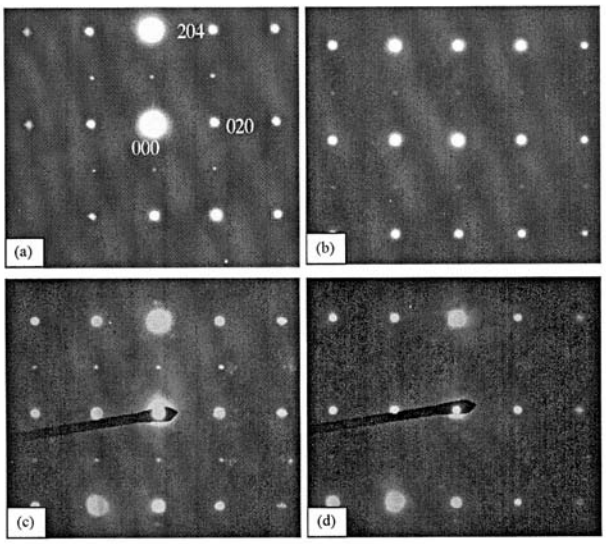

Fig. 2. Changes in SAD patterns of $SrGdMnO_4$ heated in TEM device at: (a) room temperature, (b) 673 K, (c) 973 K and (d) 1018 K.

0.994, suggesting a possible orthorhombic distortion for $SrGdMnO_4$. If the crystal is orthorhombic, these extinction rules uniquely lead to *Pccm* as a possible space group for $SrGdMnO_4$ at room temperature.

Aleksandrov [8] carried out a crystallographic analysis on the possible structural variants in the A_2BX_4 family arising from the tilting of BX_6 octahedra. In addition to the octahedral tilting, the Jahn–Teller (J–T) distortion accompanies in the case of $Mn^{3+}O_6$. This effect manifests itself in the changes of unit cell size and the *c*/*a* ratio in $Sr_{1+x}La_{1-x}MnO_4$ ($0<x<1$) [3]. In $SrGdMnO_4$, the cation valence can be assumed as Sr^{2+}, Gd^{3+} and Mn^{3+}. If a d^4 high spin state is assumed for the electron configuration of Mn^{3+}, the crystal field can be stabilized by the tetragonal elongation of the coordinating O_6 octahedron along the *c*-axis. This sort of J–T distortion, however, may contribute little to the symmetry changes from tetragonal to orthorhombic. Therefore, the appearance of weak reflections on the a^*–b^* plane should be related to the tilting of MnO_6 octahedra, and accordingly to the orthorhombic *Pccm* distortion.

In the case of $BaLnMnO_4$ (Ln = Pr or Nd), a similar unit cell of 0.5 nm × 0.5 nm × 1.2 nm to $SrGdMnO_4$ was reported [12,13]. However, the [0 0 1] zone axis SAD pattern of $BaPrMnO_4$ [13] is different from the present crystal in that the 1 1 0 reflection is absent in $SrGdMnO_4$.

In the copper-bearing K_2NiF_4-type structures, i.e., La_2MO_4 (M = Cu, Ni) [14–17] and $La_{2-x}Ba_xCuO_4$ [18,19], various space groups have been reported so far. We have noticed that our electron diffraction data are essentially the same as those of $La_{1.9}Ba_{0.1}CuO_4$ [19] with the orthorhombic *Pccm* structure. A detailed single crystal X-ray diffraction analysis is being undertaken.

3.2. Structural transition at high temperatures

The structural phase transition in $SrGdMnO_4$ was investigated with increasing temperature by TEM. Fig. 2 shows SAD patterns taken from $[\bar{2}\,0\,1]$ at room temperature in (a), 673 K in (b), 973 K in (c) and 1018 K in (d) using the as-grown crystal. The weak reflections disappeared at 1018 K. These findings show that a structural transition occurs from orthorhombic to tetragonal around 1018 K and the crystal takes the archetypal structure above that temperature.

Similar disappearance was confirmed in a quenched specimen at room temperature. Fig. 3 shows SAD patterns of the quenched specimen taken from the [0 0 1] zone axis in (a) and $[\bar{1}\,0\,0]$ in (b). No weak reflections forbidden for *F*4/*mmm* were observed between the parent reflections underlying the archetype structure.

3.3. Microstructure

The microstructure of $SrGdMnO_4$ as-grown crystals was analyzed by SEM–EDS and TEM–EDS. This was done because the Sr component is apt to vaporize in Sr-bearing compounds in the course of melt-growth owing to its high vapor pressure at elevated temperatures.

Fig. 4 is a TEM image of a crushed specimen of this compound. The two regions enclosed by circles in the figure were found to have different chemical compositions. As

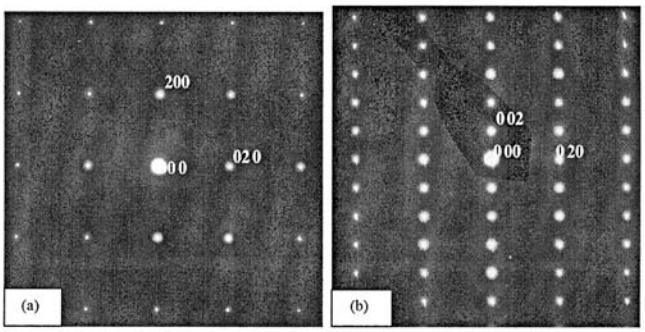

Fig. 3. SAD patterns of quenched $SrGdMnO_4$ taken from (a) the [1 0 0] zone axis and (b) [$\bar{1}$ 0 0].

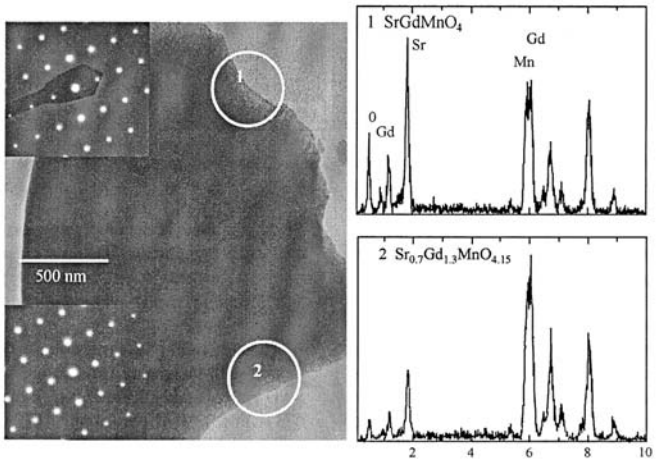

Fig. 4. TEM image of $SrGdMnO_4$ involving two regions with different chemical compositions enclosed by the circles. Insets are corresponding SAD patterns.

shown in the EDS spectra in Fig. 4, the region 1 was estimated to be a stoichiometric $SrGdMnO_4$ 1:1 composition while the region 2 is Sr-deficient with an estimated composition of $Sr_{0.7}Gd_{1.3}MnO_{4.15}$. In spite of difference in Sr content in these two regions, the SAD patterns are similar as shown in the insets of Fig. 4, suggesting an isomorphous structure for these regions. It is also notable that no clear boundary between them was detectable from this study.

4. Conclusions

Crystals of $SrGdMnO_4$ were prepared by the floating zone method. The structure was investigated by X-ray diffraction and transmission electron microscopy. Presence of extra reflections with weak intensities was detected between the present strong reflections underling the archetypal K_2NiF_4 structure with tetragonal *I4/mmm* symmetry. The extinction rules of $SrGdMnO_4$ at room temperature resemble those of $La_{1.9}Ba_{0.1}CuO_4$ with the orthorhombic *Pccm* structure.

A structural phase transition was observed around 1018 K for $SrGdMnO_4$ on the thermal stage in TEM device. The SAD pattern of the specimen above 1018 K showed the disappearance of the extra reflections with weak intensities, indicating that the high temperature phase is of *I4/mmm* archetype. A similar absence of the extra reflections with weak intensities was also confirmed in the quenched specimen at room temperature.

Most part of the crystal was identified to have a stoichiometric composition of $SrGdMnO_4$, nevertheless a Sr-deficient region was found occasionally. The chemical composition of the region was determined to be $Sr_{0.7}Gd_{1.3}MnO_{4.15}$ whose symmetry was supposed to be the same as that of $SrGdMnO_4$.

References

[1] I. Shimono, H. Konishi, J. Ceram. Soc. Jpn. 100 (1992) 1343 (in Japanese).
[2] T. Omata, S. Hoshino, H. Ikawa, T. Sasamoto, J. Ceram. Soc. Jpn. 103 (1995) 1297 (in Japanese).
[3] A. Benabad, A. Daoudi, R. Salmon, G. Leflen, J. Solid State Chem. 22 (1977) 121 (in French).
[4] P.J. Heaney, A. Mehta, G. Sarosi, V.E. Lamberti, A. Navrotsky, Phys. Rev. B 57 (17) (1998) 10370.
[5] C. Rial, E. Moran, M.A. Alario-Franco, U. Amador, N.H. Anderson, Physica C 254 (1995) 233.
[6] D.M. Hatch, H.T. Stokes, Phys. Rev. B 35 (16) (1987) 8509.
[7] K.S. Aleksandrov, I.N. Flerov, S.V. Melenikova, A.I. Kuglik, S.V. Misyul, O.A. Ageev, Ferroelectrics 104 (1990) 285.
[8] K.S. Aleksandrov, Sov. Phys. Crystallogr. 32 (4) (1987) 551.
[9] P. Ganguly, C.N.R. Rao, J. Solid State Chem. 53 (1984) 193.
[10] N. Kamegashira, in preparation.
[11] G.H. Jonker, J.H. van Santen, Physica 16 (1950) 337.
[12] N. Kamegashira, S. Ueno, H. Nakano, K. Enami, Mater. Res. Bull. 29 (2) (1994) 185.
[13] S. Ueno, K. Iwasaki, N. Kamegashira, H. Nakano, K. Enami, Mater. Chem. Phys. 42 (1995) 201.
[14] P. Odier, M. Le Blanc, J. Choisnet, Mater. Res. Bull. 21 (1986) 787.
[15] P. Zolliker, D.E. Cox, J.B. Parise, E.M. Mac Carron, Phys. Rev. B Condens. Matter 42 (10) (1990) 6332.
[16] T. Kajitani, T. Onozuka, Y. Yamaguchi, M. Hirabayashi, S. Yashuhiko, Jpn. J. Appl. Phys. Part 2 26 (1987) 1877.
[17] K. Yamada, E. Kudo, Y. Endoh, K. Tsuda, M. Tanaka, H. Asano, F. Izumi, M. Oda, Y. Hidaka, M. Suzuki, Jpn. J. Appl. Phys. Part 1 27 (1988) 1132.
[18] S. Katano, J.A. Ferrnandez-Baca, S. Funahashi, N. Mori, Y. Ueda, K. Koga, Physica C 214 (1993) 64.
[19] Y. Hirotsu, S. Nagakura, Y. Murata, T. Nishihara, M. Takata, T. Yamashita, Jpn. J. Appl. Phys. Part 2 26 (1987) 380.

journal

J. Am. Ceram. Soc., 90 [4] 1276–1279 (2007)
DOI: 10.1111/j.1551-2916.2007.01529.x

Nano-Domain Twin Structure Formed by Phase Transition in New Perovskite Oxide $(Sr_{0.67}Sm_{0.33})(Mn_{0.33}Ti_{0.67})O_3$

Hiromi Nakano†

Electron Microscope Laboratory, Ryukoku University, Otsu 520-2194, Japan

Migaku Kobayashi

Department of Chemistry and Biochemistry, Numazu College of Technology, Numazu 410-8501, Japan

Nakoi Kamegashira

Toyohashi Campus Innovation, Toyohashi University of Technology, Toyohashi 441-8580, Japan

A new perovskite oxide, $(Sr_{0.67}Sm_{0.33})(Mn_{0.33}Ti_{0.67})O_3$, was synthesized at 1573 K in an Ar flow. The structure of the oxide was determined to be orthorhombic with the space group of *Pnma* using X-ray diffraction and electron diffraction. High-resolution transmission electron microscope (HRTEM) images of the oxide revealed that nano-domain structures were formed by twinning due to a phase transition. This is the first time that phase transition of the oxide has been observed *in situ* using a heating stage in a TEM. The high-temperature phase possessed an orthorhombic structure with the space group of *Imma*, which appeared above 723 K.

I. Introduction

Rare earth manganese perovskites ($LnMnO_3$, Ln = rare earth) and their related compounds exhibit interesting electrical, magnetic, and optical properties.[1,2] They are best known for their excellent colossal magnetoresistance characteristics.[3–5] For the appearance of useful properties in perovskite systems, various oxides are formed by the combination of the A-site ion or the B-site ion with different valences and ionic sizes. In such a partial-substitution oxide, the shape and tilt of the MnO_6 octahedron depend on the rare-earth species at the A-site.[6,7] Oxides with a combination of Mn and Ti ions at the B sites were synthesized under various atmospheres by varying the oxidation states of these ions. The Ln_2MnTiO_6 (Ln = rare earth) phase was synthesized in a reducing atmosphere, and it has an orthorhombic structure (*Pnma*) for Ln = La–Nd, a monoclinic structure for Ln = Sm–Gd, and a hexagonal structure ($P6_3cm$) for Yb.[8–12] Some of these oxides exhibit antiferromagnetic properties.[9–11] The oxide $(Ca_{0.9}La_{0.1})(Mn_{1-x}Ti_x)O_3$ was synthesized in a previous study with an orthorhombic structure (*Pnma*) in an oxygen gas flow.[13] The role of the tetravalent ion was clarified from the relationship between the average (Mn,Ti)–O distance and the electrical properties.[13] Recently, the present authors synthesized oxides with various structures in an Ar flow including $(Ca_{0.5}La_{0.5})(Mn_{0.5}Ti_{0.5})O_3$ possessing a cubic structure ($Pm\bar{3}m$), $(Sr_{0.5}La_{0.5})(Mn_{0.5}Ti_{0.5})O_3$ with a rhombohedral structure ($R\bar{3}c$), and $(Ca_{0.5}Ln_{0.5})(Mn_{0.5}Ti_{0.5})O_3$ (Ln = La, Nd, Eu) and $(Ca_{0.5}Ln_{0.5})(Mn_{0.33}Ti_{0.67})$ (Ln = Y, Gd, Dy, Ho, Yb) with orthorhombic structures (*Pnma*).[14,15]

In the present study, a new oxide, $(Sr_{0.67}Sm_{0.33})(Mn_{0.33}Ti_{0.67})O_3$, was synthesized in an Ar flow. The structure and microstructure were examined using X-ray diffraction (XRD) and a transmission electron microscope (TEM). High-resolution transmission electron microscope (HRTEM) images showed nano-domain structures formed by twinning in the grains of the oxide. It is known that phase transitions in perovskites are inevitably accompanied by twinning.[16,17] We attempted to observe the phase transition *in situ* by using a heating stage in the TEM. The phase transition of the new oxide was successfully observed, for the first time.

II. Experimental Procedure

A polycrystalline oxide of $(Sr_{0.67}Sm_{0.33})(Mn_{0.33}Ti_{0.67})O_3$ was synthesized by a solid-state reaction method. Starting materials (Ln_2O_3, $SrCO_3$, Mn_2O_3, and TiO_2) with 99.9% or better purity were used, and were pre-treated by heating to adjust the oxidation state of these ions.[15] Each of the pretreated reagents was weighed and then mixed together, and the mixture was pressed into pellets. The pellets were heated at 1573 K for 3 days in a purified Ar flow. The specimens were characterized using XRD (Cu$K\alpha$), and the XRD data were refined by the Rietveld method using the RIETAN program.[18]

The specimens were crushed and placed on a copper mesh with carbon-coated microgrids, and subjected to HRTEM observations. The TEM (JEM-3000F, JEOL, Tokyo, Japan) was operated at 300 kV with spherical aberration $C_s = 1.0$ nm.

In situ observations were performed using a heating stage in a temperature range from room temperature to 1073 K in the TEM (JEM-2000EX, EM-SHU2 specimen holder, JEOL). The temperature was controlled manually, and the heating rate and cooling rate were about 600 and 300 K/h, respectively.

III. Results and Discussion

The structure of the new oxide, $(Sr_{0.67}Sm_{0.33})(Mn_{0.33}Ti_{0.67})O_3$, was refined by Rietveld analysis of the XRD data. It possesses an orthorhombic structure with the space group *Pnma*. Table I shows the atomic parameters of the room-temperature phase of the oxide. The crystal symmetry of the oxide was also determined by an electron diffraction method and was in good

T. Yano—contributing editor

Manuscript No. 22221. Received September 7, 2006; approved November 21, 2006.
This work was partially supported by a Grant-in-Aid for Scientific Research (c) No. 18560662 by the Japan Society for the Promotion of Science. We would like to thank Ms. R. Katsuraya for help with the synthesis of the oxide.
†Author to whom correspondence should be addressed. e-mail: hiromi@rins.ryukoku.ac.jp

Table I. Atomic Parameters of the Room-Temperature Phase Refined by Rietveld Analysis

Atom	Site	*x*	*y*	*z*	B (nm^2)
Sr, Sm	4*c*	0.0150(3)	1/4	−0.001(1)	0.0078(3)
Ti, Mn	4*b*	0	0	1/2	0.0035(4)
O1	4*c*	0.496(2)	1/4	0.051(6)	0.007(1)
O2	8*d*	0.226(3)	0.532(2)	0.238(4)	0.007(1)

Pnma (No. 62) $a = 0.55126(8)$ nm, $b = 0.77810(5)$ nm, $c = 0.55137(9)$ nm, $R_{wp} = 12.2\%$, S = 1.25.

agreement with the results shown in Table I. Some perovskites with an orthorhombic structure (*Pnma*) have been reported with various oxidation states of the Mn ions, including $(Ca_{0.5}Sm_{0.5})MnO_3$ (Mn:3.5+),[19] $(La_{0.1}Ca_{0.9})(Mn_{1-x}Ti_x)O_3$ $(0<x<0.9)$ (Mn:3.9+ ~3+), and $(Ca_{0.5}Sm_{0.5})(Mn_{0.5}Ti_{0.5})O_3$ (Mn: 3+).[15] In the present case, the Mn oxidation state of $(Sr_{0.67}Sm_{0.33})(Mn_{0.33}Ti_{0.67})O_3$ was estimated to be tri-valent because the oxide was synthesized under an Ar atmosphere.

The microstructure of the material was observed using the HRTEM. Figure 1 shows a nano-domain structure composed of three types of orientations. A selected area diffraction (SAD) pattern was obtained using an aperture of 200 nm diameters. The complex SAD pattern (d) was composed of three patterns (a–c), and these patterns were clarified by simulations using the atomic parameters in Table I. Along the [101]/[10$\bar{1}$] zone axis, a twin structure was formed by 90° rotation as shown in Figs. 1(a) and (b). In addition, the pattern from the [010] zone axis (in Fig. 1(c)) was also superposed by a 90° rotation. The domain boundaries of [101]/[10$\bar{1}$] or [101]/[010] were clearly observed in the enlarged images in Fig. 1. The complex pattern was easily formed by twinning, as the (020) spacing is close to the (101) spacing, with a difference of 0.2%. A periodic distance of 0.78 nm was observed in the HRTEM image, and small domains were formed by the same orientations of the periodic lattice image. HRTEM images of each domain corresponded to those of the diffraction patterns (a–c). The domain boundaries were not straight but were coherent with no mismatch. The domain size may be related to the degree of the lattice mismatch. The domains had a width of about 30 nm, and they were much smaller than those in some perovskites reported previously.[16,17]

Figure 2 also shows a twin structure along the [2$\bar{1}$0] zone axis in the HRTEM image. The insets show simulated diffraction patterns (a–c) and the superposed diffraction pattern (d), which was composed of the three patterns rotated by 60°. The lattice image with a repeat distance of 0.55 nm was observed along the three orientations, rotated by 60°. Other types of twin structures were also observed in the specimen. The (100) reciprocal plane was superposed on the (001) reciprocal plane, whose relationship was 90° rotated around the b^* axis. The (002) spacing was nearly equal to the (200) spacing, and the difference was only 0.02%.

In general, a twin structure is formed during phase transitions in perovskites.[16] It was therefore expected that a phase transition would occur in the present perovskite, $(Sr_{0.67}Sm_{0.33})(Mn_{0.33}Ti_{0.67})O_3$. We tried to observe the phase transition *in situ* in the TEM using a heating holder under vacuum. It is to be noted that the thermal behavior should not be measured in air, as the oxidation state of Mn^{3+} ion would be easily changed in air. The phase transition of the oxide was successfully observed in the high-temperature TEM.

Figure 3 shows changes in SAD patterns due to phase transition by heating (a)–(c) and by cooling (d)–(e). The SAD pattern of the room-temperature phase was taken from the [101]/[10$\bar{1}$] zone axis by twining in Fig. 3(a). The intensity of the reflections started to decrease around 593 K, and then transformed into a higher symmetrical structure at approximately 723 K by heating. The specimen temperature was maintained at 823 K for 20 min, and after that the holder temperature was decreased. The twinning pattern reappeared around 653 K, as shown in Fig. 3(d). Figure 4 shows the typical SAD patterns of the high-temperature phase above 723 K. The structure of the high-

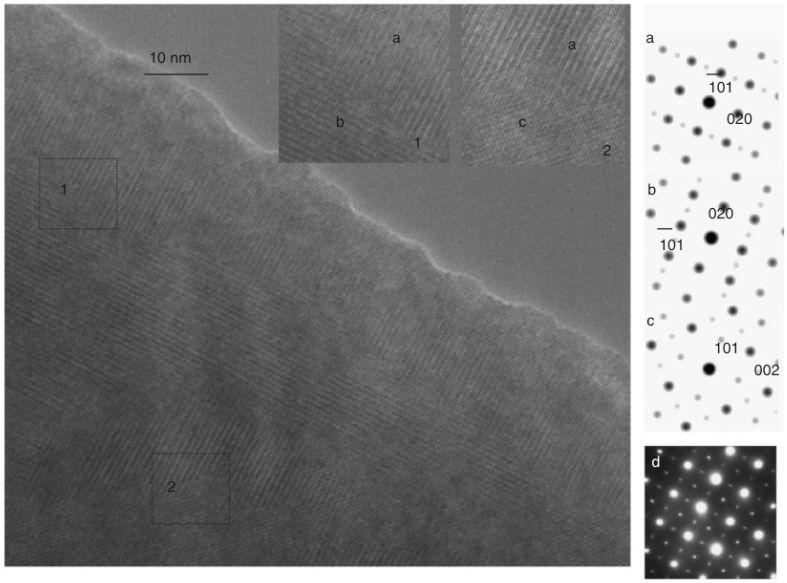

Fig. 1. High-resolution transmission electron microscope image taken from the [101]/[010] zone axes. The insets show enlarged images in the encircled region of 1 and 2, respectively. The simulated diffraction patterns projected along (a) [101], (b) [101], and (c) [010]. (d) Observed electron diffraction pattern.

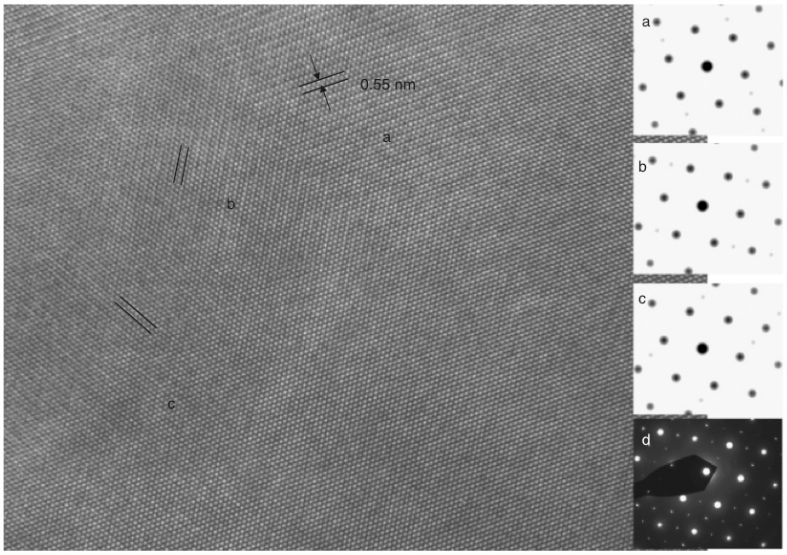

Fig. 2. High-resolution transmission electron microscope image taken from the [2$\bar{1}$0] zone axis. The insets show simulated diffraction patterns (a–c), and (d) observed electron diffraction pattern.

temperature phase seems to have a close relation with the orthorhombic *Imma* structure, which was derived from the extinction rule of the reflections in Fig. 4. The relationship between *Pnma* and *Imma* was described by the distortion of $(Mn,Ti)O_6$ octahedra as $\phi^-\phi^+\phi^-$ and $\phi^-o\phi^-$, respectively.[17] The distortion of octahedra is related to the crystal symmetry of perovskites, by Aleksandrov.[20] Therefore, the phase transition (*Pnma*—*Imma*) could be explained by the control of the distortion of the $(Mn, Ti)O_6$ octahedra.

It is expected that a similar phase transition would occur in another rare-earth perovskite, $(Sr_{0.67}Ln_{0.33})(Mn_{0.33}Ti_{0.67})O_3$, because the structural symmetry is the same, and the difference

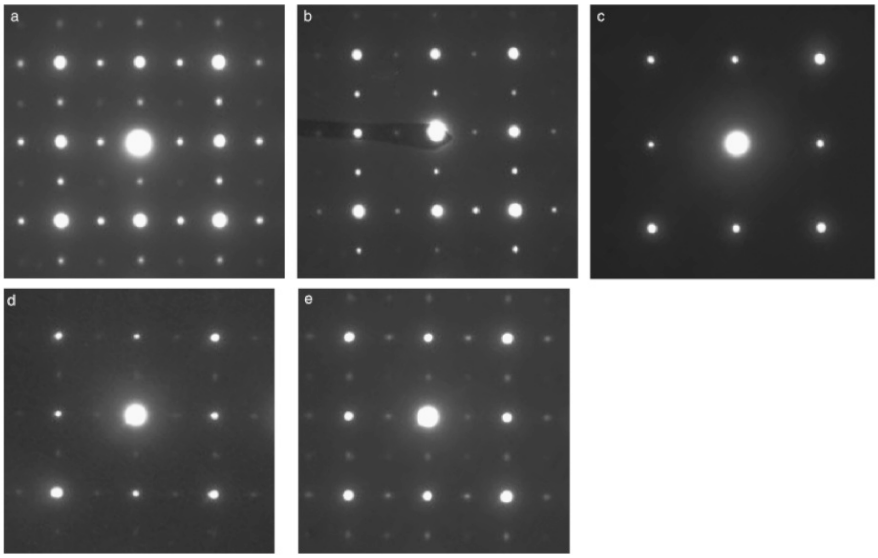

Fig. 3. Changes in the selected area diffraction pattern due to phase transition by heating (a)–(c) and by cooling (d)–(e). (a) At room temperature, (b) at 593 K, and (c) above 723 K. The specimen temperature was maintained at 823 K for 20 min and after that, (d) at 653 K, and (e) at room temperature.

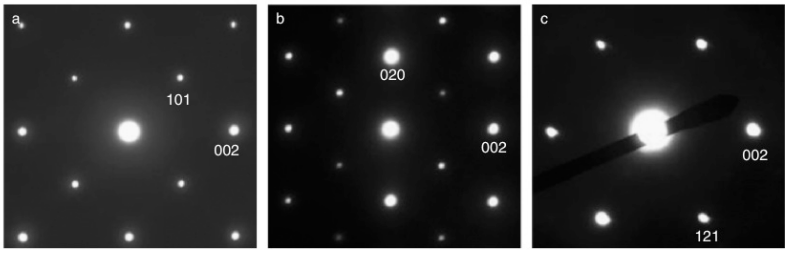

Fig. 4. Selected area diffraction patterns of the high-temperature phase taken from the (a) [010] zone axis (b) [100] and (c) [2$\bar{1}$0].

in other rare-earth oxides might be the degree of distortion of the MnO_6 octahedra.

IV. Conclusions

A new perovskite oxide, $(Sr_{0.67}Sm_{0.33})(Mn_{0.33}Ti_{0.67})O_3$, was synthesized at 1573 K. The oxide possessed a single phase with an orthorhombic structure, with lattice parameters of $a = 0.55126(8)$ nm, $b = 0.77810(5)$ nm, and $c = 0.55137(9)$ nm. The crystal symmetry was determined to be *Pnma* (No. 62) by XRD and electron diffraction methods. HRTEM observations of the oxide revealed that nano-domain structures were formed by twinning in the grains. The twinning was formed easily during the phase transition as the lattice spacing is similar to each other; e.g., (020) is nearly equal to (101), and (002) is very close to (200). The phase transition of the oxide was observed *in situ* by TEM for the first time using a thermal stage. The phase transition could be observed *in situ*, as indicated by the disappearance of weak reflections in the SAD pattern along the [001] and [101] above 723 K. The high-temperature phase was determined to be an orthorhombic structure with the space group of *Imma*.

References

[1]R. Shiina, T. Nishitani, and H. Shiba, "Magnetic Ordering, Orbital, and Lattice Distortion in Perovskite Manganites," *J. Phys. Soc. Jpn.*, **66** [10] 3159–70 (1997).
[2]J. Q. Li, "Structural Properties of the Perovskite Manganites," *J. Apply. Phys.*, **90** [2] 637–43 (2001).
[3]S. Jin, M. Mavvormack, T. H. Tiefel, and R. Ramesh, "Colossal Magnetoresistance in La–Ca–Mn–O Ferromagnetic Thin-Films," *J. Appl. Phys.*, **76** [10] 6929–33 (1994).
[4]Y. Tokura, A. Urushibara, Y. Moritomo, T. Arima, A. Asamitsu, G. Kido, and N. Furukawa, "Giant Magnetotransport Phenomena in Filling-Controlled KONDO Lattice System: $La_{1-x}Sr_xMnO_3$," *J. Phys. Soc. Jpn.*, **63**, 3931–5 (1994).
[5]A. Urushibara, Y. Moritomo, T. Arima, A. Asamitsu, G. Kido, and Y. Tokura, "Insulator-Metal Transition and Giant Magnetoresistance in $La_{1-x}Sr_xMnO_3$," *Phys. Rev. B*, **51**, 14103–9 (1995).
[6]F. G. Galasso, *Structure, Properties and Preparation of Perovskites-Type Compound*. Pergamon, Oxford, 1969.
[7]A. M. Clazer, "The Classification of Tilted Octahedral in Perovskites," *Acta Cryst.*, **B28**, 3384–92 (1972).
[8]H. Nakano, N. Kamegashira, and K. Urabe, "In-situ Observation of the Change in Domain Structure Due to Phase Transition in a Perovskite La_2MnGaO_6," *Mater. Res. Bull.*, **37**, 2107–15 (2002).
[9]N. Kamegashira, N. Nakajima, K. Watanabe, and M. Kobayashi, "Synthesis and Crystal Structure of Sm_2MnTiO_6," *J. Alloys Comp.*, **311**, 74–8 (2000).
[10]N. Kamegashira, N. Nakajima, K. Watanabe, and M. Kobayashi, "Synthesis, Crystal Structure and Magnetic Properties of a New Compound Eu_2MnTiO_6," *Int. J. Mater. Prod. Tech.*, Special Issue, SPM1, **1**, 139–46 (2001).
[11]N. Kamegashira, M. Kobayashi, and J. Saito, "Synthesis, Crystal Structure and Some Properties of Ln_2MnTiO_6 Phases (Ln = Rare Earth)"; pp. 47–52 in *Frontiers of Solid State Chemistry*, Edited by S. H. Feng, and J. S. Chen. Words Scientific, River Edge, Singapore, 2002.
[12]H. Nakano, N. Kamegashira, and K. Urabe, "Structure Analysis of a New Oxide Yb_2TiMnO_6," *Mater. Res. Bull.*, **36**, 57–68 (2001).
[13]H. Taguchi, M. Sonoda, M. Nagao, and H. Kido, "Role of Tetravalent Ion in Metal-Insulato Transition in $(La_{0.1}Ca_{0.9})(Mn_{1-x}Ti_x)O_3$," *J. Solid State Chem.*, **126**, 235–41 (1996).
[14]M. Kobayashi, M. Yamaguchi, and N. Kamegashira, "Refinement of Crystal Structure of $MLaMnTiO_6$ (M = Ba, Sr) and $CaSmMnTiO_6$"; pp. 505–10 in *International Symposium on Designing Processing and Properties of Advanced Engineering Materials*, Edited by T. Kobayashi, M. Umemoto, and M. Morinaga. Japan, Toyohashi. 1997.
[15]M. Kobayashi, R. Katsuraya, S. Kurita, M. Yamaguchi, H. Satoh, and N. Kamegashira, "Synthesis and Crystal Structure of (Ca, R)(Mn, Ti)O_3 (R, Rare Earth)," *J. Alloys Comp.*, **408–412**, 1173–6 (2006).
[16]Y. Wang and R. C. Liebermann, "Electron Microscopy Study of Domain Structure Due O Phase Transitions in Natural Perovskite," *Phys. Chem. Minerals*, **20**, 147–58 (1993).
[17]Y. Wang, F. Guyot, and C. R. C. Liebermann, "Electron Microscopy of $(Mg,Fe)SiO_3$ Perovskite: Evidence for Structural Phase Transition and Implications for Lower Mantle," *J. Geo. Res.*, **97** [B9] 12327–347 (1992).
[18]F. Izumi, "A Software Package Fir the Rietveld Analysis of X-ray and Neutron Diffraction Patterns," *J. Crystallogr. Jpn.*, **27**, 23–31 (1985) [in Japanese].
[19]P. M. Woodward, T. Vogt, D. E. Cox, A. Aulraj, C. N. R. Rao, P. Karen, and A. K. Cheetham, "Influence of Cation Size on the Structural Features $Ln_{1/2}A_{1/2}MnO_3$ Perovskites at Room Temperature," *Chemistry Mater.*, **10**, 3652–65 (1998).
[20]K. S. Aleksandorv, "The Sequences of Structural Phase Transition in Perovskites," *Ferroelectrics*, **14**, 801–5 (1976). □

Available online at www.sciencedirect.com
SCIENCE DIRECT®
JOURNAL OF RARE EARTHS 24 (2006) 668 - 672
JOURNAL OF RARE EARTHS
www.elsevier.com/locate/jre

Phase Behavior and Crystal Structure of Perovskite-Type Rare Earth Complex Oxides

Migaku Kobayashi[1*], Ryoko Katsuraya[1], Tsubasa Nara[1], Yusuke Tomita[1], Hiromi Nakano[2], Naoki Kamegashira[3]
(*1. Department of Chemistry and Biochemistry, Numazu College of Technology, 3600 Ooka, Numazu 410-8501, Japan; 2. Ryukoku University, Seta, Otsu 520-2194, Japan; 3. Department of Materials Science, Toyohashi University of Technology, Tempaku-cho, Toyohashi 441-8580, Japan*)

Received 20 June 2006; revised 19 September 2006

Abstract: Several compounds of rare earth complex oxides containing manganese and titanium were synthesized in Ar, and their crystal structures were analyzed by powder X-ray diffraction data and Rietveld method. Structures of $A_{0.67}Ln_{0.33}Mn_{0.33}Ti_{0.67}O_3$ (A = Ca or Sr and Ln = rare earth) were found to have orthorhombic symmetry with the space group *Pnma*, and their interatomic distances and bond angles were obtained. This space group was also derived from electron microscopic study. Electrical conductivity of $Ca_{0.67}Ln_{0.33}Mn_{0.33}Ti_{0.67}O_3$ for several rare earth elements showed a semiconducting property with the activation energy of 0.4 eV. Some of these compounds of the strontium system show the antiferromagnetic properties below 10 K.

Key words: perovskite; crystal structure; X-ray diffraction; alkaline earth rare earth manganese titanium oxide
CLC number: O741 **Document code**: A **Article ID**: 1002 - 0721(2006)06 - 0668 - 05

Rare earth manganese oxides with a substitution of alkaline earth elements have been noted for colossal magnetoresistivity effect (CMR)[1~5]. Among rare earth complex oxides, including manganese and titanium on B-site inside the perovskite structure, Ln_2MnTiO_6 phase is synthesized under reducing atmosphere for Ln = La[6] and other rare earths[7~12], where the orthorhombic phase for Ln = La - Nd, monoclinic phase for Ln = Sm - Gd, and hexagonal phase for Ln = Yb. Some of these oxides have antiferromagnetic properties[7~11]. In addition to these phases, other compounds (A, Ln)(Mn, Ti)O_3 were reported by several authors[13~18]: Various compounds were prepared for various combinations of La and alkaline earth, or Y on A-site, by Havinga[13], to study a dilution of magnetic interaction between Mn ions via oxygen ion, by substitution of the Ti ion. Existence of several phases in this system, such as cubic ($BaLaTiMnO_6$), orthorhombic ($CaYTiMnO_6$), and rhombohedral phases ($CaLaTiMnO_6$), were found, and some compounds of the rhombohedral phase were found to have a transition to cubic phase at high temperature[13]. $La_{1-x}Ba_xMn_{1-x}Ti_xO_3$ ($0 \leqslant x \leqslant 0.25$) with cubic phase was prepared by Lotgering[14]. Orthorhombic $La_{1-x}Ba_xMn_{1-x}Ti_xO_3$ ($x < 0.125$) and $La_{1-x}Ca_xMn_{1-x}Ti_xO_3$ ($x \leqslant 0.05$) with *Pnma* space group were synthesized, and their crystal structures were analyzed by neutron diffraction method by Elemans et al.[15]. It was considered that the tetravalent titanium ion made the cation-anion-cation overlap integrals weaken in $La_{0.1}Ca_{0.9}Mn_{1-x}Ti_xO_3$[16]. Furthermore, some compounds were synthesized and refined by the present authors[17, 18] and these compounds had various crystal structures for

* **Corresponding author** (E-mail: m.kobayashi@numazu-ct.ac.jp)
Foundation items: Project supported by the Grant-in-Aid for Scientific Research (C) (18560662) by the Japan Society for the Promotion of Science
Biography: Migaku Kobayashi (1965 -), Male, Master, Associate professor; Research field: inorganic materials

rare earth in the A-site of the perovskite structure. For example, the crystal structure of $Ba_{0.5}La_{0.5}Mn_{0.5}Ti_{0.5}O_3$, $Sr_{0.5}La_{0.5}Mn_{0.5}Ti_{0.5}O_3$, and $Ca_{0.5}Sm_{0.5}Mn_{0.5}Ti_{0.5}O_3$ were cubic ($Pm\bar{3}m$), rhombohedral ($R\bar{3}c$), and orthorhombic system (*Pnma*), respectively[17]. Some phases of (Ca, Ln)(Mn,Ti)O_3 were isolated and their crystal structures were studied[18]. Thus the compounds in the alkaline earth-rare earth-manganese-titanium-oxygen systems had variations of crystal distortions. In this article, a further synthesis of several kinds of $Ca_{0.67}Ln_{0.33}Mn_{0.33}Ti_{0.67}O_3$ phases and corresponding Sr, containing compounds for various rare earths, was tried, to obtain single phases to identify the phase behavior, and some properties were also measured. The crystal structures of these compounds are determined by Rietveld analysis of X-ray powder diffraction data, and formation of the phase is discussed.

1 Experimental

A polycrystalline sample of $Ca_{0.67}Ln_{0.33}Mn_{0.33}Ti_{0.67}O_3$(Ln = La, Nd, Sm, Eu) and $Sr_{0.67}Ln_{0.33}Mn_{0.33}Ti_{0.67}O_3$(Ln = La, Nd, Sm, Gd) was prepared by the solid-state reaction method. All the starting materials had 99.9% or greater purity, and were pre-treated to adjust the oxygen stoichiometry[18]. Mixtures of Ln_2O_3, $CaCO_3$, Mn_2O_3, and TiO_2 in appropriate molar ration were pressed into pellets, and heated at 1573 K for 3 d in a purified Ar flow.

X-ray powder diffraction data of the sample were collected using Cu Kα radiation equipped with a single crystal graphite monochromator. The 2θ range was $20° < 2\theta < 120°$ with increments of 0.04°. The resulting data were analyzed by the Rietveld method using the RIETAN program[19,20]. The initial setting values of the lattice parameters for the Rietveld analysis were used for the values determined from a least square method. The electrical conductivity was measured by dc four-probe method. Electron microscopic study of some specimen was carried out by TEM (JEM-3000F, JEOL, Tokyo, Japan) operated at 300 kV. The magnetic susceptibility was measured by the SQUID method.

2 Results and Discussion

The powder X-ray diffraction patterns of single phases of $Ca_{0.67}Ln_{0.33}Mn_{0.33}Ti_{0.67}O_3$ (LnE = La, Sm, Nd, Eu) are shown in Fig. 1. For the specimen obtained in this study all the peaks on X-ray diffraction patterns can be indexed as an orthorhombic phase corresponding to $GdFeO_3$ type perovskite structure. The degree of split in some peaks characteristic of orthorhombic symmetry decreases with increase in ionic radius of rare earth ions.

Rietveld refinement of X-ray diffraction data was carried out based on the orthorhombic cell of dimensions $\sqrt{2}a_c \times 2a_c \times \sqrt{2}a_c$ with the space group *Pnma* (No.62), where a_c is the ideal cubic perovskite cell parameter. These crystallographic data from the results of the Rietveld analysis are listed in Table 1, and the observed and calculated profiles of $Ca_{0.67}La_{0.33}Mn_{0.33}Ti_{0.67}O_3$ are shown in Fig. 2. From this figure, these profiles are in good agreement each other, with an appropriate fitness factor of R_{wp}(weighted pattern R-factor), and a coefficient S (goodness of fits). The cell parameters b and c increase with increasing ionic radius of rare earth element, whereas, the cell parameter a slightly changes as shown in Fig. 3, which includes the previous results[18].

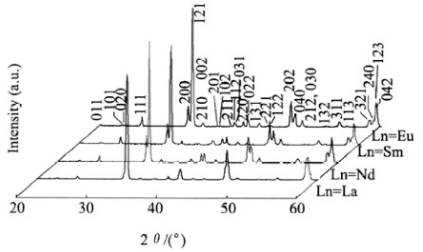

Fig. 1 Powder X-ray diffraction patterns of $Ca_{0.67}Ln_{0.33}Mn_{0.33}Ti_{0.67}O_3$ for Ln = La, Nd, Sm, and Eu (Observable peaks are indicated by Mirror index as the orthorhombic system)

Table 1 Crystallographic data and fractional atomic coordinates of $Ca_{0.67}Ln_{0.33}Mn_{0.33}Ti_{0.67}O_3$ (Ln = La, Nd, Sm, Eu)

Parameters	Ln = La	Ln = Nd	Ln = Sm	Ln = Eu
a/nm	0.54959(3)	0.5503(2)	0.55127(2)	0.55172(2)
b/nm	0.77175(7)	0.76639(2)	0.76377(3)	0.76245(3)
c/nm	0.54589(4)	0.54233(1)	0.54038(2)	0.53939(2)
R_{wp}/%	9.56	9.61	10.95	11.78
S	1.16	1.18	1.29	1.48
$x_{(Ca,R)}$	0.0268(3)	0.0383(2)	0.0444(2)	0.0477(2)
$z_{(Ca,R)}$	−0.0073(6)	−0.0075(4)	−0.0086(4)	−0.0092(5)
x_{O1}	0.487(1)	0.482(1)	0.480(1)	0.477(1)
z_{O1}	0.066(2)	0.080(1)	0.083(1)	0.085(2)
x_{O2}	0.214(1)	0.207(1)	0.205(1)	0.205(1)
y_{O2}	0.536(1)	0.5388(8)	0.5393(9)	0.5419(9)
z_{O2}	0.207(1)	0.206(1)	0.205(1)	0.206(1)
$B_{(Ca,R)}$/nm^2	0.0049(3)	0.0045(3)	0.0044(4)	0.0036(4)
$B_{(Mn,Ti)}$/nm^2	0.0038(4)	0.0034(4)	0.0029(5)	0.0038(5)
B_{O1}/nm^2	0.009(1)	0.002(2)	0.004(1)	0.007(2)
B_{O2}/nm^2	0.009(1)*	0.007(1)	0.004(1)*	0.006(1)

Space group *Pnma*; (Ca,R) and O1 in 4c (x,1/4,z), (Mn, Ti) in 4b (0, 0, 1/2), and O2 in 8d (x, y, z);

* It was calculated having assumed that the value of B_{O2} was equal to the value of B_{O1}

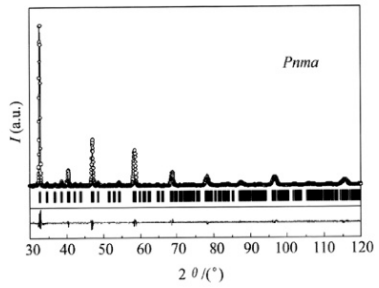

Fig. 2 Observed and calculated profiles of $Ca_{0.67}La_{0.33}Mn_{0.33}Ti_{0.67}O_3$ (Experimental points are shown by dots and calculated profile by a solid line. The small bars indicate the angular positions of the allowed Bragg reflections)

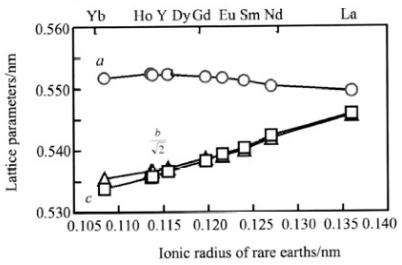

Fig. 3 Variation of lattice parameters of $Ca_{0.67}Ln_{0.33}Mn_{0.33}Ti_{0.67}O_3$ with ionic radius of rare earth element

Inside the crystal structure, a mean bond length between (Ca, Ln) in the A-site and oxygen ion increases with ionic radius of rare earth ions, as is shown in Fig. 4. An oxygen octahedron around the B-site (manganese and titanium ions) of these compounds is distorted, and a mean bond angle between (Mn, Ti)-O-(Mn, Ti) atoms decreases with rare earths, as shown in Fig. 5. Then, the oxygen octahedra around manganese and titanium ions in B-site of these compounds form zigzag arrays in a crystal.

The electrical conductivity of $Ca_{0.67}Ln_{0.33}Mn_{0.33}Ti_{0.67}O_3$ for various rare earths is shown in Fig. 6, and it is concluded from this figure that these compounds have semiconducting properties above room temperature with the activation energy near 0.45 eV.

For $Sr_{0.67}Ln_{0.33}Mn_{0.33}Ti_{0.67}O_3$ (Ln = La, Nd, Sm, Gd), similar results were obtained, and the crystallographic data of these orthorhombic compounds are shown in Table 2 with the space group *Pnma*. These structural results were supported by electron diffraction study, and SAD pattern of $Sr_{0.67}Gd_{0.33}Mn_{0.33}Ti_{0.67}O_3$ are shown in Fig. 7, taken from [001] and [1 ~ 20] zone axis. In this figure, all the diffraction spots could be assigned on the basis of orthorhombic symmetry with the space group *Pnma*.

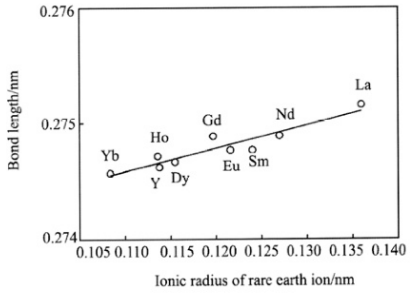

Fig. 4 Variation of a mean bond length between (Ca, Ln) in A-site and O of $Ca_{0.67}Ln_{0.33}Mn_{0.33}Ti_{0.67}O_3$ with ionic radius of rare earth ions

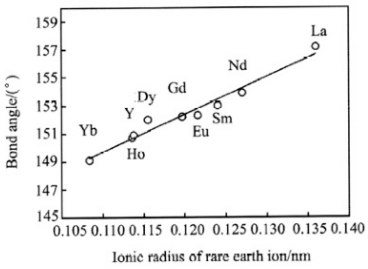

Fig. 5 Variation of a mean bond angle between (Mn, Ti)-O-(Mn, Ti) of $Ca_{0.67}Ln_{0.33}Mn_{0.33}Ti_{0.67}O_3$ with ionic radius of rare earth ions

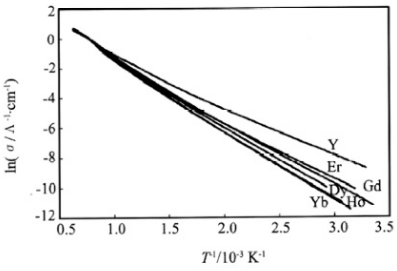

Fig. 6 Electrical conductivity of $Ca_{0.67}Ln_{0.33}Mn_{0.33}Ti_{0.67}O_3$ as a function of reciprocal temperature

Magnetic susceptibilities of some of these compounds are shown in Fig. 8 and it is derived that each compound has an antiferromagnetic behavior below 6.5, 8.0, and 2.6 K for Ln = Nd, Sm and Gd, respectively. Magnetization curve of $Sr_{0.67}Nd_{0.33}Mn_{0.33}Ti_{0.67}O_3$ against the applied magnetic field is shown in Fig. 9,

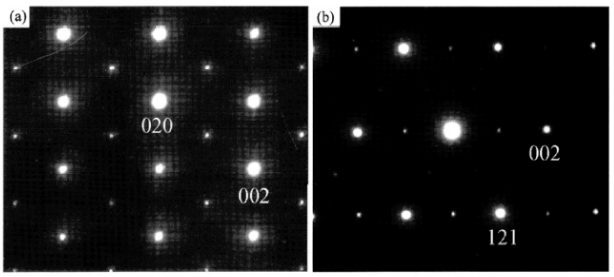

Fig.7 SAD patterns of $Sr_{0.67}Gd_{0.33}Mn_{0.33}Ti_{0.67}O_3$ taken from [001](a) and [2 - 10] (b)

and this compound includes a small portion of ferromagnetic component.

Table 2 Crystallographic data and fractional atomic coordinates of $Sr_{0.67}Ln_{0.33}Mn_{0.33}Ti_{0.67}O_3$ (Ln = La, Nd, Sm, Gd)

Parameters	Ln = La	Ln = Nd	Ln = Sm	Ln = Gd
a/nm	0.55132(4)	0.5514(1)	0.55126(8)	0.55008(8)
b/nm	0.78396(5)	0.78103(9)	0.77810(5)	0.77903(4)
c/nm	0.55437(2)	0.55167(9)	0.55137(9)	0.55000(8)
R_{wp}/%	11.1	12.6	12.2	12.4
s	1.25	1.18	1.25	1.28
$x_{(Ca,R)}$	0.000(2)	0.0134(4)	0.0150(3)	0.0139(4)
$z_{(Ca,R)}$	0.001(1)	0.029(8)	−0.001(1)	−0.003(1)
x_{O1}	0.50(1)	0.493(3)	0.496(2)	0.492(3)
z_{O1}	0.061(3)	0.074(7)	0.051(6)	0.082(7)
x_{O2}	0.249(8)	0.226(3)	0.226(3)	0.234(7)
y_{O2}	0.493(5)	0.516(3)	0.532(2)	0.514(4)
z_{O2}	0.259(5)	0.245(6)	0.238(4)	0.238(9)
$B_{(Ca,R)}$/nm^2	0.0062(2)	0.0070(3)	0.0078(3)	0.0095(4)
$B_{(Mn,Ti)}$/nm^2	0.0028(3)	0.0031(4)	0.0035(4)	0.0027(4)
B_{O1}/nm^2	0.002(3)	0.006(2)	0.007(1)	0.014(2)
B_{O2}/nm^2	0.009(2)	0.006(2)*	0.007(1)*	0.014(2)*

Space group *Pnma*; (Sr, R) and O1 in 4c (x, 1/4, z), (Mn, Ti) in 4b (0, 0, 1/2), and O2 in 8d (x, y, z);

* It was calculated having assumed that the value of B_{O2} was equal to the value of B_{O1}

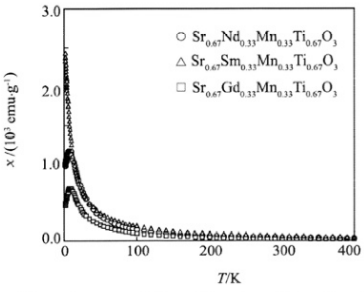

Fig.8 Magnetic susceptibility of $Sr_{0.67}Ln_{0.33}Mn_{0.33}Ti_{0.67}O_3$ for Ln = Nd, Sm, and Gd as a function of temperature

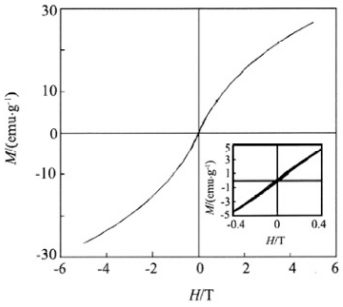

Fig.9 Magnetization curve of $Sr_{0.67}Nd_{0.33}Mn_{0.33}Ti_{0.67}O_3$ against the applied magnetic field at 5 K

Acknowledgement: We thank Professor Y. Hinatsu for his helpful discussion on magnetic properties.

References:

[1] Urushibara A, Morimoto Y, Arima T, et al. Insulator-metal transition and giant magnetoresistance in $La_{1-x}Sr_xMnO_3$[J]. Phys. Rev., 1995, B51: 14103.

[2] Mahesh R, Mahendiran R, Raychaudhuri A K, et al. Effect of the internal pressure due to the A-site cations on the giant magnetoresistance and related properties of doped rare earth manganates, $Ln_{1-x}A_xMnO_3$ (Ln = La, Nd, Gd, Y; A = Ca, Sr, Ba, Pb) [J]. J. Solid State Chem., 1995, 120: 204.

[3] Huhtinen H, Laiho R, Lisunov K G, et al. Critical behavior of magnetoresistance near the metal-insulator transition of $La_{0.7}Ca_{0.3}MnO_3$[J]. J. Magn. Magn. Mater., 2002, 238: 160.

[4] Zheng L Q, Fang Q F. Magnetoresistance behavior in $La_{0.7}Ca_xMnO_3$ (x = 0.1 ~ 0.3) and La_yMnO_3 (y = 0.67 ~ 0.9) bulk materials [J]. Phys. Stat. Sol (a), 2001, 185: 267.

[5] McCarroll W H, Ramanujachary K V, Fawvett Ian D, et al. Electrical and magnetic properties of strontium substituted lanthanum manganate perovskitc crystals prcpared using fused salt electrolysis [J]. J. Solid State Chem., 1999, 145: 88.

[6] Ramanujachary K V, Swamy C S. Preparation and characterization of La_2TiMnO_6 [J]. Indian J. Chem., 1981, 20A: 96.

[7] Kamegashira N, Nakajima N, Watanabe K, et al. Synthesis and crystal structure of Sm_2MnTiO_6 [J]. J. Alloys and Compounds, 2000, 311: 74.

[8] Kamegashira N, Nakajima N, Watanabe K, et al. Synthesis, crystal structure and magnetic properties of a new compound Eu_2MnTiO_6 [J]. Int. J. Materials and Product Technology, SPM1, 2001, 1(Special Issue): 139.

[9] Kamegashira N, Kobayashi M, Saito J. Synthesis, crystal structure and some properties of Ln_2MnTiO_6 phases (Ln = rare earth) [J]. Frontiers of Solid State Chemistry, ed. By Feng S H, Chen J S, Worlds Scientific, 2002. 47.

[10] Nakano H, Nakajima N, Shirakami T, et al. Crystal structure of a new oxide, Nd_2TiMnO_6 [J]. Mat. Res. Bull., 1999, 34: 1851.

[11] Haque Md T, Nakajima N, Watanabe K, et al. Structure, magnetic and thermal properties of Gd_2MnTiO_6 [J]. Mater. Chem. Phys., 2003, 80: 676.

[12] Nakano H, Kamegashira N, Urabe K. Structure analysis of a new oxide Yb_2TiMnO_6 [J]. Mat. Res. Bull., 2001, 36: 57.

[13] Havinga E E. Magnetic interactions between Mn^{3+} ions in perovskites [J]. Philips Res. Rept., 1966, 21: 432.

[14] Lotgering F K. On the double-exchange interactions in $La_{1-x}Ba_xMnO_3$ [J]. Philips Res. Repts., 1970, 25: 8.

[15] Elemans J B A A, Van Laar B, Van Der Veen K R, et al. The crystallographic and magnetic structures of $La_{1-x}Ba_xMn_{1-x}Me_xO_3$ (Me = Mn or Ti) [J]. J. Solid State Chem., 1971, 3: 238.

[16] Taguchi H, Sonoda M, Nagao M, et al. Role of tetravalent ion in metal-insulator transition in $(La_{0.1}Ca_{0.9})(Mn_{1-x}Ti_x)O_3$ [J]. J. Solid State Chem., 1996, 126: 235.

[17] Kobayashi M, Yamaguchi M, Kamegashira N. Refinement of crystal structure of $MLaMnTiO_6$ (M = Ba, Sr) and $CaSmMnTiO_6$ [A]. International Symposium on Designing, Processing and Properties of Advanced Engineering Materials [C]. 1997.505.

[18] Kobayashi M, Katsuraya R, Kurita S, et al. Synthesis and crystal structure of (Ca, R)(Mn, Ti)O_3 (R, Rare earth) [J]. J. Alloys and Compounds, 2006, 408 - 412: 1173.

[19] Izumi F. Rietan-A software package for the Rietveld analysis and simulation of X-ray and neutron diffraction patterns [J]. J. Crystallogr. Jpn. 1985, 27: 23.

[20] Izumi F. Rietveld analysis of X-ray and neutron diffraction patterns [J]. J. Mineral. Soc. Jpn., 1985, 17: 37.

Key Engineering Materials Vols. 321-323 (2006) pp 1695-1698
online at http://www.scientific.net

Thermal Diffusivity and Phase Transition of Rare Earth Manganites

Migaku Kobayashi[1,2,a], Hirohisa Satoh[1,b], Yoshihiko Hiyoshi[1],
Naoki Kamegashira[1,c], Doh-Jae Lee[3] and Hee-Joon Kim[4,d]

[1]Department of Materials Science, Toyohashi University of Technology, Tempaku-cho, Toyohashi, 441-8580, Japan

[2] Present address: Department of Chemistry and Biochemistry, Numazu College of Technology, Ooka, Numazu, 410-8501 Japan

[3]Chonnam National University, Department of Metallurgical Engineering, Kwang-Ju, Korea

[4]Departmernt of Ecological Engineering, Toyohashi University of Technology, Tempaku-cho, Toyohashi, 441-8580 Japan

[a]m.kobayashi@numazu-ct.ac.jp, [b]hsatoh@tutms.tut.ac.jo,
[c]nkamegas@tutms.tut.ac.jp, [d]kim@eco.tut.ac.jp

Keywords: Rare earth manganites; Phase transition; Oxygen nonstoichiometry; Thermal diffusivity.

Abstract. Thermal diffusivity of nonstoichiometric $PrMnO_3$ and $NdMnO_3$ phases were measured by laser flash method from room temperature to 1100 K, in addition to the data of electrical conductivity, thermal analysis and high temperature X-ray diffractometry to detect the phase transition. The thermal diffusivity curve varied with increasing temperature and showed a clear anomaly with a sudden dip at the phase transition temperature. The transition temperature decreases with oxygen nonstoichiometry in each phase.

Introduction

$LnMnO_3$ (Ln = rare earth element) has a perovskite-type structure for Ln = La – Dy and a hexagonal structure for a smaller ionic size of rare earths [1]. These compounds and their solid solutions with alkaline earth elements have been extensively studied in recent years because of their potential applications to electrode materials for solid state fuel cell systems [2] and to magnetoresistive sensors [3-6].

In general $LnMnO_3$ (Ln=La– Dy) with the perovskite-type structure belongs to an orthorhombic system near stoichiometric composition and this orthorhombic distortion is caused by the Jahn-Teller effect of trivalent Mn ion in the oxygen octahedral field in the crystal structure [7]. This effect for the crystallographic distortion is easily liberated to a phase with a higher symmetry by the thermal energy and in the case of $LaMnO_3$ phase it becomes a rhombohedral system by the phase transition at high temperature and the transition temperature decreases with oxygen nonstoichiometry [8,9]. At the phase transition several physical properties drastically change [10-12]. $PrMnO_3$ [13-15] and $NdMnO_3$ [16] have the similar phase transition at high temperatures near 1000 and 1100K, respectively. The thermal diffusivity of nonstoichiometric $LaMnO_{3+x}$ phase also has an anomaly at the phase transition temperature from orthorhombic to rhombohedral systems as was reported by the present authors [12].

In this paper the phase transition of praseodymium manganites was studied in detail with an emphasis on oxygen nonstoichiometry by the measurements of electrical conductivity, DTA and thermal diffusivity with the support of high temperature X-ray diffractometry. The thermal diffusivity of $NdMnO_3$ phase was also measured in this study and the phase transition was detected and compared with the results from the other methods.

Experimental

The $PrMnO_3$ and $NdMnO_3$ specimens were prepared by the conventional ceramic method by heating at 1523 K in purified Ar for 3days from rare earth sesquioxide and Mn_2O_3 as the starting

materials as in the previous study [15-18]. The formation of the single phase was identified by X ray diffractometry. The adjustment of oxygen nonstoichiometry [19] was taken by equilibrating the specimen at 1273 K for 2 days under various oxygen partial pressures [20]. The oxygen partial pressure was generated by buffer method of mixing gases of H_2/CO_2 and /or Ar/O_2 [16]. It is found from this thermogravimetric analysis (TGA) that these phases decompose into each constituent sesquioxide and MnO below a certain limiting partial pressure of oxygen at each temperature. Assuming that under these low oxygen partial pressures both decomposed phases, Pr_2O_3 and MnO, can be taken to be stoichiometric [21], then the detailed data of degree of oxygen nonstoichiometry of $PrMnO_3$ phase could be determined from the weight change similar to the preparation for orthorhombic $LaMnO_3$ and $NdMnO_3$ phases [16,20]. The volume of the unit cell obtained from a variation of the lattice constants with oxygen nonstoichiometry of $PrMnO_{3+x}$ decreases as the oxygen nonstoichiometry (x) increases because of increase of the content of a smaller size of tetravalent manganese ion.

Thermal diffusivity was measured by laser flash method. The specimen had a pellet type with a diameter of 10mm and 2mm thickness. The temperature rise on one side of the pellet of the specimen was measured with a radiation thermometer after irradiation of laser pulse on the other side at each temperature. The value of thermal diffusivity could be calculated via the least squares method by substituting 20 sets of time and temperature terms together with the absorption coefficient term. The experimental details of the laser flash technique were almost similar as in the previous work [12]. The electrical conductivity was measured by dc four-probe method.

Results and Discussion

The results of thermal diffusivity of $PrMnO_{3+x}$ and $NdMnO_{3+x}$ are shown in Figs. 1 and 2, respectively. The thermal diffusivity of both phases decreased with an increase of temperature in low temperature region and there exists an anomaly for each specimen at high temperature, which should correspond to the phase transition. The behavior of sink in thermal diffusivity curve was also seen in the case of $LaMnO_{3+x}$ near the transition temperature [12].

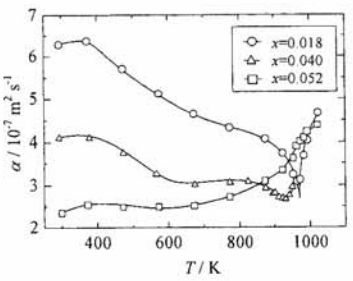

Fig. 1 Thermal diffusivity of $PrMnO_{3+x}$.

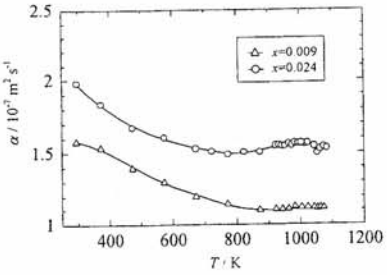

Fig. 2 Thermal diffusivity of $NdMnO_{3+x}$.

To detect the phase transition temperature of $PrMnO_{3+x}$ the electrical conductivity was measured for nonstoichiometric specimen as is shown in Fig. 3. The so-called Z-type jump in the conductivity curve is seen against reciprocal temperature and from the slope the activation energy (~0.2 eV) was derived for these semiconducting materials. The conductivity increases with oxygen nonstoichiometry, which suggests that this phase has a p-type semiconducting property. The transition temperature, which is determined from the point of the steepest slope during Z-type jump, decreases with oxygen nonstoichiometry. The width of the jump in the conductivity curve also decreases with the oxygen nonstoichiometry. Similar tendency is seen in DTA curve for nonstoichiometric $PrMnO_{3+x}$ phase as shown in Fig. 4, where it is clearly seen that thermal anomaly corresponding to the transition temperature decreases with oxygen nonstoichiometry and the enthalpy change for the phase transition calculated from the peak area decreases with oxygen

nonstoichiometry. The entropy change for the phase transition of $PrMnO_{3+x}$ evaluated from the enthalpy value divided by the transition temperature decreases with oxygen nonstoichiometry by weakening of the Jahn-Teller effect.

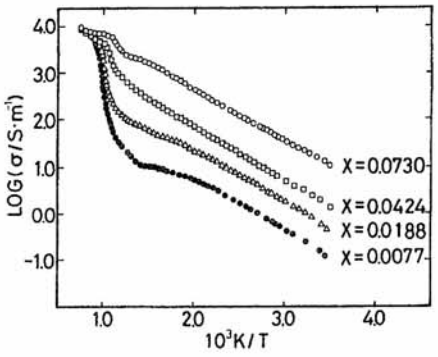

Fig. 3 Electrical conductivity of $PrMnO_{3+x}$.

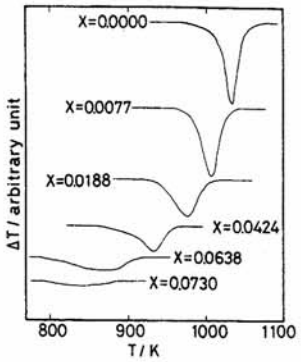

Fig. 4 DTA curves of $PrMnO_{3+x}$.

Thus the variation of the phase transition temperature of $PrMnO_{3+x}$ and $NdMnO_{3+x}$ including these data are shown in Figs. 5 and 6 as a function of oxygen nonstoichiometry. The detailed structural study of $PrMnO_3$ phase showed that the orthorhombic phase changed to the quasi cubic phase above 945K by Pollert et al [13,14]. In this study the transition temperature for each phase of $PrMnO_{3+x}$ and $NdMnO_{3+x}$ decreases with oxygen nonstoichiometry by all kinds of measurements as explained by the liberation from the Jahn-Teller effect.

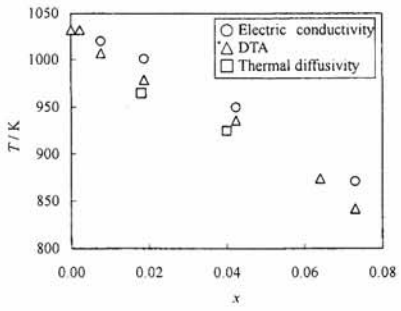

Fig. 5 Transition temperature of $PrMnO_{3+x}$.

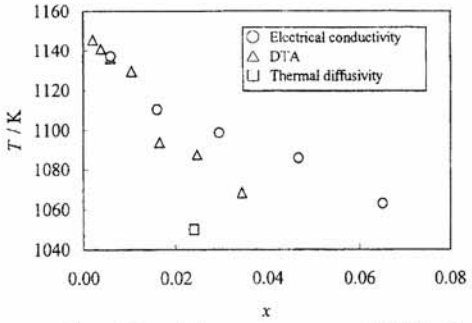

Fig. 6 Transition temperature of $NdMnO_{3+x}$.

The transition behavior was also identified by the high temperature X-ray diffractometry in the present study. The diffraction patterns unambiguously changed the symmetry below and above the transition temperature. Several peaks characteristic of the orthorhombic phase at room temperature systematically combined to higher symmetric patterns at high temperature and all of these diffraction patterns could be indexed based on the rhombohedral symmetry at 990K.

Summary

1. The existence of the phase transition was detected by thermal diffusivity, electrical conductivity, DTA and high temperature X-ray diffractometry for $PrMnO_3$.
2. $PrMnO_3$ has the phase transition near 850-1000K from orthorhombic to rhombohedral

structures.
3. Thermal diffusivity of $NdMnO_3$ phase was also measured above room temperature.
4. The transition temperature of $PrMnO_3$ phase decreases with oxygen nonstoichiometry like $LaMnO_3$ and $NdMnO_3$ phases.

Acknowledgements

The authors wish to thank Prof. K. Inoue for his helpful discussion.

References

[1] C. P. Khattak and F. F. A. Wang, in: K. A. Gschneidner, Jr., L. Eyring (Eds.), *Handbook on the Physics and Chemistry of Rare Earths*, North-Holland, Amsterdam, 1979, p.525, Chap. 29.

[2] A. Martinez-Jaurez, L. Sanchez, E. Chinarro, P. Recio, C. Pascual and J. R. Jurado: Solid State Ionics, 135 (2000) 525.

[3] A. J. Millis, P. B. Littlewood and B. I. Fhraiman: Phys. Rev. Lett., 74 (1995) 5144.

[4] Y. Tokura, A. Urushibara, Y. Moritomo, T. Arima, A. Asamitsu, G. Kido and N. Furukawa: J. Phys. Soc. Japan, 63 (1994) 3931.

[5] A. Urushibara, Y. Moritomo, T. Arima, A. Asamitsu, G. Kido and Y. Tokura: Phys. Rev., B51 (1995) 14103.

[6] Y. Yamada, O. Hino, S. Nohdo and R. Kanao: Phys. Rev Lett. 77 (1996) 904.

[7] A. Wold, R. J. Arnott and J B. Goodenough: J. Phys. Chem. Solid, 9 (1956?) 176.

[8] A. Wold and R. J. Arnott: J. Phys. Chem. Solids, 9 (1959) 176.

[9] Md. T. Haque, H. Satoh, N. Kamegashira: Mat. Lett. 58 (2004) 1571.

[10] G. H. Jonker, J. Appl. Phys., 22 (1956) 707.

[11] H. Satoh, M. Takagi, K. Kinukawa and N. Kamegashira: Thermochimica Acta, 299 (1997) 123.

[12] M. Kobayashi, H. Satoh, N. Kamegashira and K. Inoue: J. Alloys and Compounds, 192 (1993) 93.

[13] E. Pollert and Z. Jirák: J. Solid State Chem., 35 (1980) 262.

[14] E. Pollert, S. krupička and E. Kuzmičová: J. Phys. Chem. Solids, 43 (1982) 1137.

[15] N. Kamegashira and Y. Miyazaki: J. Mater. Sci. Lett. 4 (1985) 103.

[16] N. Kamegashira and Y. Miyazaki: Mat. Res. Bull. 19 (1984) 176.

[17] T. Mori, K. Aoki, N. Kamegashira, T. Shishido, T. Fukuda: Mat. Lett. 42 (2000) 387.

[18] T. Mori, N. Kamegashira, K. Aoki, T. Shishido, T. Fukuda: Mat. Lett. 54 (2002) 238.

[19] V. A Cherepanov, L. Yu. Barkhatova, A. N. Petrov and V. I. Voronin: J. Solid State Chem., 118 (1995) 53.

[20] N. Kamegashira, Y. Miyazaki and H. Yamamoto: Mater. Chem. Phys., 11 (1984) 187.

[21] P. Kofstad: *Nonstoichiometry, Diffusion, and Electrical Conductivity in Binary Metal Oxides* (Wiley-Interscience, New York, 1972).

journal

J. Am. Ceram. Soc., **90** [4] 1342–1345 (2007)
DOI: 10.1111/j.1551-2916.2006.01314.x

In situ Transmission Electron Microscopy Observation of Multiple Phase Transition in $BaGd_2Mn_2O_7$

Hiromi Nakano†

Electron Microscope Laboratory, Ryukoku University, Otsu 520-2194, Japan

Nobuo Ishizawa

Ceramics Research Laboratory, Nagoya Institute of Technology, Tajimi 507-0071, Japan

Naoki Kamegashira

Department of Materials Science, Toyohasi University of Technology, Toyohashi 441-8580, Japan

Masatomo Yashima

Department of Materials Science and Engineering, Tokyo Institute of Technology, Yokohama, 226-8502, Japan

***In situ* transmission electron microscopy observation revealed that $BaGd_2Mn_2O_7$ undergoes several phase transitions upon heating. The orthorhombic *Pnnm* phase (I) at room temperature was transformed into a tetragonal $P4_2/mnm$ (II) at around 420 K via an intermediate phase. On further heating, the other phase (III) nucleated in the phase II matrix at 623 K and grew until covering the whole inspected region by 723 K. Phase III has a 1.5% lattice mismatch along *c* compared with phase II, and presumably has a monoclinic symmetry. The transition between II and III was of the first order.**

I. Introduction

The rare-earth manganite $BaLn_2Mn_2O_7$ (Ln = rare-earth element) has a $Sr_3Ti_2O_7$-type layered perovskite structure with double-block oxygen octahedra belonging to the Ruddlesden–Popper-type homologous series $AO(ABO_3)_2$.[1] Deschizeaux–Cheruy and Joubert were the first to synthesize these manganites (Ln = Nd–Gd) in a N_2 atmosphere.[2] After that, many phases were reported for the oxides, depending on the synthesis or annealing conditions.[3–12] High-temperature X-ray diffraction (XRD) analysis, and electrical conductivity and thermal analyses,[3,13,14] revealed phase transitions for the Sm, Eu, Gd, Nd, and Tb compounds, which undergo a transition from orthorhombic to tetragonal on heating. Kamegashira has suggested that the tetragonal $I4/mmm$ structure is stable at high temperatures.[15] The transition temperatures tend to increase with decreasing ionic radii of the Ln cations.[14] In the Gd–manganite, the tetragonal phase is reported to transform into another orthorhombic form at 773 K on heating.[16] This is contradictory to the conventional understanding about the successive phase transition series common in perovskite-related families whose symmetries are expected to change from lower to higher with increasing temperatures and vice versa. In the present study, we report phase transitions of $BaGd_2Mn_2O_7$ observed mainly by a transmission electron microscope (TEM) equipped with a thermal holder.

Manuscript No. 21842. Received May 29, 2006; approved June 27, 2006.
†Author to whom correspondence should be addressed. e-mail: hiromi@rins.ryukoku.ac.jp

II. Experimental Procedure

The starting powders of $BaCO_3$, Ln_2O_3, and Mn_2O_3 were mixed together and calcined at 1623 K in an Ar atmosphere for 2 days. The product was confirmed as a single phase of $BaGd_2Mn_2O_7$ by powder XRD analysis. The product was then pulverized and hydrostatically pressed into a rod. Single crystals were grown by the floating zone (FZ) method in an Ar atmosphere. The procedure of crystal growth is detailed in the previous paper.[6] The as-grown crystals were annealed at 493 K for 10 days in an Ar atmosphere with subsequent gradual cooling. The crystals were examined by the four-circle single-crystal diffractometer Rigaku-AFC7R (Rigaku, Tokyo, Japan).

A fragment of the crystal was crushed and scooped onto a copper mesh with carbon-coated microgrids. The *in situ* TEM observation was performed on a thermal stage in the temperature range from 293 to 1073 K (JEM-2000EX, EM-SHU2 specimen holder, JEOL, Tokyo, Japan). The temperature was controlled manually. The heating rate was approximately 600 K/h.

III. Results and Discussion

The as-grown crystal of $BaGd_2Mn_2O_7$ showed the tetragonal $P4_2/mnm$ symmetry.[6] It is known that the crystals grown by the FZ method often show a meta-stable high-temperature phase at room temperature due to its rather high cooling procedure. The as-grown crystals were thus heat treated at 493 K for 10 days in an Ar atmosphere. By this procedure, the crystals transformed from meta-stable tetragonal to orthorhombic (phase I) at room temperature. Table I tabulates the lattice parameters of the as-grown and annealed crystals. The orthorhombic phase was

Table I. Lattice Parameters of $BaGd_2Mn_2O_7$

	As-grown crystal	Annealed crystal
Symmetry	Tetragonal $P4_2/mnm$ [6]	Orthorhombic *Pnnm*
Lattice parameters, *a* (nm)	0.5541 (3)	0.5505 (4)
Lattice parameters, *b* (nm)	0.5541 (3)	0.5505 (5)
Lattice parameters, *c* (nm)	2.004 (5)	2.0182 (4)

Table II. Atomic Parameters of $BaGd_2Mn_2O_7$ with *Pnnm*

Atom	*x*	*y*	*z*
Ba	0.24389 (8)	0.7437 (2)	0
Gd	0.27031 (5)	0.22936 (9)	0.31654 (2)
Mn	0.2539 (1)	0.2459 (3)	0.10304 (5)
O1	0	0	0.1107 (5)
O2	0	0	0.3878 (4)
O3	0	0.5	0.0988 (4)
O4	0	0.5	0.3764 (5)
O5	0.271 (2)	0.227 (3)	0
O6	0.197 (1)	0.302 (2)	0.2087 (4)

$RI = 0.072$, $S = 1.021$

stable from room temperature up to approximately 450 K. The space group for the phase I was supposed to be *Pnnm* from the selected area electron diffraction (SAED) data. The atomic parameters of the structure assuming *Pnnm* were refined by an X-ray four-circle diffractometer, and are shown in Table II.

Figure 1 shows the SAED patterns along the [001] zone axis at various temperatures. At around 333 K, the orthorhombic phase I started to transform into an intermediate phase with a rather complex diffraction pattern as shown in Fig. 1(b). Then, the intermediate phase transformed into the tetragonal phase II at approximately 420 K. The space group of the phase II was supposed to be $P4_2/mnm$. The phase II was stable between 420 and 623 K. These results agree with the high-temperature XRD and electrical conductivity results.[13] With increasing temperature, a new phase III nucleated in the phase II matrix at 623 K. The SAED pattern at 623 K can be interpreted as a mixture of phases II and III. At 723 K, phase II finally disappeared and the crystal was composed of phase III.

The coexistence of phase II and III at 623 K was also confirmed by the dark-field (DF) images. Figure 2 shows the DF images obtained from the encircled spots in the SAED pattern at 623 K. The crystallographic orientation relationship on the [001] zone is given schematically in Figs. 2(d)–(f). The composite diffraction pattern can be decomposed into (d), (e), and (f). The coherency between the phases II and III was good on the zone. Phase III is sheath shaped, several tens of nanometers in width and much longer in length.

Figure 3 shows TEM images at 623 and 793 K, respectively. The insets correspond to SAED patterns. The sheath-shaped regions of phase III grew on further heating at a rate of 20 K/min above 793 K. Figure 3(b) shows two large single-crystal phase III domains, indicating that the nucleation and growth of phase III in the phase II matrix have been completed at that temperature. The two neighboring phase III domains exchange the *a* and *b* axes with each other, being similar to the relationship of 90° domains in the perovskite-type crystals.[17]

A small misfit in the cell dimension along *c* was observed between phases II and III, as shown in Fig. 4. No such significant misfit was observed from room temperature up to approximately 600 K. This means that the transition between phases I (*Pnnm*) and II ($P4_2/mnm$) is hardly detectable in the [100] zone. Above 600 K, however, a composite diffraction pattern started to appear, as shown in Fig. 4(b). The pattern can be de-

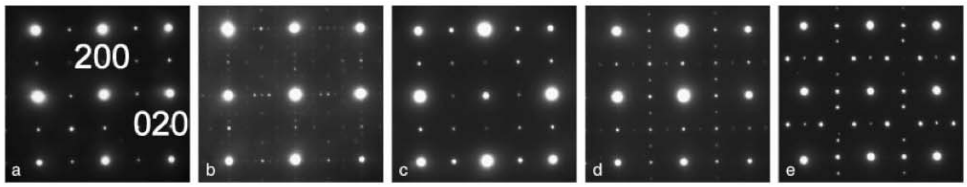

Fig. 1. Selected area electron diffraction patterns of $BaGd_2Mn_2O_7$ along the [001] zone axis taken *in situ* at various temperatures: at (a) RT for phase I, (b) 373 K for intermediate phase, (c) 420 K for phase II, (d) 623 K for phase II+III, and (e) 723 K for phase III.

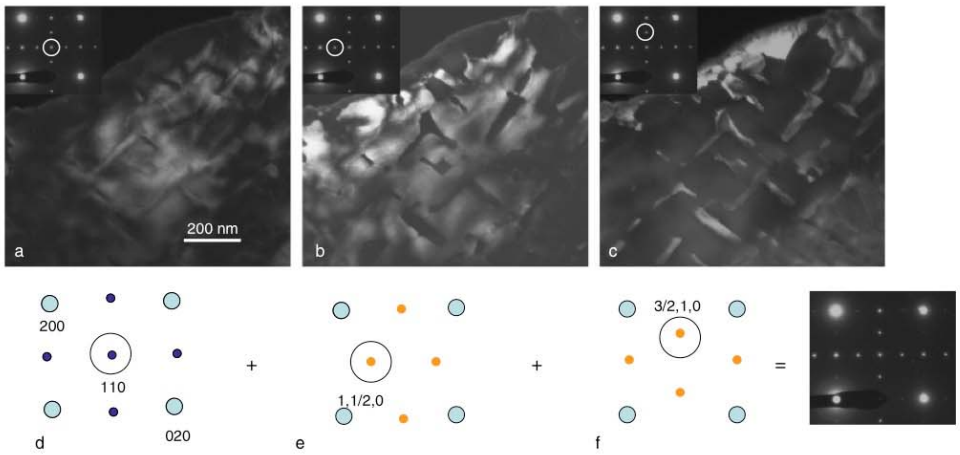

Fig. 2. Dark-field images produced by encircled spots in the selected area electron diffraction pattern taken from the [001] zone axis. Illustrations (d)–(f) show the diffraction patterns at each phase. (a) and (d) tetragonal phase II, (b) and (e) phase III, (c) and (f) phase III rotated by 90°.

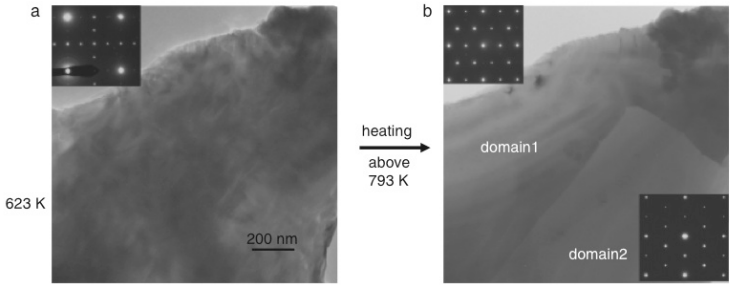

Fig. 3. Transmission electron microscope images of $BaGd_2Mn_2O_7$ taken from the [001] zone axis at 623 K (a), and 793 K (b). Insets show the corresponding selected area electron diffraction patterns.

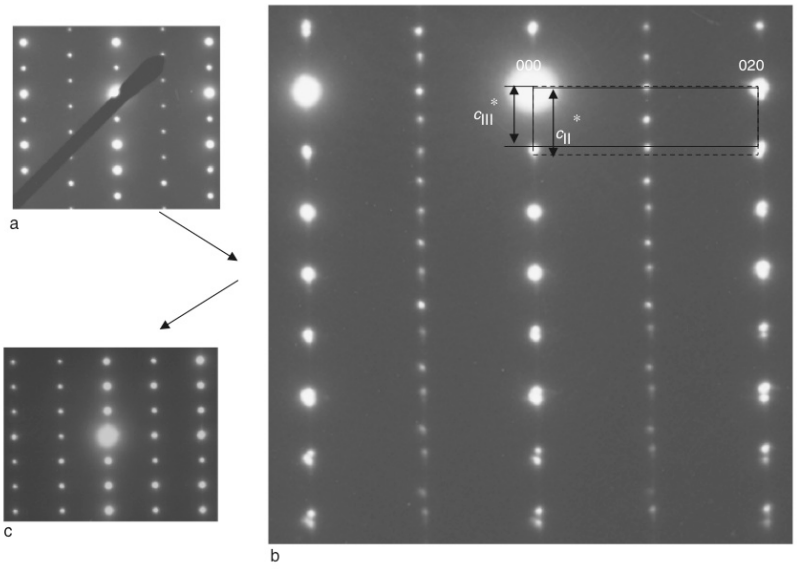

Fig. 4. Changes of selected area electron diffraction patterns taken from the [100] zone for the $BaGd_2Mn_2O_7$ axis by heating. (a) Phase I at room temperature, (b) intermediate phase (phase II+phase III) at 673 K, and (c) phase III at 1023 K.

composed into two plane lattices: a face-centered rectangular lattice and a primitive rectangular lattice with half the repetition length along *b*. The former suggests the presence of phase II, and the latter corresponds to phase III. The split reflections at 673 K indicate that the *c* length of phase III is 1.5% longer than that of phase II. The *c* length of phase III remained almost constant with increasing temperature. The phase II disappeared above 800 K. No significant change was observed in the specimen on further heating up to 1023 K, the highest temperature available for the present *in situ* TEM observation.

The I–II transition at around 420 K may accompany tilts of the MnO_6 octahedra because the symmetries suggest a change of the octahedral tilt system from (Φ00) (0Φ0) for $P4_2/mnm$ to ($\Phi_1\Phi_2$0) ($\Phi_2\Phi_1$0) for *Pnnm*.[13,18] On the other hand, the nucleation-growth process observed in the II–III transition suggested that the transition is of the first order. Actually, the repeated *in situ* experiments revealed that the transformation speed is temperature dependent. The II–III transition point could be related to the inflection of the electrical conductivity curve against temperature at approximately 620 K.[13] From the SAED patterns, phase III seems to have a close relation with the monoclinic $B112/m$ structure that was observed in $BaTb_2Mn_2O_7$ upon annealing.[12] It is expected that one or more phase transitions may occur at temperatures above 1023 K because the symmetry of phase III is still much lower than $F4/mmm$ assumed for the prototype.

IV. Conclusion

Phase transitions in $BaGd_2Mn_2O_7$ have been studied by *in situ* TEM observation. The orthorhombic phase I (*Pnnm*) transformed into the tetragonal phase II ($P4_2/mnm$) at roughly above 420 K. Then, phase III nucleated in the matrix of phase II at 623 K, and grew to cover the whole region under inspection by 723 K. Phase III has approximately 1.5% large cell size along the *c* axis compared with phase II. The transition between the phases II and III was considered to be of the first order.

Acknowledgment

This work was partially supported by a Grant-in Aid for Scientific Research (c) No. 18560662 by the Japan Society for the Promotion of Science.

References

[1]N. Ishizawa, "Layered Perovskite-Structure Classification," *Ceramics*, **31** [5] 409–13 (1996).

[2]M. N. Deschizeaux-Cheruy and J. C. Joubert, "Donnees cristallographiqes sur une nouvelle serie de manganites mixtes de terre rare et d'alcalino-terreux," *J. Solid State Chem.*, **40**, 14–9 (1981).

[3]N. Kamegashira, H. Nakano, G. Chan, and J. Meng, "Phase Behavior of Rare Earth Manganites," *J. Rare Earths*, **22** [5] 582–5 (2004).

[4]J. Meng, H. Satoh, and N. Kamegashira, "Crystal Structure Refinement of Tetragonal $BaTb_2Mn_2O_7$," *J. Alloys Compd.*, **244**, 75–8 (1996).

[5]N. Kamegashira, J. Meng, T. Murase, K. Fujita, H. Satoh, T. Shishido, and T. Fukuda, "Crystal Growth and Structure Analysis of Rare Earth Mangantites with Layered Perovskite Type"; pp. 181–6 in *10th International Ceramics Congress Part A*, Edited by P. Vincenzini. Florence, 2002.

[6]N. Kamgegashira, J. Meng, T. Mori, A. Murase, H. Satoh, T. Shishido, and T. Fukuda, "Growth and Structure Analysis of Single Crystal of Tetragonal $BaGd_2Mn_2O_7$ with a Superlattice Structure," *Mater. Lett.*, **57**, 1941–4 (2003).

[7]S. Ueno, N. Kamegasira, H. Nakano, and K. Enami, "Crystal Structure of Layered Perovskite, Barium Europium Manganese Oxide [$BaEu_2Mn_2O_7$]," *Mater. Res. Bull.*, **31**, 497–502 (1996).

[8]S. Ueno and N. Kamegashira, "Crystal and X-Ray Diffraction Data for Orthorhombic $BaNd_2Mn_2O_7$ Phase," *Powder Diffraction*, **12** [2] 103–5 (1997).

[9]N. Kamegashira, A. Shimono, and M. Hirokawa, "Synthesis and Transition of the Orthorhombic $BaGd_2Mn_2O_7$," *Mater. Chem. Phys.*, **24**, 389–97 (1990).

[10]J. Meng, J. Wang, J. Feng, H. Satoh, and N. Kamegashira, "Structural Phase Transition in the Layered Perovskite Compound $BaTb_2Mn_2O_7$"; pp. 159–65 in *Proceedings of the International Symposium on Solid State Chemistry*, Edited by S. H. Feng and J. S. Chen. World Scientific, China, 1996.

[11]N. Kamegasira, J. Meng, K. Fujita, H Satoh, T. Shishido, and K. Nakajima, "Study on the Phase Behavior on $BaEu_2Mn_2O_7$ Through Heat Treatment of a Single Crystal," *J. Alloys Compd.*, **408–412**, 603–607 (2006).

[12]N. Kamegashira, H. Satoh, J. Meng, and T. Mikami, "Structure Determination of a New Phase of Monoclinic $BaTb_2Mn_2O_7$," *J. Alloys Compounds*, **374**, 173–6 (2004).

[13]H. Nakano, N. Kamegashira, and N. Ishizawa, "In-Situ Observation of Structural Transition in Rare Earth Manganites by TEM"; in *Proceedings of 6th Pacific Rim Conference on Ceramic of Glass*, Edited by M. Singh, in press.

[14]H. Nakano, H. Satoh, N. Kamegashira, and N. Ishizawa, "Phase Behavior of Layered Manganites $BaLn_2Mn_2O_7$ (Ln = Rare Earth)"; in *Proceedings of IC-TMC15*, Kyoto, 2006, *Phys. Stat. Sol.* (c) **3**(8), 2812–15 (2006).

[15]N. Kamegashira, "Phase Transition and Nonstoichiometry of Rare Earth Magnaites," *Shokubai*, **31** [4] 222–6 (1989).

[16]J. Meng, P. R. China, N. Kamegashira, A. Murase, H. Satoh, H. Y. Wang, Q. B. Bo, and C. Peng, "Anomalous Structural Transition in Layered Perovskites $BaGd_2Mn_2O_7$ Compound"; pp. 397–401 in *Proceedings of International Journal of Materials and Product Technology, Special Issue, SPM 1*, INDERSCIENCE Edited by M. A. Dorgham, (2001).

[17]H. Nakano, N. Kamegashira, and K. Urabe, "In Situ Observation of Change in Domain Structure Due to Phase Transition in a Perovskite La_2MnGaO_6," *Mater. Res. Bull.*, **37**, 2107–15 (2002).

[18]K. S. Aleksandrov and J. Bartolome, "Octahedral Tilting Phases in Perovskite-Like Crystals with Slabs Containing an Even Number of Octahedral Layers," *J. Phys.: Condens. Matter*, **6**, 8219–35 (1994). □

phys. stat. sol. (c) **3**, No. 8, 2812 2815 (2006) / **DOI** 10.1002/pssc.200669508

Phase behavior of layered manganites $BaLn_2Mn_2O_7$ (Ln = rare earth)

Hiromi Nakano[*,1], **Hirohisa Satoh**[2], **Naoki Kamegashira**[2], and **Nobuo Ishizawa**[3]

[1] Ryukoku University, Seta Otsu, 520-2194, Japan
[2] Toyohasi University of Technology, Tempaku, Toyohashi, 441-4580, Japan
[3] Nagoya Institute of Technology, Asahigaoka, Tajimi, 507-0071, Japan

Received 13 February 2006, revised 3 April 2006, accepted 9 June 2006
Published online 4 September 2006

PACS 61.10.Nz, 68.18.Jk, 68.37.Lp

We have found that many phases appear in the layered manganites $BaLn_2Mn_2O_7$, depending on the synthesis and annealing conditions for each rare earth metal. The $BaLn_2Mn_2O_7$ phase, with a stoichiometric composition synthesized under low oxygen pressure, transforms into another structure upon heating. The transition temperature varies according to the rare earth ion. In the present paper, we summarized the relationship between the transition temperature and rare earth ions. We successfully observed *in-situ* multiple-phase transition of the manganite by thermal TEM. We found a first-order phase transition in Gd-manganite at a relatively high temperature, presumably caused by a change in the behavior of 3d electrons in the Mn^{3+} ion. We discuss here the structural transition in $BaLn_2Mn_2O_7$.

1 Introduction

The rare earth manganites $BaLn_2Mn_2O_7$ (Ln = rare-earth element) have the $Sr_3Ti_2O_7$-type layered perovskite structure with double-block oxygen octahedra that belong to the Ruddlesden-Popper-type homologous series $AO(ABO_3)_2$. Over several years, many phases have been identified in these oxides, depending on the synthetic or annealing conditions for each rare earth element [1]. These phases were determined by XRD, in which a structural transition appears as a peak split at around 30° in 2θ (diffraction angle by Cu Kα radiation) [1]. Recently, a single crystal of $BaLn_2Mn_2O_7$ (Ln = Eu or Gd) was successfully fabricated by the FZ method [2, 3]. Kamegashira *et al*. have found the phase transition, whereby the orthorhombic phase of $BaLn_2Mn_2O_7$ changed into a tetragonal phase upon heating, and the phase transition was examined by XRD, DSC and electron conductivity [4]. We recently succeeded in observing *in-situ* the structural change in $BaEu_2Mn_2O_7$ by thermal TEM [5].

In this experiment, to determine the nature of the phase transition in $BaLn_2Mn_2O_7$, the relationship between the transition temperature and rare earth ions was summarized. We focus on two types of phase transitions that were observed in $BaGd_2Mn_2O_7$ by thermal TEM.

2 Experimental procedure

$BaLn_2Mn_2O_7$ (Ln = Pr - Tb) was prepared from the starting materials $BaCO_3$, Ln_2O_3, and Mn_2O_3 by a ceramics method in Ar atmosphere. The single crystal was grown from the polycrystalline ceramic by a floating zone method in Ar atmosphere. The detailed procedure was described in previous papers [1, 3].

* Corresponding author: e-mail: hiromi@rins.ryukoku.ac.jp

In-situ observation was performed using a thermal stage in the range from room temperature to 723 K in a TEM (JEM-2000EX, EM-SHU2 specimen holder, JEOL). A carbon-coated microgrid mesh was annealed at above 723 K and used in the thermal TEM. The specimen was crushed and scooped onto a copper mesh with a carbon-coated microgrid.

3 Results and discussion

We have found that many different phases appear in the oxides, depending on the synthesis and annealing conditions for each rare earth element [1]. Table 1 shows the various phases in $BaLn_2Mn_2O_7$ (Pr - Tb) determined by XRD analysis. Some of these phases appeared during the phase transition induced by annealing. The phase transition was investigated in $BaLn_2Mn_2O_7$ for several years. The orthorhombic phase of $BaLn_2Mn_2O_7$ transformed into a tetragonal phase, as determined by XRD, DSC, and electrical conductivity, except in the case of Pr-manganite. These data are summarized for each rare earth element in Table 2. The transition temperatures tended to increase with decreasing ionic radius of the rare earth ion. The orthorhombic $BaLn_2Mn_2O_7$ phase was produced under low oxygen pressure conditions [4, 6]. Under other conditions, the orthorhombic phase was distorted in the case of oxides containing trivalent Mn ions with stoichiometric composition. This indicated that the orthorhombic phase was caused by the Jahn-Teller effect due to the Mn^{3+} ion. Kamegashira reported that the structure of layered manganite is stable as *I4/mmm* at high temperature [4]. In the structure of $BaLn_2Mn_2O_7$ with *I4/mmm*, Ba and rare-earth ions occupy different sites, namely 2b and 4e, respectively. The Ba site is 12-coordinate, while the rare earth site is 9-coordinate. The ionic radius of Ba^{2+} is 0.142 nm. The differences in ionic radius between Ba and rare-earth ions affect the structural distortion and crystal stability in the layered structure. The crystal distortion was controlled by tilting octahedra of MnO_6, as reported by Aleksandrov and Bartolome [12].

Table 1 Phases of $BaLn_2Mn_2O_7$, as determined by XRD.

Crystal structure	symmetry	Pr	Nd	Sm	Eu	Gd	Tb
Tetragonal	*I4/mmm*	●	●	○	○	○	○
Tetragonal	$P4_2/mnm$			●	●	●	
Orthorhombic	*Fmmm*		○	○	○	○	
Orthorhombic	*Immm*				○	○	○
Orthorhombic	*Cmcm*			○	○		
Monoclinic	*A2/m*			○	○	○	○

● Singe crystal (as-grown); ○ Poly crystal

In Gd-oxide, however, two transition temperatures were detected by XRD and DSC, as shown in Table 2. These corresponded to two types of phase transitions, namely, orthorhombic to tetragonal around 559 K and tetragonal to orthorhombic around 773 K [10], as revealed by XRD. The crystal symmetry was reduced again at relatively high temperatures. At 749 K, a large and sharp peak appeared in DSC data of $BaGd_2Mn_2O_7$, as reported by Meng [10].

We successfully observed *in-situ* the structural change by thermal TEM. Figure 1 shows the SAD pattern taken from the multi-phase $BaGd_2Mn_2O_7$ by heating on a thermal TEM holder. As starting material, a single crystal with an orthorhombic structure was used, produced by annealing of the as-grown crystal, followed by slow cooling. In Fig. 1 (a), the pattern shows the orthorhombic phase with *Pnnm* that was determined by XRD and electron diffraction method. In the case of single crystals of $BaGd_2Mn_2O_7$, the as-grown crystal possessed a tetragonal structure ($P4_2/mnm$) with $\sqrt{2}a$ cell size of archetype *I4/mmm* [3]. The orthorhombic phase transformed into a tetragonal phase at around 420 K, as shown in Fig. 1 (c). An intermediate phase was observed between orthorhombic and tetragonal, as shown in Fig. 1(b). The phase transition was controlled by tilting MnO_6 octahedra [12]. Therefore, the intermediate phase might

be caused by various tilting octahedra during the phase transition. The patterns in (a) and (c) taken from the [001] axis seemed to be the same. Accutually, the pattern changed from the orthorhombic symmetry (*Pnnm*) to tetragonal symmetry ($P4_2/mnm$) in the symmetrical subgroup.

Table 2 Transition temperatures from orthorhombic to tetragonal in $BaLn_2Mn_2O_7$

Rare earth ionic radii (nm) [13]		Transition temperature		
		XRD results / K	DSC results / K	Electrical conductivity results / K
Pr	0.114	-	-	-
Nd [7]	0.112	523	-	-
Sm [8]	0.109	520	525	525
Eu [9]	0.107	560	550	550
Gd [10]	0.106	559, 773	617, 749	650
Tb [11]	0.104	725	745	755

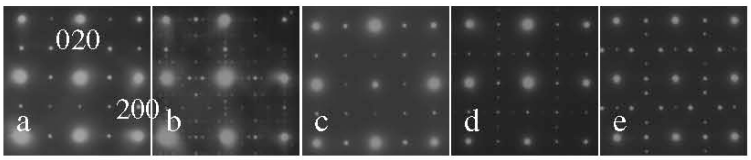

Fig. 1 Changes in SAD patterns of $BaGd_2Mn_2O_7$ in thermal TEM at (a) room temperature, (b) 333 K, (c) 420 K, (d) 623 K, and (e) 723 K.

In subsequently, a complex pattern appeared at around 623 K, as shown in Fig. 1(d). This phase was composed of a matrix with tetragonal structure and a new phase with orthorhombic structure. The complex phase changed into a single orthorhombic phase at around 723 K, in which 110 reflection and their equivalent reflections disappeared. The diffraction pattern in Figure 1(e) was composed of two diffraction patterns rotated by 90° with respect to the orthorhombic phase as twin structures, as shown in Fig. 2. The pattern revealed that the a^*-axis was not equivalent to the b^*-axis. The transition temperature was in agreement with DSC and electrical conductivity data shown in Table 2. The symmetry of the orthorhombic phase at relatively high temperatures has not yet been determined. We suggest that the phase transition around 623 K is a first-order phase transition because extra large peak was observed in the DSC curve [10] and the orthorhombic symmtry (Fig. 2) was not in the symmetrical subgroup of $P4_2/mnm$. A similar phase transition was observed in $BaEu_2Mn_2O_7$ [5]. This phase transition might be related to the behavior of the 3d electrons in the Mn^{3+} ion. The change was detected in the magnetic property data in which slight changes were observed at 600 and 670 K, as reported in a previous paper [14]. At higher temperatures, the structure might stabilize by uniting the lattice vibration and the electronic structure, in the form of vibronic coupling [15].

We think that other rare earth manganites with double-block oxygen layer have the possibility of happening by a fiirst-order phase transition. These structures should be further analyzed in terms of their physical properties in order to elucidate the behavior of the phase transition in layered manganites.

4 Conclusion

The layered manganites $BaLn_2Mn_2O_7$ (Ln = rare earth) take on many different structures depending on the synthetic or annealing conditions for the rare earth element. These manganites exhibited a heat-induced phase transition from orthorhombic to tetragonal, as determined by XRD, DSC and electrical conductivity. The relationship between transition temperature and rare earth species was summarized:

the transition temperature decreased with increasing rare earth ionic radius. At relatively high temperatures, a first-order phase transition was observed in Gd manganites by thermal TEM. This first-order phase transition was related to the behavior of 3d electrons in Mn^{3+}. The low symmetry structure at high temperature might stabilize by uniting the lattice vibration and the electronic structure.

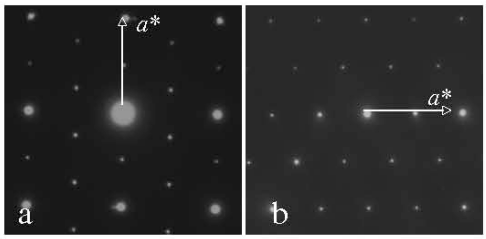

Fig. 2 Fig. 1(e) is composed of the two patterns shown in (a) and (b). The SAD pattern is taken from the orthorhombic phase at above 723 K.

References

[1] N. Kamegashira, H. Nakano, G. Chen, and J. Meng, J. Rare Earths **22**(5), 582 (2004).
[2] N. Kamegashira, J. Meng, T. Murata, K. Fujita, H. Satoh, T. Shishido, and T. Fukuda, in: Proceedings of 10th Int. Ceramics Congress, CIMTEC (2002), edited by P. Vincenzini, Part A, p. 181.
[3] N. Kamegashira , J. Meng, T. Mori, A. Murase, K. Fujita, H. Satoh, T. Shishido, and T. Fukuda, Mater. Lett. **57**, 1941 (2003)
[4] N. Kamegashira, Shokubai **31**(4), 222 (1989) (in Japanese).
[5] H. Nakano, N. Ishizawa, and N. Kamegashira, Proceedings of PACRIM6, Maui (2005), in press.
[6] N. Kamegashira, H. Satoh, and M. Horikawa, Mater. Lett. **10**(11,12), 494 (1991).
[7] J. Meng, H. Satoh, M. Ishida, and N. Kamegashira, J. Alloys Compd., in press (2006).
[8] N. Kamegashira and S. Umeno, J. Rare Earths (Special Issue) **1**, 242 (1991).
[9] N. Kamegashira and M. Ichikawa, Mater. Chem. Phys. **25**, 71 (1990).
[10] J. Meng, N. Kmegahira, A. Murase, H. Satoh. H. Y. Wang, Q. B. Bo, and C. Peng, Int. J. Mater. Product Technol. **1**, 397 (2000).
[11] N. Kamegashira, S. Umeno, H. Satoh, and M. Horikawa, Mater. Chem. Phys. **24**, 83 (1989).
[12] K. S. Aleksandrov and J. Bartolome, J. Phys.: Condens. Matter **6**, 8219 (1994).
[13] R. D. Shannon, Acta Cryst. A **32**, 751 (1976)
[14] A. Shimono, K. Hayashi, and N. Kamegashira, Mater. Chem. Phys. **28**, 175 (1991).
[15] J. B. Goodenough, J.-S. Zhou, F. Rivadulla, and E. Winkler, J. Solid State Chem. **175**, 116 (2003).

JOURNAL OF RARE EARTHS
Vol. 24, Spec. Issue, Dec. 2006, p. 1

Novel Phase Transition in $BaPr_2Mn_2O_7$

Hiromi Nakano[1]*, Naoki Kamegashira[2]
(*1. Ryukoku University, Seta, Otsu 520-2194, Japan; 2. Toyohashi University of Technology, Tenpaku-cho, Toyohashi 441-8580, Japan*)

Abstract: The rare earth manganite $BaLn_2Mn_2O_7$(Ln = rare earth element) has a $Sr_3Ti_2O_7$-type layered perovskite structure with double-block oxygen octahedra belonging to the Ruddlesden-Popper-type homologous series $AO(ABO_3)_2$. In Pr-manganite, a novel phase transition was first observed in situ at 1040 K by a thermal transmission electron microscope. At 1040 K, reflections began to split along the *c*-direction in the selected area diffraction pattern. This indicates that a new phase appears in the original phase matrix; the *c* length of the new phase is 1.5% longer than that of the original phase. After about 5 min, the original phase disappears. No change in the crystal symmetry (space group *I4/mmm*) is observed above 1040 K.

Key words: rare earth manganite; phase transition; transmission electron microscope (TEM)
CLC number: TG145 **Document code**: A **Article ID**: 1002 - 0721(2006) - 0001 - 03

Layered perovskite manganites $BaLn_2Mn_2O_7$(Ln = rare earth) with a double block of oxygen octahedra were first synthesized by Deshizeaux-Cheruy and Joubert for Ln = Pr-Gd[1] and by Kamegashira (one of the present authors) for Ln = Tb[2]. After that, many phases have been synthesized and identified, whose appearance depended on the synthesis conditions[3]. In recent years, the authors have found heat-induced phase transitions, where the orthorhombic phase for Ln = Sm, Eu, Gd, Nd and Tb transformed into the tetragonal phase by high-temperature X-ray diffraction (XRD), thermal analysis, and electrical conductivity[4-6]. The transition temperatures tend to increase with decreasing ionic radius of the rare earth ion. In Pr-manganite, however, no phase transition has yet been found, and the synthesized phase was only a prototype structure with the space group *I4/mmm*.

In the present experiment, the structural change in $BaPr_2Mn_2O_7$ was observed in-situ by using a transmission electron microscope (TEM) with a thermal holder. A novel phase transition of Pr-manganite upon heating was found and the phase behavior of the rare earth manganites with layered perovskite was discussed.

1 Experimental

$BaLn_2Mn_2O_7$(Ln = rare earth) was prepared from starting materials $BaCO_3$, Ln_2O_3, and Mn_2O_3 by a ceramics method in Ar atmosphere. The ceramic was grown by the floating zone (FZ) method in Ar atmosphere, whereby a single crystal was obtained. The detailed procedure was described in our previous paper[7].

The synthesized phase was analyzed by an X-ray four-circle diffractometer (Rigaku-AFC7R Tokyo, Japan).

The specimen was crushed and scooped onto a copper mesh with carbon-coated microgrids and subjected to high-resolution TEM observations. The TEM (JEM-3000F, JEOL, Tokyo, Japan) was operated at 300 kV with spherical aberration $C_s = 1.0$ nm.

In-situ observations were performed using a thermal stage in the range from room temperature to 1073 K in the TEM (JEM-2000EX, EM-SHU2 specimen holder, JEOL). The temperature was controlled manually and the heating rate was about 600 $K \cdot h^{-1}$.

2 Results and Discussion

Table 1 shows the structure of as-grown crystals of $BaPr_2Mn_2O_7$ refined by an X-ray four-circle diffractometer and structure determination program (SHELX-97). The structure has tetragonal symmetry with the space group *I4/mmm*, which is a prototype layered perovskite structure with double-block oxygen octahedra. The layered structure along the *c*-direction was observed by a high-resolution TEM. A repeat distance of 1.03 nm was observed along the *c* - direction, and

Received date: 2006 - 06 - 24; **revised date**: 2006 - 09 - 10
Foundation item: Project supported by a Grant-in Aid for Scientific Research (c) No. 18560662 by Japan Society for the Promotion of Science
Biography: Hiromi Nakano, Female, Senior teaching associate; Research field: Characterization of ceramics by electron microscopy
* **Corresponding author** (E-mail: hiromi@rins.ryukoku.ac.jp)

Table 1 Atomic parameters of $BaPr_2Mn_2O_7$

Parameters	x	y	z
Ba	0	0	0.5
Pr	0	0	0.31689(2)
Mn	0	0	0.09917(9)
O1	0	0	0
O2	0	0	0.2063(8)
O3	0	0.5	0.1060(3)

Space group $I4/mmm$, $a = b = 0.3905$ (1) nm; $c = 2.0626$ (1) nm, $R = 0.0759$, $S = 1.26$

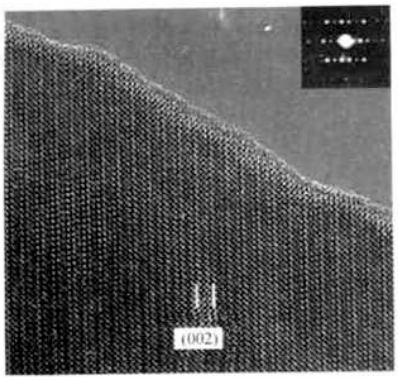

Fig. 1 High-resolution TEM image of $BaPr_2Mn_2O_7$ taken from [100] zone axis

corresponded to the (002) spacing, as shown in Fig. 1. The inset is a selected area diffraction (SAD) pattern taken from the [100] zone axis. Fig. 1 shows no stacking disorder or streaks between the reflections. We observed in situ the structural change in $BaPr_2Mn_2O_7$. The present authors have previously succeeded in observing multiple phase transitions for Ln = Eu and Gd by high-temperature TEM. The TEM data revealed an intermediate phase and the changes in real time using a video system.

Figs. 2(a) and (b) show SAD patterns taken from the [001] zone axis at room temperature and 1073 K, respectively. No change was observed in Fig. 2. However, an obvious change was observed in the SAD patterns taken from the [100] zone axis.

Fig. 3 shows the changes in the SAD patterns upon heating of the specimen holder of the TEM. At around 1040 K, the reflections began to split into two along the c-direction, as indicated by two arrows in Fig. 3(b). The split was caused by the presence of two phases (low-temperature phase and high-temperature phase). It indicated that the unit cell size of the high-temperature phase along the c-direction was larger than that of the low-temperature phase. The expansion length remained constant despite the increase in temperature. After about 5 min, the former reflections vanished. The unit cell size of the high-temperature

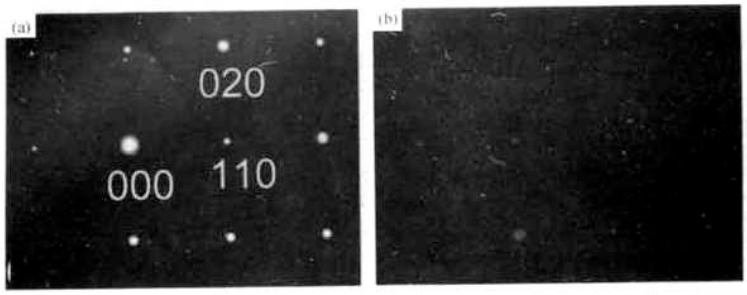

Fig. 2 SAD patterns of $BaPr_2Mn_2O_7$ taken from [001] zone axis at ambient temperature (a) and 1073 K (b)

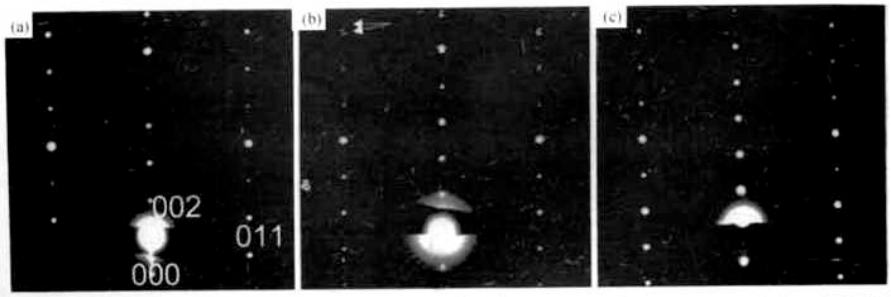

Fig. 3 Structural change in SAD pattern of $BaPr_2Mn_2O_7$ taken from [100] zone axis at ambient temperature (a), at 1040 K (b), and after about 5 min at 1040 K (c)

phase expanded by about 1.5% along the c-axis in comparison to the low-temperature phase. No change was observed in the structural symmetry. Such phase transition could not be detected easily by high-temperature XRD because two phases were coexisted for only 5 min. Therefore, XRD data showed the expansion of the cell size but no change of the crystal symmetry at high temperature[3].

The structural change was a first-order phase transition, as seen in Eu- and Gd-mangaganites[6]. In the case of Eu- and Gd-manganite, the structural symmetry changed at relatively high temperature, and the cell size expanded by about 1.5% along the c-direction[6]. We think the reason for the expansion of the cell size at high temperature in these layered manganites as follows. $BaPr_2Mn_2O_7$ possess a double-block oxygen octahedra in which Mn-O lengths shows various sizes, Mn-O_2(0.22097 nm) > Mn-O_1(0.2045 nm) > Mn-O_3(0.19576 nm), as calculated in Table 1. The difference in the length between Mn-O_3 and Mn-O_2 was caused by the Jahn-Teller effect for tri-valent of Mn ion[8]. However, Mn-O_1 length was shorter by 0.016 nm than that of Mn-O_2 and the short length might be caused by the structure of double-block oxygen octahedron. When the length strain was lost above 1040 K, and accordingly the cell size expanded about 1.5% (0.032 nm) along the c-axis. We believe that the first-order phase transition was caused by the crystal nature of the layered manganite $BaLn_2Mn_2O_7$ with double-block oxygen octahedra.

3 Conclusion

A novel phase transition in $BaPr_2Mn_2O_7$ was observed by a high-temperature TEM. The phase at ambient temperature has a prototype structure with tetragonal symmetry (space group $I4/mmm$). A structural change was clearly visible in the SAD pattern at around 1040 K. Along the c-direction, reflections began to split, and after 5 min, the former reflections vanished. As a result, the cell size expanded by about 1.5% along the c-direction. No change was observed in the structural symmetry. The structural change was a first-order phase transition.

References:

[1] Deshizeaux M, Cheruy N, Joubert J C. Donnees cristallographiqes sur une nouvelle serie de manganites mixtes de terre rare et d'alcalino-terreux [J]. J. Solid State Chem., 1981, 40: 14.

[2] Meng J, Satoh H, Kamegashira N. Crystal structure refinement of tetragonal $BaTb_2Mn_2O_7$ [J]. J. Alloys and Compounds, 1996, 244: 75.

[3] Kamegashira N, Nakano H, Chan G, et al. Phase behavior of rare earth manganites [J]. J. Rare Earths, 2004, 22(5): 582.

[4] Kamegashira N, Meng J, Mikami T, et al. Phase behavior of $BaLn_2Mn_2O_7$(Ln = rare earth) with a layered perovskite structure [J]. J. Rare Earths, 2004, 22(1): 17.

[5] Kamegashira N. Phase transition of rare earth manganites [J]. Shokubai, 1989, 31(4): 222.

[6] Nakano H, Kamegashira N, Ishizawa N. In-situ observation of structural transition in rare earth manganites by TEM [A]. Proceedings of PacRim 6 [C]. Maui, U.S.A, (2005) in press.

[7] Kamgegashira N, Meng J, Mori T, et al. Growth and structure analysis of single crystal of tetragonal $BaGd_2Mn_2O_7$ with a superlattice structure [J]. Material Letters, 2003, 57: 1941.

[8] Goodenough J B, Zhou J S, Rivadulla F, et al. Bond-length fluctuations in transition-metal oxyperovskite [J]. J. Solid State Chem., 2003, 175: 116.

ペロブスカイト関連酸化物の相状態その場観察に関する研究成果

journal

J. Am. Ceram. Soc., 89 [4] 1461–1464 (2006)
DOI: 10.1111/j.1551-2916.2005.00908.x

Thermal Behavior of $BaTiO_3$ Particles Synthesized by Plasma Chemical Vapor Deposition

Hiromi Nakano†

Electron Microscope Laboratory, Faculty and Technology, Ryukoku University, Ryukoku, Japan

Keigo Suzuki and Kazunori Kizima

Graduate School of Materials Science and Technology, Kyoto Institute of Technology, Kyoto, Japan

The thermal behavior of nanoparticles $BaTiO_3$, prepared by a radio-frequency plasma chemical vapor deposition (RF-plasma CVD) method, was characterized by various analysis methods. The $BaCO_3$ phase was included in the powder as byproducts, which is also observed in hydrothermal $BaTiO_3$ powder. The $BaCO_3$ phase decomposed and disappeared by annealing at 873 K for 30 min. H_2O, N_2, CO_2 and H_2, were detected by a thermal desorption spectra measurement from $BaTiO_3$ powder. The annealed powder became well-crystallized particles without grain growth, although as-prepared powder included polycrystalline particles. We successfully observed in-situ grain growth for $BaTiO_3$ nanoparticles by thermal transmission electron microscope. At the initial step of normal grain growth, very fine particles with 40–60 nm diameters started to merge into the larger grains around 1083 K. The migration rate was measured by video images and a grain boundary diffusion coefficient D_{gb} was calculated.

I. Introduction

FINE-GRAIN and well-crystallized $BaTiO_3$ particles are required in the electronic industry. In recent years, $BaTiO_3$ nanoparticles have been synthesized by various production methods, such as solid-state reaction,[1] hydrothermal synthesis,[2–4] alkoxide method,[5,6] sol–gel method,[7,8] and so on. Hydrothermal synthesis or an alkoxide method based on a liquid phase process supplies very fine powder, compared with the powder synthesized by the solid phase reaction, which is known as the conventional method. Therefore, hydrothermally prepared powder has been mass-produced and is commercially available.[9] The characteristic phenomenon in hydrothermal $BaTiO_3$ powder has been investigated by transmission electron microscope (TEM), in our previous papers.[10,11] The hydrothermal $BaTiO_3$ powder includes OH^- ions or H_2O in the $BaTiO_3$ lattice.[12] Accordingly, the volume of the unit cell is larger than that of the $BaTiO_3$ prepared by the solid-state reaction. Additionally, defects in the particles directly affect the density of the unit cell.[11,13] A $BaCO_3$ phase, which is easily formed on the surfaces of hydrothermal $BaTiO_3$, is decomposed by annealing at >1073 K, and the phase reappears when annealed powder is exposed to air or humid atmosphere for a few weeks.[13] Such behaviors depend on the synthesizing processes of $BaTiO_3$ powder.

H. Chan—contributing editor

Manuscript No. 20793. Received July 21, 2005; approved November 19, 2005.
†Author to whom correspondence should be addressed. e-mail: hiromi@rins.ryukoku.ac.jp

In recent years, Suzuki and Kizima[14] successfully synthesized fine particle $BaTiO_3$ by a radio-frequency chemical vapor deposition (RF-plasma CVD) method. $BaTiO_3$ films prepared by CVD have been reported by some authors,[15,16] while $BaTiO_3$ nanoparticles synthesized by plasma CVD have been seldom been characterized yet.

In the present study, we focused on the thermal properties and behavior of $BaTiO_3$ particles prepared by plasma CVD. The characterization was performed using X-ray diffraction (XRD), thermal desorption spectra (TDS) measurement, and thermogravimetric analysis (TG). We will discuss the thermal properties in comparison with hydrothermal $BaTiO_3$. Still more, thermal behavior was observed *in situ* on the thermal stage in a TEM device. At the initial stage of grain growth, grain-boundary diffusion coefficient D_{gb} was calculated from a migration rate of grain boundaries.

II. Experimental Procedure

$BaTiO_3$ nanoparticles were synthesized by RF-plasma CVD method. Titanium iso-propoxide ($Ti[OCH(CH_3)_2]_4$, Nakarai Tesque Inc., Tokyo, Japan) and bis-dipivaloylmethanate barium ($Ba(C_{11}H_{19}O_2)_2$, Kojundo Chemical Lab Co., Tokyo, Japan) were used as starting materials. The detailed procedure was reported previously.[14]

Crystal structures of the products were measured by XRD (RINT-2000, RIGAKU, Cu$K\alpha$, Tokyo, Japan). Thermal behavior of the products was evaluated using TG (TP-1, RIGAKU) and TDS (HPT–TDS, RIGAKU).

The nanoparticles were scooped onto a mesh and subjected to high-resolution TEM observation (JEM-3000F, JEOL, Tokyo, Japan). TEM equipped with an energy-dispersive X-ray spectroscopy (EDS) apparatus was used to characterize the composition of the products. *In situ* observation of thermal behavior was performed by TEM (JEM-2000EX, EM-SHH4 specimen holder, JEOL) using a thermal stage in a range from room temperature to 1083 K. The temperature of the specimen was manually controlled on the specimen holder.

III. Results and Discussion

(1) Characterization of $BaTiO_3$ Particles Synthesized by Plasma CVD Method

As mentioned above, the $BaCO_3$ phase is included in $BaTiO_3$ particles as byproducts under some conditions. For example, $BaCO_3$ phase is formed on the particle surface of the hydrothermally synthesized $BaTiO_3$ particles under the following chemical reaction: $BaTiO_3+x(H_2O+CO_2)=(Ba_{1-x}H_{2x})TiO_3+xBaCO_3$.[10] Thus, it is important to investigate the thermal decomposition behavior of $BaCO_3$ included in $BaTiO_3$ powder. From this point of view, we selected as-prepared powder that involves some amounts of $BaCO_3$ phase for the present study,

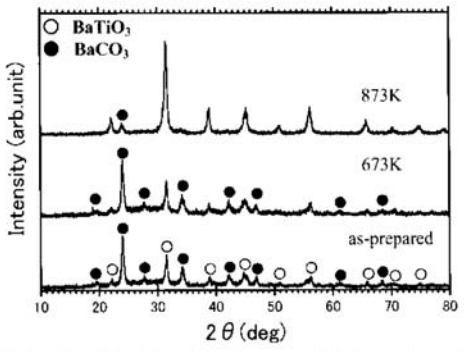

Fig. 1. X-ray diffraction profiles of as-prepared $BaTiO_3$ powder, and powder annealed at 673 and 873 K for 30 min.

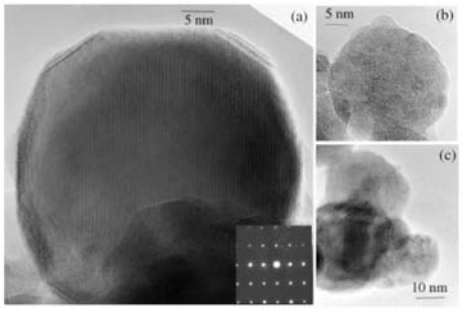

Fig. 3. Transmission electron microscope images of various types of $BaTiO_3$ nanoparticles prepared by RF-plasma chemical vapor deposition method. Inset attached in (a) shows a corresponding selected area diffraction pattern taken from [110] axis.

although we have already succeeded in preparing single phase of perovskite $BaTiO_3$ nanoparticles.[14,17]

Figure 1 shows the XRD patterns of the as-prepared powder and the powders annealed at the temperatures of 673 and 873 K for 30 min. The as-prepared powder fairly included $BaCO_3$ phase as byproducts. The formation mechanism of $BaCO_3$ phase in the plasma CVD process was described in our previous papers.[17] The $BaCO_3$ phase was easily decomposed and disappeared by annealing at 873 K for 30 min. Moreover, the XRD profiles revealed that the degree of crystallinity effectively increased by annealing at 873 K.

The gas-desorption behavior and weight loss of the $BaTiO_3$ powder were characterized by TDS and TG measurements, respectively, in a heat range from room temperature to 1273 K. Figure 2 shows TG curve accompanied with TDS spectra. The gaseous species CO_2 was observed at temperature range from 700 to 1100 K. It might be decomposed from the $BaCO_3$ phase.[10] The gaseous species H_2 was detected around 1173 K, which might be combined with O ions in the $BaTiO_3$ lattice. Below 600 K, the gaseous species H_2O on the surface of the $BaTiO_3$ particles were mainly detected. However, in the case of hydrothermally synthesized $BaTiO_3$, the gaseous species H_2O was detected in a wider temperature range up to 1073 K, which is attributed to H_2O or OH ions included inside the particles.[3,12] The weight loss of approximately 15% is mainly caused by the escape of H_2O gas and the decomposition of $BaCO_3$. These findings corresponded to hydrothermal $BaTiO_3$ powder.[3] The characteristic peak was a N_2 gas spectrum detected around 900 K for the plasma CVD powder. Gaseous species N_2 may originate in the decomposition of an amorphous nitrogen compounds. The mechanism of formation of the amorphous nitrogen compounds was reported by Suzuki and Kijima.[17]

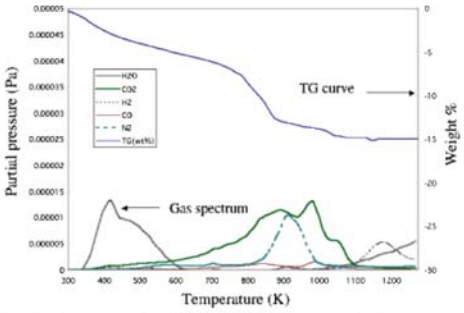

Fig. 2. Thermo-gravimetric analysis (TG) curve and thermal desorption spectra of the $BaTiO_3$ powder in the temperature range from room temperature to 1273 K.

Figure 3 shows TEM images of $BaTiO_3$ particles synthesized by the plasma CVD method. Particle sizes ranged from 10 to 50 nm in diameter by TEM image. A well-crystallized particle was seen in Fig. 3(a), and the inset shows a selected area diffraction (SAD) pattern taken from the [110] zone axis. No pore was observed in the particles, although internal pores were usually observed in hydrothermally synthesized $BaTiO_3$ particles.[11] Facet was formed on the (111) plane. Polycrystalline particles were also observed, as shown in Figs. 3(b) and 3(c). In Fig. 3(b), it seemed that the particle contains several small crystallites. Each particle showed nearly stoichiometric composition according to the EDS measurement. Formation of several types of $BaTiO_3$ nanoparticles may be due to the difference of the quenching rates of chemical species in the plasma CVD process.[18]

(2) In Situ Observation of Thermal Behavior of $BaTiO_3$ Particles in TEM

We tried in situ observations of the thermal behavior of the $BaTiO_3$ particles in a TEM device using a thermal holder. In this experimental stage, we could record the grain-boundary mobility at the initial stage of normal grain growth at 1083 K. The temperature of the holder was increased from room temperature at the heating rate of about 9 K/min, and maintained at 1083 K for 20 min. Figure 4 shows the changes in the $BaTiO_3$ particles by heating from room temperature to 1083 K. The changes in images are shown in Figs. 4(a)–(c). The consecutive images are recorded by video film and a part of the fragmentary images are shown in Figs. 4(d)–4(f). Remarkable grain growth did not occur below 873 K. However, SAD patterns shown in the insets revealed that the degree of the crystallinity increased with an increase in temperature up to 873 K. Around 1083 K, grain growth started, and small particles with 40–60 nm diameters merged into large particles. This phenomenon is an initial stage of normal grain growth, which means that grain boundaries moved as a consequence of many individual atomic jumps across the plane of the boundary.[19] The grain-boundary diffusion coefficient (D_{gb}) is calculated by applying the migration rate across the grain boundary (v, m/s) to the following equations[20]:

$$v = D_{gb}\Delta F/(\lambda RT) = 2D_{gb}\gamma V/(\lambda RTr) \quad (1)$$

$$\Delta F = 2\gamma V/r \quad (2)$$

Here, ΔF is total free energy (J/mol) on the boundary, R is a gas constant, T is the temperature, and λ is the boundary thickness. V is molecular volume. γ is boundary energy (J/m^2)

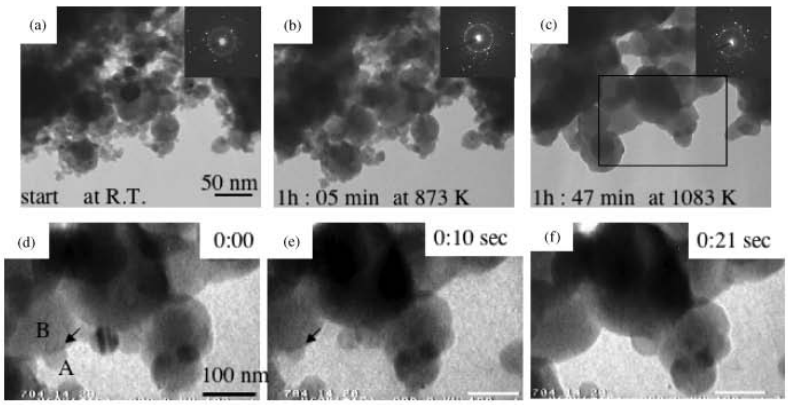

Fig. 4. Changes in $BaTiO_3$ particles on thermal holder in transmission electron microscope (TEM). TEM images and selected area diffraction patterns obtained at (a) room temperature, (b) 873 K, and (c) 1083 K. (d)–(f) show the series of images where "A" grain merged with "B" grain at 1083 K.

that was estimated at roughly 1 J/m^2. In our experiment, the migration rate (v) and curvature ($2/r$) was determined from the movement of some particles by the series of the thermal TEM images recorded by video system. Table I show curvature ($2/r$), migration rate (v), and calculated grain boundary diffusion coefficient (D_{gb}). These values were derived from the movement of $BaTiO_3$ nanoparticles with 40 60 nm diameters at 1083 K. The grain No. 6 in Table I was determined from those images in Figs. 4(d) (f). Kusunoki *et al.*[20] determined the D_{gb} of ZrO_2 with about 30 nm diameters at 1473 K from thermal TEM images by the similar method. These values of D_{gb} in Table I were almost comparable with that of ZrO_2 (1.4×10^{-17} m^2/s).

IV. Conclusions

We successfully synthesized $BaTiO_3$ nanoparticles by the RF-plasma CVD method. The thermal properties of the nanoparticles were characterized by XRD, TG, TDS measurements, and TEM observation. *In situ* observation of thermal behavior was recorded using thermal TEM. Those data revealed the following results:

1. The $BaCO_3$ phase included in $BaTiO_3$ powder decomposed and disappeared by annealing at 873 K for 30 min. The degree of crystallinity increased without grain growth by annealing at 873 K. Thus, the annealed powder derived from the plasma CVD is expected to be commercial available.

Table I. Curvature ($2/r$), Migration Rate (v), and Calculated Grain-Boundary Diffusion Coefficient (D_{gb}) of $BaTiO_3$ at 1083 K

Grain	Curvature ($2/r$) $\times 10^7$ m	Migration rate (v) $\times 10^{9}$ m/s	Grain-boundary diffusion coefficient (D_{gb}) $\times 10^{-18}$ m^2/s
1	5.0	2.5	3.25
2	4.8	3.7	4.93
3	3.2	2.7	5.36
4	4.0	2.5	4.07
5	4.3	2.9	4.43
6	3.6	2.4	4.29
Average			4.39 (Standard deviation $\sigma = 0.66$)

2. Various gases such as H_2O, N_2, CO_2, and H_2 were detected from $BaTiO_3$ powder by the TDS measurements from room temperature to 1273 K.

3. TEM observation showed that particle sizes ranged from 10 to 50 nm in diameter. Well-crystallized $BaTiO_3$ particles were observed, but polycrystalline particles coexisted in the powder products. No pores were observed in the plasma CVD-derived $BaTiO_3$ powder in contrast with hydrothermally synthesized $BaTiO_3$.

4. *In situ* TEM observation showed that grain growth started around 1083 K. At the initial step of normal grain growth, the migration rate was from the movement of the particles with 40 60 nm sizes recorded by video system. As a result, average value of grain-boundary diffusion coefficient (D_{gb}) at 1083 K was calculated to be 4.39×10^{-18} m^2/s with standard deviation of 0.66×10^{-18} m^2/s. This value was almost comparable with that of ZrO_2 nanoparticles at 1473 K. From the results, we expect that the dense products will be sintered using the present $BaTiO_3$ powder by relatively low energy compared with hydrothermal $BaTiO_3$ powder.

References

[1]E. Brrorowskie and M. S. Castro, "Synthesis of Barium Titanate Improved by Modifications in the Kinetics of the Solid State Reaction," *J. Euro. Ceram. Soc.*, **20** [14-15] 2347 51 (2000).
[2]K. W. Seo and J. K. Oh, "$BaTiO_3$ Particle Formation Mechanism Under Hydrothermal Conditions," *J. Ceram. Soc. Jpn.*, **108** [8] 691 6 (2000).
[3]T. Kunieda and S. Moriyama, "Properties of Hydrothermal Barium Titanate Powders," *Creative*, **5**, 67 77 (2004) [in Japanese].
[4]D. Hennings and S. Schreinemacher, "Characterization of Hydrothermal Barium Titanate," *J. Euro. Ceram. Soc.*, **9**, 41 46 (1992).
[5]Y. Suyama and M. Nagasawa, "Synthesis of Single-Crystal Barium Titaium Isopropoxide Complex to Form Barium Titanate," *J. Am. Ceram. Soc.*, **77** [2] 603 5 (1994).
[6]Y. Suyama, T. Noritake, and M. Nagasawa, "Formation of $BaTiO_3$ from a Barium Titanium Isoproxide Complex," *Jpn. J. Appl. Phys.*, **36**, 5939 42 (1997).
[7]R. N. Viswanath and S. Ramasamy, "Preparation and Ferroelectric Phase Transition Studies of Nanocrystalline BaTiO," *Nanostruct. Mater.*, **8** [2] 155 62 (1997).
[8]H. F. Guo, X. T. Zhang, B. Liu, Y. C. Li, Y. B. Huang, and Z. L. Du, "Preparation of Nanometer-sized $BaTiO_3$ Crystallites by Sol Gel Method and Size Effects on Structure," *Acta Phys-Chim Sinica*, **20** [2] 164 8 (2004).
[9]K. Fukui, K. Hidaka, M. Aoki, and K. Abe, "Preparation and Properties of Uniform Fine Perovskite Powders by Hydrothermal Synthesis," *Ceram. Int.*, **16** [5] 285 90 (1990).
[10]H. Nakano, K. Urabe, and H. Ikawa, "Barium Carbonate Phase on the Surfaces of Barium Titanate Particle and *in situ* Transmission Electron Microscopy Observation of its Decomposition," *J. Am. Ceram. Soc.*, **86** [4] 741 3 (2003).

[11]H. Nakano, K. Urabe, T. Oikawa, and H. Ikawa, "Characterization of Internal Pores in Hydrothermally Synthesized $BaTiO_3$ Particles by Transmission Electron Microscopy," *J. Am. Ceram. Soc.*, **87** [8] 1594 7 (2003).
[12]Y. Sakabe, N. Wada, J. Ikeda, and Y. Hamaji, "Ceramics for Ultra-Thin Dielectric Layer of Multilayer Ceramic Capacitors"; pp 565 569 in *Proceedings of ISAF 11th IEEE*, Edited by E. Colla. IEEE, Piscataway, NJ, 1998.
[13]H. Ikawa, N. Munekata, T. Ozeki, M. Takemoto, and T. Shirakami, "Ferroelectric Phase Transformation and Density of Heated Hydrotheram Barium Titanate," *Trans. Mater. Res. Soc. Jpn.*, **27** [4] 707 10 (2002).
[14]K. Suzuki and K. Kizima, "Synthesis and Characterization of Barium Titanate Nanoparticles by Plasma Chemical Vapor Deposition," *J. Ceram. Soc. Jpn*, **12** [5] S916 23 (2004).
[15]J. Zeng, H. Wang, M. Wang, S. Shang, Z. Wang, and C. Lin, "Preparation and Ferroelectric Properties of $BaTiO_3$ Thin Films by Atmospheric-Pressure Metalorganic Chemical Vapor Deposition," *Thin Solid Films*, **322**, 104 7 (1998).
[16]Y. S. Yoon, S. S. Yom, T. W. Kim, and S. J. Lee, "Surface, Structural and Electrical Properties of $BaTiO_3$ Films Grown on p-Si Substrates by Low Pressure Metal Organic Chemical Vapor Deposition," *J. Mater. Sci.*, **30**, 3603 6 (1995).
[17]K. Suzuki and K. Kijima, "Effect of Oxygen Injection on Synthesizing Barium Titanate Nanoparticles by Plasma Chemical Vapor Deposition," *J. Mater. Sci.*, in press.
[18]M. Sugasawa, N. Kikukawa, N. Ishikawa, N. Kayano, and T. Kimura, "Synthesis of Y Fe O Ultrafine Particles Using Inductively Coupled Plasma," *J. Aerosol Sci.*, **29** [5] 675 86 (1998).
[19]W. D. Kingery, *Introduction to Ceramics*, 2nd edition, pp. 448 515. John Wiley & Sons Inc., New York, 1976.
[20]M. Kusumoki, K. Yonemitsu, Y. Sasaki, Y. Ikuhara, and Y. Kubo, "Estimation of Diffusion Coefficients for Zirconia," *Ceram. Trans.*, **44**, 455 64 (1994). □

「材料」(Journal of the Society of Materials Science, Japan), Vol. 56, No. 6, pp. 500-504, June 2007
論　文

Sol-Crystal 法により合成したナノポーラス $NaNbO_3$ 粒子の微構造†

中野裕美* 平野陽介** 陶山容子**

Microstructure of Nano-Porous $NaNbO_3$ Particles Synthesized by Sol-Crystal Method

by

Hiromi NAKANO*, Yosuke HIRANO** and Yoko SUYAMA**

Nano-porous $NaNbO_3$ was successfully synthesized from Na-Nb ethoxide by sol-crystal method. Structural characterization of specimens annealed at various temperatures was performed by a transmission electron microscope (TEM) and X-ray diffractometery. The single crystal of Na-Nb ethoxid was decomposed to an amorphous matrix below 473K. Small crystals were grown by heating above 573K, and the crystal sizes became larger with increasing temperature. At 673K, well crystallized $NaNbO_3$ grain with an orthorhombic structure (S.G. *Pbcm*) was observed. The three-dimensional image constructed by a tomography system showed that the grain had many inner-pores with a few ten nano-meter sizes. Thermal behavior of the inner-pore could be observed *in-situ* with a TEM using a heating stage during the crystallization process.

Key words : Nano-porous grain, Transmission electron microscope, Sodium naiobate, Sol-crystal method

1 緒　　言

近年，環境に配慮した鉛を含まない誘電体材料として，$NaNbO_3$ やその固溶体に関する研究が行われてきた．純粋な $NaNbO_3$ は，室温では反強誘電性[1]が知られているが，$LiNbO_3$,[2)~3)] $KNbO_3$,[4)] $BaTiO_3$[5)] やその他のペロブスカイト関連酸化物[6)] などとの置換により強誘電性になることが多くの研究者により報告されてきた．また，スパークプラズマ法により合成された $NaNbO_3$ セラミックス[7)] では，強誘電性や圧電性が報告されているなど興味ある物性が期待されている．このような $NaNbO_3$ を高品質の電子材料として利用するためには，均質で高品質の微粒子が求められる．

近年，陶山らは $BaTiO_3$,[8)~9)] $Ba_5Nb_4O_{15}$[10)] の合成において，通常のセラミックス合成温度よりも低温で均質な微粒子の合成を sol-crystal 法により成功した．この手法は，複合アルコキシドを前駆体として組成を制御し，単結晶を経て熱処理により結晶化する方法で，均質な酸化物の微粒子が得られるという特徴がある．本研究では，Na-Nb 複合エトキシド結晶から $NaNbO_3$ の合成を行ったところ，ナノサイズの気孔を有するポーラスな粒子が形成されることを見出したので，各熱処理温度で得られた試料を詳しく解析し，結晶化過程や微構造の変化等を報告する．

2 実　　験

ベンゼン溶媒に所定量の $NbCl_5$ と EtOH を加え，不活性ガス雰囲気中で撹拌し，その溶液に NH_3 ガスを流すことにより $Nb(OEt)_5$ を合成した．この $Nb(OEt)_5$ に所定量の Na と EtOH を加えて室温で撹拌溶解させた．このようにして調製した溶液から Na-Nb 複合エトキシド結晶を析出させた．この結晶を不活性ガス雰囲気中で 373K で 1 時間乾燥させた後，373K ～ 973K の各温度でそれぞれ 1.5 時間加熱処理した．熱重量－示差熱分析 (TG-DTA Rigaku ThermoPlus TG8120) により複合エトキシドから複合酸化物への熱分解挙動を調べた．得られた生成物は，粉末 X 線回折法 (XRD, Rigaku RINT-2000, CuKα) により相の同定を行った．また微構造は走査型電子顕微鏡 (SEM, JSM 5410) および高分解能透過型電子顕微鏡 (HR-TEM, JEM-3000F) により観察した．非晶質相から結晶相への熱挙動のその場観察は高温 TEM (JEM-2000EX, EM-SHH4) を用い，気孔の熱挙動を撮影した．873K で得られたナノポーラス粒子の形状は，TEM (JEM-2100) により試料傾斜角度 +60 度から −60 度において像を撮影し，トモグラフィシステム (EM-05500TGP) により三次元像を構築した．

3 結 果 と 考 察

3・1 Na-Nb エトキシドの様々な温度(373K ～ 973K) による熱処理後の微構造

Fig. 1 に，Na-Nb エトキシドを 373K から 973K の各温度で 1.5 時間熱処理をして得られた試料の XRD パターンを示す．Na-Nb 複合エトキシドは，473K 以下でほとんど分解し，$NaNbO_3$ の組成を有する非晶質相が生成すると考えられる．623K では，わずかに $NaNbO_3$ 結晶相の回折ピークが確認できる．673K 以上で斜方晶 $NaNbO_3$ (空間群 *Pbcm* (No. 57)) で指数づけされる明瞭な回折ピークが確認された．673K での格子定数は，$a = 0.5561$nm，$b = 0.5523$nm，$c = 1.560$nm で結晶子は 57nm と計算され

† 原稿受理 平成 18 年 7 月 26 日 Received July 26, 2006
* 正会員 龍谷大学理工学部電子顕微鏡室 〒520-2194 大津市瀬田大江町横谷，Electron Microscope Laboratory, Ryukoku Univ., Seta, Otsu, 520-2194
** 島根大学総合理工学研究科 〒690-8504 松江市西川津町，Division for Res. Sci. and Eng., Shimane Univ., Nishikawatsu-cho, Matsue, 690-8504

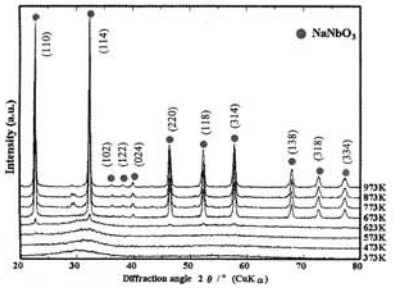

Fig. 1　XRD patterns of specimens annealed at various temperatures for 1.5h.

た．目立ったピークに回折指数をつけたが，小さいピークについてもすべて $NaNbO_3$ の斜方晶にもとづくピークであることを確認した．

Fig. 2 に，TG-DTA 曲線を示す．TG 曲線で 473K までに現れた重量減少は，大部分のエトキシ基が分解したことを示すものであった.[11] また，DTA 曲線で 700K 付近に現れた大きな発熱ピークは，$NaNbO_3$ の結晶化によるものと考えられる．Na-Nb 複合エトキシドの熱分解による $NaNbO_3$ の生成過程において，エトキシ基の分解生成物の脱離によりまずポーラスな非晶質体が生成し，このような非晶質体は熱処理温度の上昇により徐々に結晶化し，773K 以上では結晶性のよい粒子になることが観察された．

Fig. 3 (a)に Na-Nb エトキシドの単結晶の写真を，また (b)　(c)，それを 373K と 973K でそれぞれ 1.5 時間熱処理した試料の SEM 写真を示す．エトキシドの単結晶は約 5mm 程度で，熱処理後に得られた試料はエトキシ基の分解により数ミクロンサイズの凝集粉末になっていることがわかる．この粉末の一次粒子の大きさは，973K でもほぼ同様の大きさで，粒成長が起こった様子は観察されなかった．

TEM 観察の結果，結晶化が起こり始める温度は，XRD で回折ピークが認められる 623K より低温の 573K であることが分かった．Fig. 4 に，573K で観察した試料の TEM 像と制限視野回折 (SAD) 図を示す．回折図には非晶質を示すハローリングが観察されたが，四角で囲った中の拡大図（矢印）には明らかに格子像が観察できる．

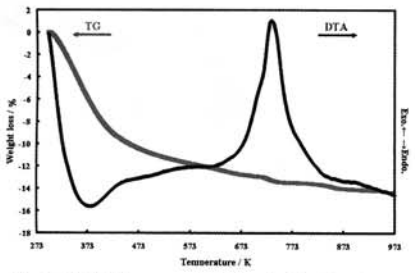

Fig. 2　TG/DTA curves of Na-Nb ethoxide. Heating rate is 10K/min.

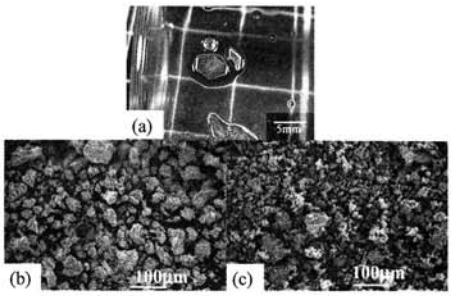

Fig. 3　Photograph of single crystal of Na-Nb etoxid. SEM images of specimen annealed (b) at 373K and (c) at 973K.

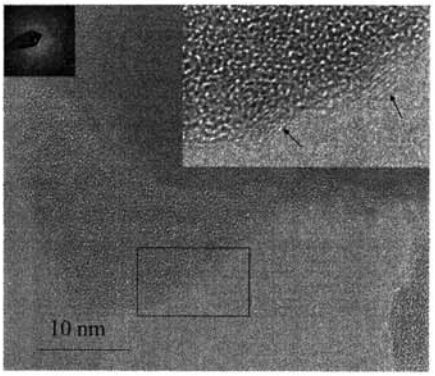

Fig. 4　TEM image of specimen annealed at 573K. Inset is a SAD patter and enlarged image.

さらに 623K および 673K で熱処理した試料を TEM 観察した結果，どちらの試料にもまだ一部に非晶質相が残ることを確認した．Fig. 5 に，673K で熱処理した試料の TEM 写真と制限視野回折図を示す．(b) は (a) の四角で囲まれた領域を拡大した写真である．試料の上部では回折スポットが検出され，格子縞もはっきり確認できるが，試料下部は非晶質相であることがわかる．

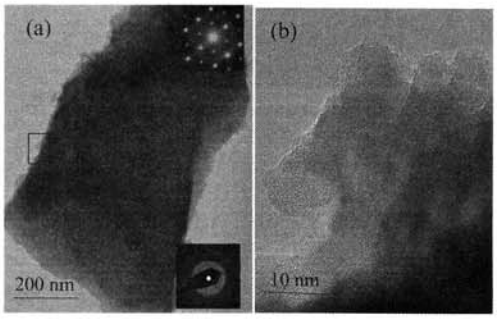

Fig. 5　(a) TEM images of specimen annealed at 673K and (b) enlarged image.

Fig. 6 (a) に，873K で熱処理された試料の TEM 像を，(b) に [001] 方向から撮影した高分解能像を示す．$NaNbO_3$ 粒子中に多数の気孔が観察され，その気孔サイズは約数十 nm 程度 (<100nm) であることがわかる．また (b) の高分解能 TEM 像では，気孔が結晶形 (001) 面の格子縞に沿った形状をしているのが観察された．

Fig. 7 は，TEM を用いて試料を ±60 度に傾斜し，一度ずつ画像を取り込んだ後にトモグラフィシステムにより三次元像を構築したものである．3 次元像からも様々な大きさの気孔 (<100nm) が粒子内に多数存在するのが確認できた．

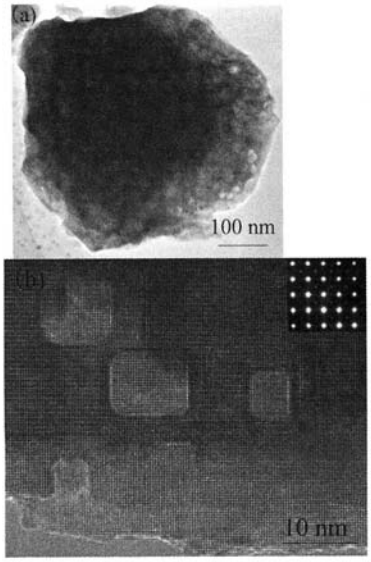

Fig. 6 (a) low-magnification TEM image of specimen annealed at 873K and (b) high-resolution TEM image. Inset is SAD pattern taken from the [001] zone axis.

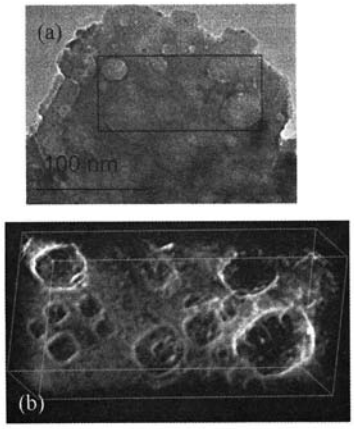

Fig. 7 Three-dimensional image of $NaNbO_3$ powder annealed at 873K. (a) reconstructed area and (b) 3D image.

3・2 $NaNbO_3$ 粒子中の気孔の熱挙動

各温度での熱処理後の微構造観察の結果，Na-Nb エトキシドの分解後に得られたポーラスな $NaNbO_3$ の組成を持つ非晶質相が，573K 以上で結晶化する過程で，母材の結晶形に沿った気孔が形成されることが推察された．そこで，熱処理により結晶化する過程で，粒子内部の気孔の熱挙動をその場観察することを試みた．観察試料は，Fig. 8 (a) に示すように，623K で熱処理しすでにエトキシ基が分解した後のポーラスで非晶質の $NaNbO_3$ を用いた．高温 TEM により徐々に温度を上げたところ，723K 付近で明らかに結晶化が起こり始め，多結晶リングが観察された (Fig. 8 (b))．その頃から気孔の動きが顕著に見え始めたので，温度を保持して観察を行った．240 秒後には，観察粒子領域が単結晶に近づいたことを示す制限視野回折パターンが観察された (Fig. 8 (c))．

Fig. 9 に，723K で温度を保持しながらビデオにより撮影した気孔の経時変化を示す．(a) はホルダー温度が 723K に達し，結晶化が進行すると共に 20nm サイズの気孔の動きが見え始めた温度である．(b)～(d) の写真はビデオによる動画から経過時間による静止画を切り取ったものである．(a) と (d) の写真を比較すると，明らかに気孔の数の減少が確認できる．(b) および (c) 中に顕著な動きのあった気孔にマークしその動きを記した．723K で約 20nm サイズの気孔の移動速度を平均すると，約 10nm/sec となった．より小さい気孔はより早い速度で移動することがビデオ映像より観察できた．移動距離は様々で，150nm 程度複雑な動きをするものから，短いものでは隣の大きな粒子に吸収されるものなど観察された．この結果から，非晶質から結晶化する際，小さな気孔が熱により移動しながら一部は試料外に抜け，一部は他の気孔と合体して大きくなることが明らかになった．また $NaNbO_3$ の結晶化に伴い，気孔の形状も $NaNbO_3$ の結晶形に合わせて変化したことが考えられる．このような気孔形状の違いは，623K で 1.5 時間熱処理した試料中にも明らかに見ることができる．

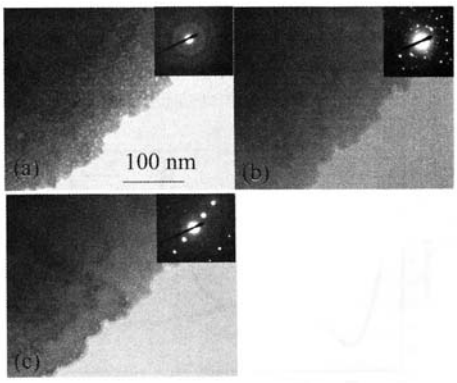

Fig. 8 TEM observations of $NaNbO_3$ using a thermal stage. (a) starting material, (b) at 723K and (c) at 723K after 240sec.

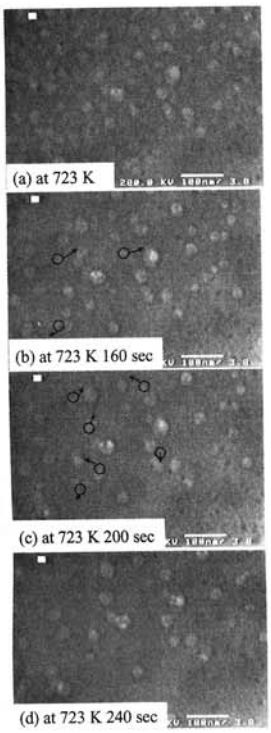

Fig. 9　Behabior of pores in the $NaNbO_3$ at 723K in TEM.

Fig. 10 (a)は，623K 熱処理により結晶化が進んだ領域で，[001] 方位から撮影した TEM 写真で，(b) はまだ非晶質の領域の写真である．(a) の粒子中の気孔は (b) に比べてやや大きく，形状も明らかに変化しているのが観察できる．さらに熱処理温度を上げると，Fig. 6 (b)のように気孔のサイズはさらに大きくなる傾向が見られた．

今回の気孔形成の特徴を，これまでに報告された sol-crystal 法による，複合アルコキシドからの $Ba_5Nb_4O_{15}$ の微粒子の結晶化過程と比較して考察する．$Ba_5Nb_4O_{15}$ の場合，773K 1.5 時間の熱処理ではまだ 2 ～ 5nm 程度の微結晶ができ始める温度であった.[10]873K でも平均 10nm

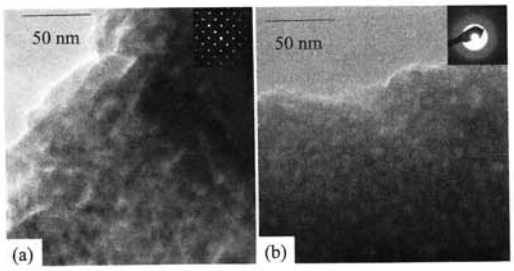

Fig. 10　TEM images of $NaNbO_3$ annealed at 623K. (a) crystal region and (b) amorphous region.

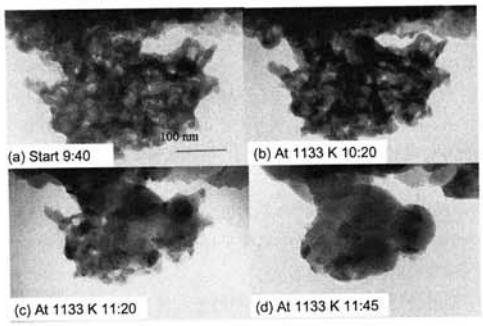

Fig. 11　Structural changes in $Ba_5Nb_4O_{15}$ by heating in TEM. Starting material is used a specimen annealed at 873K for 1.5h in air.

程度の微結晶であり，これを高温 TEM 用出発試料としてその場観察した結果を Fig. 11 に示す．高温 TEM 観察により，結晶化が顕著に進行した温度は約 1133K であり，この温度では小さな粒子が大きな粒子に吸収される様子が確認された．これにより，合体の際に内部の気孔は外部に抜け結果として密度が高い粒子を得ることができたことがわかる．これに対し，$NaNbO_3$ の場合はそれよりも低い 773K で結晶体になるため，この温度では粒子の吸収・合体が起こらず，気孔の移動距離も短く，結果として粒子内部に多くの気孔が残ったまま結晶化が進行した．この結果，ナノポーラス粒子が形成されたものと思われる．

粒子内に気孔を有するものとして，水熱合成により得られた $BaTiO_3$ 微粒子が報告されている.[12]この微粒子は，固相反応で得られた粒子に比べ密度の低さが指摘されてきた．この $BaTiO_3$ 微粒子中の気孔数は今回のように多くないが，結晶形を反映した気孔も多数観察されている.[12]このことから，水熱合成時の熱処理過程で今回と同様のメカニズムにより結晶粒内に気孔が取り残されたことが予想される．

このような特異な構造は，今後ナノ複合体への展開が期待される．今回の解析結果からナノポーラス粒子の形成メカニズムを Fig. 12 にイラストで示す．

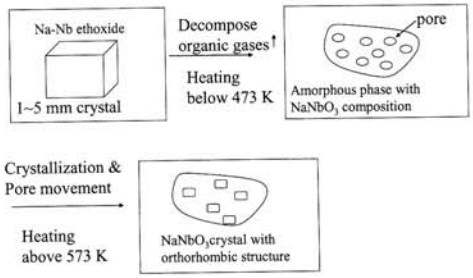

Fig. 12　Formation mechanism of nano-porous $NaNbO_3$ grain.

4 結 論

(1) Sol-crystal 法により，斜方晶構造を有する $NaNbO_3$ の微粒子を合成した．

(2) Na-Nb 複合エトキシド結晶は，473K 以下で分解して非晶質 $NaNbO_3$ が生成した．非晶質 $NaNbO_3$ は 573K から結晶化を開始し，773K 以上で完全に結晶化した斜方晶 $NaNbO_3$ の微粒子が得られた．

(3) 773K ～ 973K の熱処理により得られた粒子は，粒内に数十 nm サイズの気孔を有するナノポーラス粒子であった．

(4) ナノポーラス粒子の形成は，まず Na-Nb エトキシドが熱処理により分解してポーラスな非晶質体となる．これを 623K 以上で熱処理すると結晶化が起こり，その過程で気孔が粒子内部を動きながら結晶形に沿った形状を形成し，結果として数十ナノサイズの気孔を有する結晶粒になったことが明らかになった．

謝 辞

TEM による三次元像の撮影においてご協力頂きました日本電子㈱の遠藤憲明氏に感謝します．

参 考 文 献

1) A. W. Heawt, "Neutron powder profile refinement of ferroelectric and antiferroelectric crystal-structures-soium niobate at 22 degrees C", Ferroelectrics, Vol.74, No.1-4, pp.83-85 (1974).

2) R. V. D. Muhll, A. Sadel and P. Hagenmuller, "Structure crystalline a 295K de la phase ferroelectrique $Li_{0.02}Na_{0.98}NbO_3$", Journal of Solid State Chemistry, Vol.51, No.2, pp.176-182 (1984).

3) L. Pardo, P. Duran-Martin, J. P. Mercurio, L. Nibou and B. Jimenez, "Temperature behavior of structural, dielectric and piezoelectric properties of sol-gel processd ceramics of the system $LiNbO_3$-$NaNbO_3$", Journal of Physics Chemistry of Solids, Vol.58, No.9, pp.1335-1339 (1997).

4) M. M. Shamim, T. Isgidate and K. Ohi, "High pressure raman study of $KNbO_3$-$KTaO_3$ and $KNbO_3$-$NaNbO_3$ mixed crystals", Journal of Physical Society of Japan, Vol.72, No.3, pp.551-555 (2003).

5) H. Abdelkefi, H. Khemakham, G. Velu, J. C. Carru and R. V. D. Muhll, "Dielectric properties of ferroelectric ceramics derived from the system $BaTiO_3$-$NaNbO_3$-based solid solutions", Solid State Sciences, Vol.6, No.12, pp.1347-1351 (2004).

6) L. A. Peznitchenko, N. V. Dergunva, G. A. Gegunia, O. M. Ragumovskaya, L. A. Shilkina and L. S. Ivanova, "New binary of solid solutions based on $NaNbO_3$", Ferroelectrinic, Vol.214, No.3-4, pp.241-254 (1998).

7) T. Wada, K. Tsuji. T. Saito and Y. Matsuo, "Ferroelectric $NaNbO_3$ ceramics fabricated by spark plasma sintering", Japanese Journal of Applied Physics, Vol.42, No.9B, pp.6110-6114 (2003).

8) Y. Suyama, T. Noritake and M. Nagasawa, "Formation of $BaTiO_3$ from barium titanium isopropxide complex", Japanese Journal of Applied Physics, Vol.36, No.9B, pp.5939-42 (1997).

9) Y. Suyama and M. Nagasawa, "Synthesis of single-crystal barium titanium isopropxide complex to form barium titanate", Journal of American Ceramic Society, Vol.77, No.2, pp.603-605 (1994).

10) H. Nakano, T. Yano and Y. Suyama, "Microstructural evolution during crystallization of $Ba_5Nb_4O_{15}$ from Ba-Nb ethoxide", Journal of the Ceramic Society of Japan, Vol.113, No.1, pp.59-63 (2005).

11) Y. Hirano, T. Yamada and Y. Suyama, "Synthesis and properties of sodium niobate via Na-Nb double alkoxide", Proceedings of 20th International Japan-Korea Seminar on Ceramics, Shimane, Vol.20, pp.395-398 (2003).

12) H. Nakano, K. Urabe, T. Oikawa and H. Ikawa, "Characterization of inner pores in hydrothermal synthesized $BaTiO_3$ particles by transmission electron microscopy", Journal of American Ceramic Society, Vol.87, No.8, pp.1594-97 (2004).

セラミックス基盤工学研究センター年報 (2007). Vol. 7, 6-15

Phase Transition of Gd_3RuO_7 From a Structural Point of View

H. Nakano†, K. Tateishi‡, and N. Ishizawa¶

† Ryukoku University, Seta, Otsu 520-2194
‡ Gifu Prefectural Ceramics Research Institute, Hoshigadai, Tajimi 507-0811
¶ Ceramics Research Laboratory, Nagoya Institute of Technology, Asahigaoka, Tajimi 507-0071

構造的観点からみた Gd_3RuO_7 の相転移

中野裕美†・立石賢司‡・石澤伸夫¶

† 龍谷大学 〒 520-2194 滋賀県大津市瀬田大江町横谷 1-5
‡ 岐阜県セラミックス研究所　〒 507-0811　多治見市星ヶ台 3-11
¶ 名古屋工業大学セラミックス基盤工学研究センター　〒 507-0071 岐阜県多治見市旭ヶ丘 10-6-29

Gd_3RuO_7, the ordered oxygen-deficient fluorite-type compound, undergoes a structural phase transition between the $P2_1nb$ and *Cmcm* modifications at around 382 K. This paper describes the phase transition from a structural point of view, based on the high–temperature single-crystal X-ray and electron diffraction studies. The transition is almost reversible, and characterized by an additional tilt about the c axis that occurs in the low-temperature modification for half of the RuO_6 octahedra in association with a reduction of apparent coordination number from 6+2 to 7 for one-third of Gd atoms. Dimerization of the Ru array along the $[\text{-}RuO_5\text{-}]_\infty$ zigzagging chain occurs below the transition temperature, which provides a folding effect on the chain. The folding tendency of the chain explains geometrically an expansion of the *b*-length and a compression of the *c*-length near 382 K on cooling and *vice versa* on heating. The transition is similar to those given in the literature for Sm_3RuO_7, Eu_3RuO_7, Sm_3OsO_7, Eu_3OsO_7 and Gd_3OsO_7, except that one of crystallographically independent Gd atoms in the high-temperature *Cmcm* modification is statically or dynamically distributed between two positions located very close with each other. The disordered distribution of the Gd atom in the high-temperature modification is presumably correlated with the octahedral tilts about the *c* axis, resulting in the experimental observation of the extremely prolate atomic displacement ellipsoid for the O1 atom in the *cis* position along the chain. The $P2_1nb$-*Cmcm* phase transition contains two competing mechanisms characterized by the order-disorder transition of the librating [-Gd-RuO_6-Gd-RuO_6-Gd-] linkage along the *b* axis, and by the displacive-type dimerization of Ru atoms along the chain. The *in situ* electron diffraction experiments suggested a possible existence of intermediate phase between the high- and low-temperature modifications.

1. Introduction

Compounds of the Ln_3MO_7 series are composed of trivalent lanthanide (Ln) and pentavalent transition metal oxides and crystallizes in the defect-fluorite-type structure (Allpress & Rossel, 1979). The structure was first determined for La_3NbO_7 on the basis of the *Cmcm* symmetry. Among the Ln_3MO_7 series, Ln_3RuO_7 and Ln_3OsO_7 contain the MO_6 octahedral single-chains in the matrix composed of Ln and O atoms. The unit-cell relationship between the cubic fluorite-type parent structure (f) and the Gd_3RuO_7-type chain structure (c) is shown in Fig. 1. The crystals show the polymorphism. The phase transition between the space groups $P2_1nb$ and *Cmcm* was first reported for Sm_3RuO_7 at 190 K, and Eu_3RuO_7 at 280 K (Gemmill *et al*., 2004), and then for Sm_3OsO_7 at 235 K, Eu_3OsO_7 at 330 K, and Gd_3OsO_7 at 430 K (Gemmill *et al*., 2005).

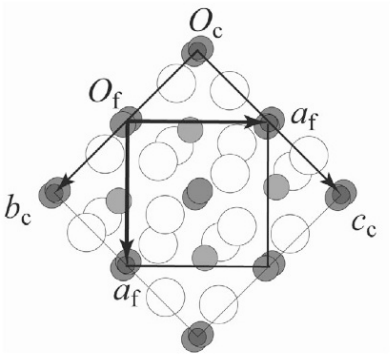

Fig. 1. The unit-cell relationship between the cubic fluorite-type parent structure (f) and the Gd_3RuO_7-type chain structure (c). Metal and oxygen atoms are represented by filled and unfilled circles, respectively.

The *Cmcm* structure is considered as archetypal, possessing the highest symmetry among the Ln_3RuO_7 polymorphs.

Bontchev *et al.* (2000) grew single crystals of Gd_3RuO_7 by the flux method and suggested that the crystal has localized carriers in one-dimension with Mott variable range hopping along the octahedral single chains. They also reported two phase transitions at 14.5 and 8 K relevant to the orderings of the Ru and Gd magnetic moments, respectively. Harada & Hinatsu (2002) found another transition at 382 K for Gd_3RuO_7 and reported from the specific heat measurement that the transition is of the first order.

The room temperature structure of Gd_3RuO_7 was first analyzed also assuming *Cmcm*, which made ourselves difficult to presume the symmetry of the high-temperature modification of Gd_3RuO_7 above 382 K. Recently, the crystal structure of Gd_3RuO_7 at room temperature was reexamined and found to possess the $P2_1nb$ symmetry (Ishizawa *et al.*, 2006). The phase transition of Gd_3RuO_7 between $P2_1nb$ and Cmcm was then detailed by the *in situ* single-crystal X-ray diffraction study (Ishizawa *et al.*, 2007). The present paper aims at filling up the unreported things which were excluded from our past papers mainly due to the space problems, and to discuss the nature of the phase transition of Gd_3RuO_7 from a structural point of view. This paper also includes a latest finding about the possible presence of intermediate phase near the phase transition obtained from the electron microscopy study.

2. Crystal shape and its relation to the structure

Crystals were grown by cooling the $SrCl_2$-RuO_2-Gd_2O_3 solution at the rate of 5 $Kmin^{-1}$ from 1373 K. Experimental details are given in our previous papers (Ishizawa et al, 2006, 2007). Metallic black crystals had a prismatic shape surrounded by {120} side faces and capped by {101}. As shown in Fig. 2, these faces correspond to the planes extending through the crystal so that they can avoid strong bonds between the pentavalent Ru cation and the divalent oxide anions. The RuO_6 octahedral chains are running along the *c* axis which corresponds to the columnar direction of the as-grown crystal. Therefore it is not difficult to distinguish the direction of the maximum electric conduction for the crystals in columnar shape.

3. Choice of space group

Precession images were reconstructed from the frame data taken by the CCD single-crystal diffractometer (Smart Apex II, Bruker) at various temperatures between 293 to 1223 K. The 0*kl* planes at 423 K and 293 K are shown in Fig. 3. In the high-temperature modification, only the reflections with *k*=even were observed due to the lattice centering.

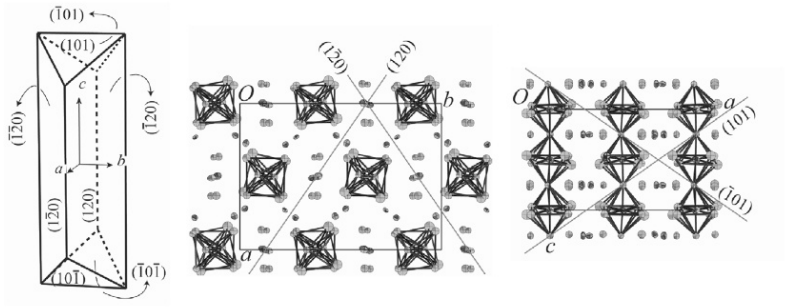

Fig. 2. Face indices of a typical as-grown crystal and their relation to structure.

In the low-temperature modification, on the other hand, satellite reflections at both sides of parent reflections appear along the *b* axis. The satellites are commensurate and can be indexed by doubling the *b*-length. The lattice loses the centering and becomes primitive.

Intensity data of the low-temperature modification were collected at 293 K up to d=0.40 Å resolution level (2θ<124° for Mo Kα) by the CCD diffractometer. Those of the high-temperature modification were collected at 423, 773 and 1223 K. Crystal data are given in Table 1. Numerical details have been given by Ishizawa *et al.*, (2007). The agreement index for the intensities of crystallographically equivalent reflections, R_{merge}, in the low-temperature modification showed no significant improvement by reducing the Laue symmetry from *mmm* to lower ones. The crystal was thus assumed to have an orthorhombic symmetry. From the systematic absence of reflections, possible space groups were limited to $P2_1nb$ and *Pmnb*. The noncentrosymmetric $P2_1nb$ was adopted because the mirror planes perpendicular to the *a* axis in the centrosymmetric *Pmnb* did not allow octahedral tilts about the axes on the planes.

Figure 4 shows the temperature dependence of the mean $|Fo|^2$ of eight reflection parity groups, eoe, ooo, ooe, eoo, 0oo, 0oe, o0o and e0o, on the basis of the $P2_1nb$ lattice. The reflections in these groups can exist in $P2_1nb$ and should disappear in *Cmcm*. The data were collected upon heating. The temperature dependence was essentially the same on cooling the specimen, suggesting that the transition is almost reversible. The mean $|Fo|^2$ of the first seven parity groups, *i.e.*, eoe, ooo, ooe, eoo, 0oo, 0oe and o0o, decreased rapidly with increasing temperature and disappeared above 382 K. The reflections of the parity group e0o were slightly stronger and more diffuse than those of the other seven groups above 382K, although the $|Fo|^2$ value of the strongest reflection in the group e0o did not exceed 3 times its estimated standard uncertainty. They were thus neglected for the space group determination.

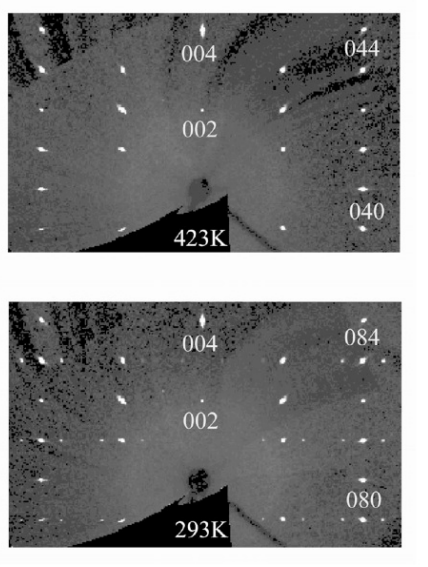

Fig. 3. Precession images of the reciprocal *0kl* plane at 423 K (*Cmcm*) and 293 K ($P2_1nb$), calculated from the CCD frame data.

Some of the Ln_3MO_7 crystals, *e.g.*, Ln_3MO_7 (M=Nb, Ta and Sb, Ln=Nd, Gd and Ho) (Allpress & Rossel, 1979), Y_3TaO_7 (Rossell, 1979), and Dy_3ReO_7 (Hinatsu *et al.*, 2004), have been reported to crystallize in the space group $C222_1$. The space groups of $C222_1$ and *Cmcm* can be distinguished from the *h*0*l* reflections, *i.e.*, the reflection group e0o

Table 1. Crystallographic Data for Gd_3RuO_7

formula	Gd_3RuO_7	Gd_3RuO_7	Gd_3RuO_7	Gd_3RuO_7
fw (g/mol)	684.82	684.82	684.82	684.82
temperature (K)	293	423	773	1223
wavelength (Å)	0.71073	0.71073	0.71073	0.71073
crystal system	orthorhombic	orthorhombic	orthorhombic	orthorhombic
space group	$P2_1nb$	*Cmcm*	*Cmcm*	*Cmcm*
unit cell dimensions				
a (Å)	10.6399(2)	10.6514(2)	10.6847(2)	10.7346(2)
b (Å)	14.6769(2)	7.3404(3)	7.3694 (1)	7.4112(2)
c (Å)	7.3747 (1)	7.3942 (1)	7.4136 (1)	7.4481(2)
volume ($Å^3$)	1151.64(3)	578.12(3)	583.75(2)	592.54(3)
Z	8	4	4	4

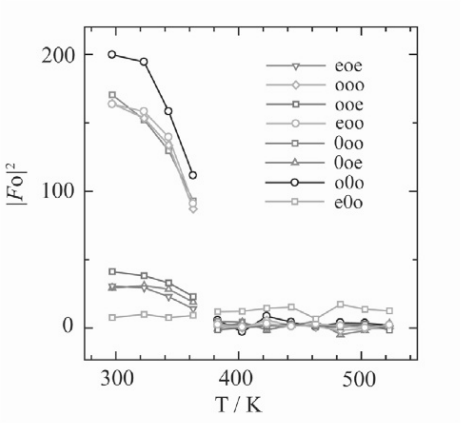

Fig. 4. Temperature dependence of the mean $|Fo|^2$ of seven reflection parity groups, eoe, ooo, ooe, eoo, 0oo, 0oe, o0o and e0o, where o and e stands for odd and even indices, respectively, on the basis of the $P2_1nb$ lattice. The data points are connected by polylines in the high- and low-temperature modifications for viewing purpose.

are allowed for $C222_1$ whereas not for *Cmcm*. The possibility of $C222_1$ was discarded for this crystal by the aforementioned reason in the present study.

4. Changes in the cell dimensions

Temperature dependences of the cell dimensions in the range between 293 K and 523 K are shown in Fig. 5. A small shrinkage of the *b*-length and an expansion of the *c*-length were observed between the 363 and 383 K data points upon heating and the reverse took place upon cooling. Between these data points lies the phase transition temperature of 382 K reported from the specific heat measurement. The changes in the cell dimensions suggest that the transition is almost reversible. The *a*-length changed monotonically and no anomaly was observed within experimental errors.

5. Octahedral tilts and distortion

The structures of the high- and low-temperature modifications are illustrated in Fig. 6. There are two crystallographically independent octahedra, $Ru1O_6$ and $Ru2O_6$ in the low-temperature $P2_1nb$ modification. The two octahedra alternate along the *c* axis by sharing the *trans* O3 atom (O_t) to form a zigzagging single chain of $[\text{-}Ru1O_5\text{-}Ru2O_5\text{-}]_\infty$. These single chains are embedded and separated with each other in a matrix consisting of Gd and O atoms. The $Ru1O_6$ octahedron has practically one tilt system about an axis parallel to the *a* axis. On the other hand, the $Ru2O_6$ octahedron has a second tilt system about an axis parallel to the *c* axis in addition to the first tilt about the axis parallel to *a*.

The two independent $Ru1O_6$ and $Ru2O_6$ octahedra in the $P2_1nb$ modification become crystallographically identical in *Cmcm*. The $Ru1O_6$ in the high-temperature modification has a single tilt system about *a*. The appearance and disappearance of the tilt about *c* for every other RuO_6 octahedra is a structural feature that characterizes the $P2_1nb$-*Cmcm* phase transition.

Several important geometrical parameters obtained from the least-squares procedure are listed in Table 2. The RuO_6 octahedra are elongated along the chain in the high-tempeature modification as seen from the ratio of $\langle Ru\text{-}O_t\rangle_2$ / $\langle Ru\text{-}O_c\rangle_4$, where O_c stands for the O1 atom in the *cis* position of octahedra with respect to O_t, and the angle brackets stand for taking an average over the number of bonds given as a subscript. The values of quadratic elongation and angle distortion in Table 2 suggest that the shape of oxygen octahedra in the high-tempeature modification resolves into more distorted $Ru1O_6$ and less distorted $Ru2O_6$ in the low-temperature modification (Robinson *et al.*, 1971). The Ru-O_t-Ru angle of 142.5 º at 423 K is slightly more obtuse

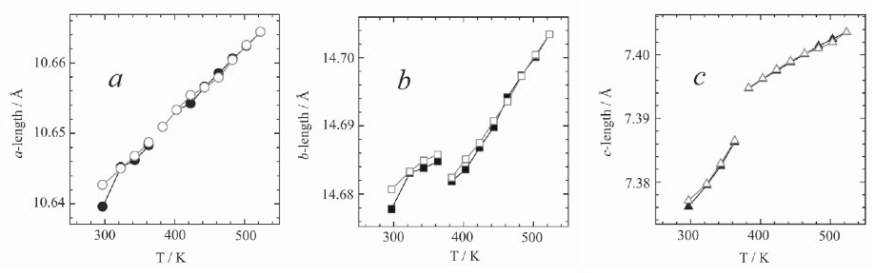

Fig. 5. Temperature dependence of the *a*-, *b*-, and *c*-lengths of Gd_3RuO_7. Data points of filled black marks on heating and open red ones on cooling are connected by polylines for viewing purpose. The *b*-length of the *Cmcm* modification above 382 K is doubled in the figure for comparison with the low-temperature $P2_1nb$ modification. The estimated standard uncertainties of the cell lengths are less than the marker size.

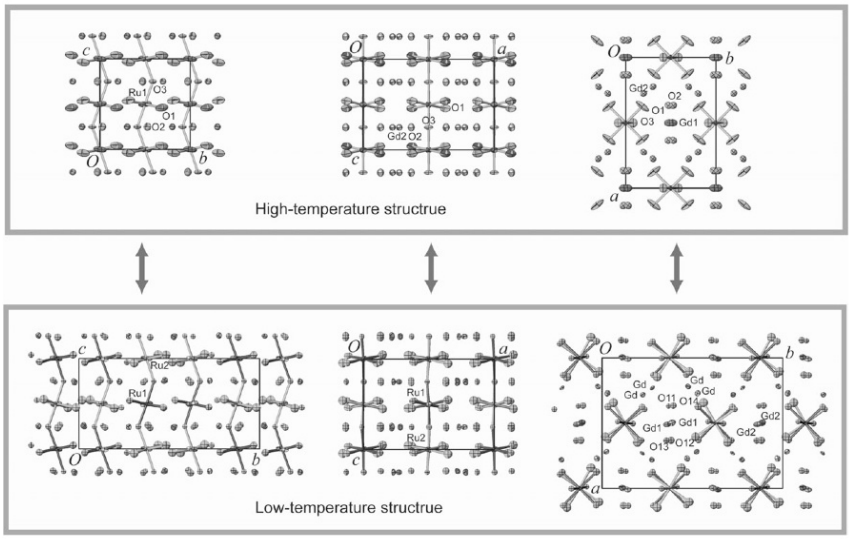

Fig. 6. Comparison of the high- and low-temperature modifications at 423 K and 293 K with atomic displacement parameter ellipsoids plotted at the 97% probability level.

Table 2. Selected interatomic distances (Å) and geometry parameters

	293 K		423 K	773 K	1223 K
<Ru1-O>$_6$ (Å)	1.947(8)		1.945(2)	1.953(4)	1.948(4)
<Ru1-O_t>$_2$ (Å)	1.945(8)		1.952(1)	1.959(2)	1.967(2)
<Ru1-O_c>$_4$ (Å)	1.948(6)		1.941(2)	1.950(4)	1.949(4)
<Ru1-O_t>$_2$ / <Ru1-O_c>$_4$	0.9985		1.0057	1.0046	1.0092
Octahedral volume (Å^3)	9.744		9.738	9.857	9.897
Quadratic elongation	1.006		1.005	1.005	1.005
Angle variance	22.85		16.94	18.65	16.78
<Ru2-O>$_6$ (Å)	1.949(7)				
<Ru2-O_t>$_2$ (Å)	1.953(6)				
<Ru2-O_c>$_4$ (Å)	1.947(8)				
<Ru1-O_t>$_2$ / <Ru1-O_c>$_4$	1.0031				
Octahedral volume (Å^3)	9.807				
Quadratic elongation	1.004				
Angle variance	14.63				
Ru1···Ru2 (Å)	3.683(4), 3.691(4)	Ru1···Ru1 (Å)	3.6971(1)	3.7068(1)	3.7241(1)
Ru1-O1-Ru2 angle (°)	140.4(5)	Ru-O3-Ru angle (°)	142.5(2)	142.2(4)	142.4(4)
Ru1-O2-Ru2 angle (°)	144.1(5)				

[a] The interatomic distances (Å) in angle brackets are the average over the shortest *n* bonds with *n* given as a subscript. The O_t represents *trans* O atoms connecting the RuO_6 octahedra along the chain, and O_c represents the other *cis* O atoms of RuO_6 octahedra.

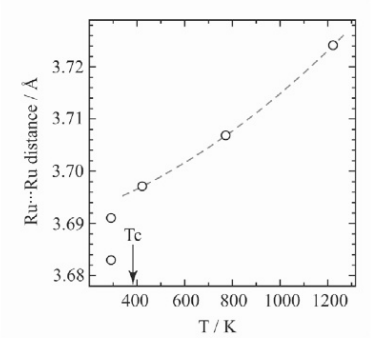

Fig. 7. Changes in the intermetallic Ru···Ru distance along the RuO_6 chain with temperature. The estimated standard uncertainties are within the marker size. Two Ru···Ru distances in the $P2_1nb$ modification at 293 K lie below the dashed quadratic polynomial line connecting the values in the *Cmcm* modification at high temperatures.

than the mean of the two Ru-O_t-Ru angles at 293K in the low-tempeature modification, *i. e.*, 140.4(5) º for Ru1-O1-Ru2 and 144.1(5) º for Ru1-O2-Ru2. This indicates that the octahedral single chain tends to unfold in the high-temperature modification.

6. Ru···Ru intermetallic distance

Along the chain, there is one kind of intermetallic Ru···Ru distance in the high-temperature modification, corresponding to the half of the *c* length, whereas there are two kinds of Ru···Ru distances in the low-temperature modification. The temperature dependence of the Ru···Ru distance is shown in Fig. 7. The Ru···Ru distance in the high-temperature modification is much larger than their mean in the low-temperature modification. The elongation of octahedra, the unfolding tendency of the chain, and the increase of intermetallic Ru···Ru distance accord geometrically with each other. They also explain the shrinkage of the *b*-length and the expansion of the *c*-length (Fig. 5) near the phase transition point upon heating and *vice versa* upon cooling. The inequality of Ru···Ru intermetallic distances along the chain in the low temperature modification (Fig. 7) indicates that the dimerization of adjacent Ru atom pairs takes place in addition to the general shortening of the Ru···Ru distances. This suggests a higher, and slightly different, electronic correlation between the Ru atoms along the chain in the low-temperature modification compared with the high-temperature one. A detailed analysis of the band structure is necessary in order to understand the phase transition as well as the conduction properties.

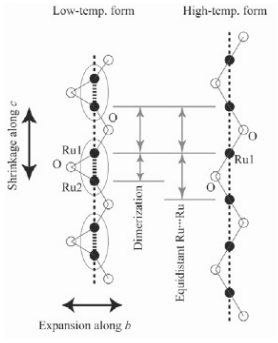

Fig. 8. Shematic drawing of the RuO_6 chain featuring the relation between the dimerization of Ru atoms and the changes of cell dimensions on the transition.

7. Dynamic disorder in the high-temperature modification

The RuO_6 octahedral single chains are bridged with each other along the *b* axis by the Gd1-O1 bonds, as shown in Fig. 9. The bridging is symmetrical in the high-temperature modification due to the presence of mirror planes perpendicular to the *a* axis. The presence of mirrors prevents octahedral tilting about *c*. Below the transition temperature, each Gd1 atom releases one bond to RuO_6 octahedron, enabling a tilt about *c* for every other RuO_6 octahedra. This is essentially the same as those reported for the $P2_1nb$-*Cmcm* phase transitions in Sm_3RuO_7 and Eu_3RuO_7, Sm_3OsO_7, Eu_3OsO_7 and Gd_3OsO_7 .

The *Cmcm* structures determined at 423, 773 and 1223 K are shown in Fig. 10. The distance of the Gd atom split pair was approximately 0.3 Å, and did not show any significant temperature dependence. The atomic displacement parameters increased almost linearly as a function of temperature. It is notable that only the O1 atom in *cis* position has an extremely prolate atomic displacement parameter ellipsoid, as the overlapped Gd1 split pair looks like in Fig. 9.

The coordination geometry around Gd1 can be modified depending on the actual Gd1 atom location in the spilt pair. Figure 11 illustrates four possible geometries in the high-temperature modification. The directions of Gd1 atom shifts are the same in (a) and (b), and are reversed in (c) and (d). The Gd1 atom is coordinated by two O_c atoms of an octahedron by occupying a closer position to the octahedron. On the other hand, the shift provides to the other adjacent octahedron one of the two possible tilts (clockwise or counterclockwise) about the axes close to *c*, by releasing one Gd1- O_c bond. Depending on the directions of Gd1 atom shifts,

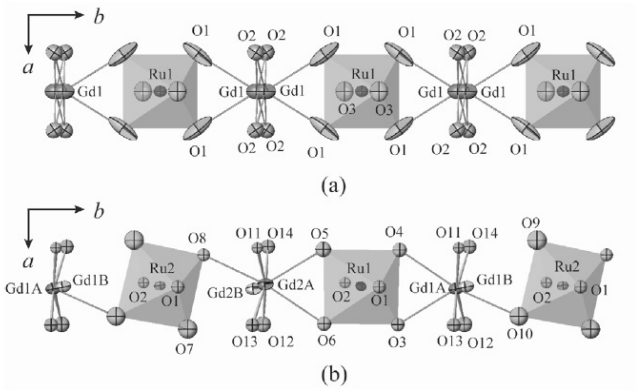

Fig. 9. The [-Gd-RuO_6-Gd-RuO_6-Gd-] linkage in the *Cmcm* (a) and $P2_1nb$ (b) strcutrues.

half number of octahedra accomodate tilts whereas the remaining half remain untilted. The geometries of (c) and (d) have the antiphase relation against (a) and (b) along the *b* axis, respectively.

The *Cmcm* structure can be considered as a superposition of four variants with different geometries. Although each geometry has a doubled periodicity of the *Cmcm* structure along the *b* axis, the superposition reduces it into the original value. The O_c atoms are located at the corners of clockwise-tilted, counterclockwise-tilted and untilted octahedra. Superposing all the possible geometries would then make the probability density distribution of O_c rather complicatedly elongated along the arc connecting the octahedral corners. Actually a simple superposition would give rise to a probability density distribution profile composed of three peaks weighted by 1:2:1 along the arc about the tilt axis. Such distribution is difficult to analyze on the basis of a simple split atom model for O_c. It is also suggested that these four geometries exist in the high-temperature modification not statically but dynamically because the phase transition at 482 K prescribes these geometries to get ordered in the low-temperature modification. In this regard, the $P2_1nb$-*Cmcm* phase transition can be considered as an order-disorder transition of the librating [-Gd-RuO_6-Gd-RuO_6-Gd-] linkage along the *b* axis. This is consistent with the study of the specific heat measurement (Harada & Hinatsu, 2002). The present time-averaged X-ray analysis assumes simple harmonic vibrations for constituent atoms. The prolate feature of O1 ellipsoids thus obtained in the high-temperature modification implys a possible

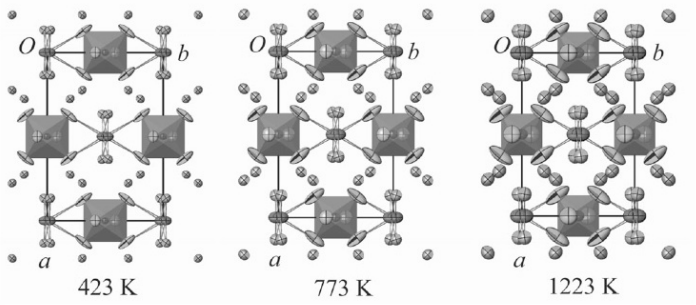

Fig. 10. Changes of the *Cmcm* structures projected along the *c* axis as a function of temperature. The anisotropic displacement parameter ellipsoids are plotted at the 97% probability level. The split atom pair of Gd1 (red) is partially overlapped and looks elongated along the *b* axis in the figure. Four shortest Gd1-O bonds are colored in light blue and the next four in red.

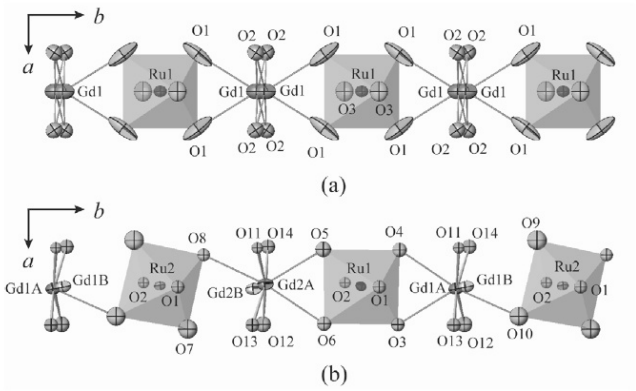

Fig. 9. The [-Gd-RuO_6-Gd-RuO_6-Gd-] linkage in the *Cmcm* (a) and $P2_1nb$ (b) strcutrues.

half number of octahedra accomodate tilts whereas the remaining half remain untilted. The geometries of (c) and (d) have the antiphase relation against (a) and (b) along the *b* axis, respectively.

The *Cmcm* structure can be considered as a superposition of four variants with different geometries. Although each geometry has a doubled periodicity of the *Cmcm* structure along the *b* axis, the superposition reduces it into the original value. The O_c atoms are located at the corners of clockwise-tilted, counterclockwise-tilted and untilted octahedra. Superposing all the possible geometries would then make the probability density distribution of O_c rather complicatedly elongated along the arc connecting the octahedral corners. Actually a simple superposition would give rise to a probability density distribution profile composed of three peaks weighted by 1:2:1 along the arc about the tilt axis. Such distribution is difficult to analyze on the basis of a simple split atom model for O_c. It is also suggested that these four geometries exist in the high-temperature modification not statically but dynamically because the phase transition at 482 K prescribes these geometries to get ordered in the low-temperature modification. In this regard, the $P2_1nb$-*Cmcm* phase transition can be considered as an order-disorder transition of the librating [-Gd-RuO_6-Gd-RuO_6-Gd-] linkage along the *b* axis. This is consistent with the study of the specific heat measurement (Harada & Hinatsu, 2002). The present time-averaged X-ray analysis assumes simple harmonic vibrations for constituent atoms. The prolate feature of O1 ellipsoids thus obtained in the high-temperature modification implys a possible

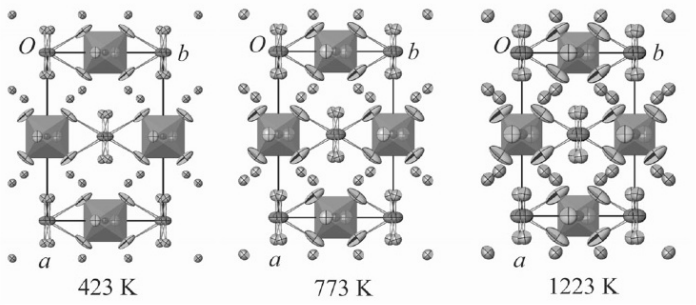

Fig. 10. Changes of the *Cmcm* structures projected along the *c* axis as a function of temperature. The anisotropic displacement parameter ellipsoids are plotted at the 97% probability level. The split atom pair of Gd1 (red) is partially overlapped and looks elongated along the *b* axis in the figure. Four shortest Gd1-O bonds are colored in light blue and the next four in red.

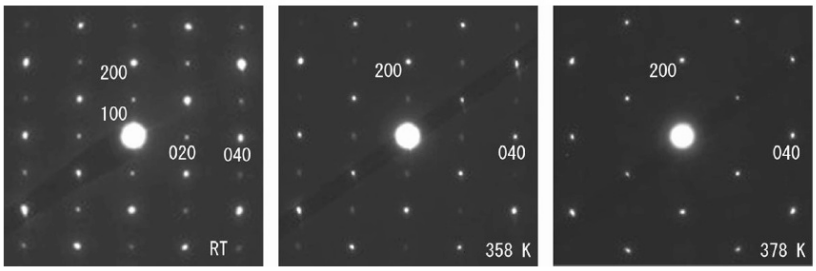

Fig. 13. Changes in the [001] zone axis electron diffration pattern as a function of temperature. The 100 reflection is probably due to multipe diffraction. Satellite reflections were scarcely observed in this sample.

respectively. The Gd atoms also occupy either positions Gd2A or Gd2B with probabilities of approximately 93% and 7 %, respectively. The high correlation between the probabilities of 92-93% at the Gd1A and Gd2A sites suggests a possible coexistence of major variants containing Gd atoms at the A sites and minor variants containing Gd atoms at the B sites in the crystal.

9. Electron diffraction

The *in situ* observation of the electron diffraction pattern was carried out using JEM-2000EX and EM-SHU2 specimen holder (JEOL). The [001] zone axis electron diffraction patterns at room temperature, 358 and 378 K are shown in Fig. 13. Due to presence of the lattice centering in the high-temperature modification, the reflections with $h+k$=odd should become extinct. Since the indices in Fig. 13 are given based on the $P2_1nb$ lattice with doubled b-length compared with the high-temperature modification, the extinction rule is apparently modified as $h+k/2$=odd. Actually, the reflections 020, 220, 140, 340, etc., become week at 358 K and almost disappear at 378 K in Fig. 13. This is consistent with the X-ray diffraction study.

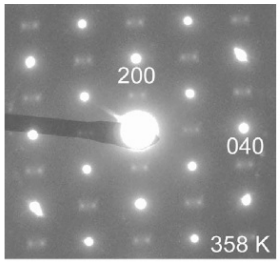

Fig. 14. The [001] zone axis electron diffraction pattern at 358 K Satellite reflections were clearly observed in many samples.

On the other hand, many crystals showed an interesting behavior when they are heated close to the phase transition temperature. A typical [001] zone axis electron diffraction pattern is shown in Fig. 14. The pattern taken at 358 K has diffuse split pairs near the *hkl* reflections with $h+k/2$=odd. These satellites align along the b axis at both sides of the reflections with $h+k/2$=odd. The center reflections with $h+k/2$=odd gradually lost their intensity upon heating whereas the satellites became even stronger. The satellites then disappeared suddenly at the transition point and the the diffraction pattern changed into that of the high-temperature modification as shown in the rightmost photograph in Fig. 13. The reverse took place upon cooling.

The diffuse split satellites suggest a possible existence of intermediate phase near the phase transition temperature. As discussed in the sections 7 and 8, the transition assumes both properties of the order-disorder and displacive types. If there is a difference in temperature between the two events of termination/initiation of the libration of the [-Gd-RuO_6-Gd-RuO_6-Gd-] linkage and the dimerization/dedimerization of the Ru atoms, then an inhomogeneous stress field should appear in the crystal between these events. This could trigger off the intermediate phase.

10. Relation to the other Ln_3RuO_7 compounds

Gemmill *et al.* (2004) reported that the refinement of the *Cmcm* modifications of Eu_3RuO_7 turned out a poorer fitting than that of Sm_3RuO_7. The anisotropic atomic displacement parameters of Sm1 and Eu1 atoms in these compounds are approximately 4-times prolate along b, and the values for Eu1 are approximately 50 % larger than those for Sm1. This may indicate that the harmonic approximation of a

non-split Ln1 atom model becomes less appropriate for describing the *Cmcm* structure with decreasing ionic radii in the sequence of Ln = Sm^{3+} ($4f^5$), Eu^{3+} ($4f^6$), and Gd^{3+} ($4f^7$).

The $P2_1nb$ modifications have been found recently for Ln_3RuO_7 (Ln=Tb^{3+} ($4f^8$), Dy^{3+} ($4f^9$)) at room temperature. They are also expected to undergo the $P2_1nb$-*Cmcm* phase transition at high temperatures. If the known phase transition temperatures are plotted against ionic radii of Ln atoms, similar transitions are expected to occur at roughly estimated temperatures of 440 K for Tb_3RuO_7 and 510 K for Dy_3RuO_7. The disorder in the high-temperature modification is also expected for the Tb and Dy compounds, which are subjects of future investigation.

11. Summary

Structural phase transition of trigadorinium ruthenium heptaoxide, Gd_3RuO_7, has been investigated by *in situ* high-temperature X-ray and electron diffraction. A small shrinkage of the *b*-length and an expansion of the *c*-length were observed between 363 and 383 K with increasing temperature. No significant change occurred in *a*-length within experimental errors. The changes were essentially reversible against temperature. Structures of the high-temperature modification have been determined at 423, 773, and 1223 K assuming the orthorhombic *Cmcm* symmetry. The structure of the low-temperature modification has been determined at 293 K, assuming the orthorhombic $P2_1nb$ symmetry with doubled unit cell along the *b*-axis of the high-temperature modification. The transition from high- to low-temperature modification can be structurally characterized by tilts about axes close to the *c*-axis occurring on half of the RuO_6 octahedra. These octahedral tilts couple with a reduction in coordination number of the Gd atom bridging the adjacent RuO_6 single chains along the *b*-axis. Dimerization of the Ru array along the chain occurs on the transition, which provides a folding effect on the zigzagging chain in the low-temperature modification. The present study also revealed a presence of structural disorder in the *Cmcm* structure that had not been reported for lanthanide ruthenates (Ln_3RuO_7) and osmates (Ln_3OsO_7) in the literature. The disorder includes a dynamical or static distribution of h-third of Gd atoms in the unit cell, which is presumably linked to the libration of the octahedral tilts about the axes close to *c*. The $P2_1nb$-*Cmcm* phase transition can be considered as an order-disorder transition of the librating[-Gd-RuO_6-Gd-RuO_6-Gd-]linkage. Similar phase transitions are expected to occur in Ln_3RuO_7 (Ln=Tb, Dy) with smaller Ln cation sizes at higher temperatures than Gd_3RuO_7. The *in situ* electron diffraction experiments on Gd_3RuO_7 revealed a possible existence of intermediate phase between the high- and low-temperature modifications.

Acknowledgements

This study was supported by Grants-in-Aid for Scientific Research No. 18560662 (HN) and No. 18206071 (NI) from the Japan Society for the Promotion of Science. One of the authors (KT) has been involved in this study as a researcher of the Project Laboratory based on the program of the Ministry of Education, Culture, Sports, Science and Technology “Cooperation for Innovative Technology and Advanced Research in Evolutional Area, West Tounou, Gifu Prefecture”.

References

Allpress, J. G. ; Rossel, H. J. *J. Solid State Chem.* **1979**, 27 105-114.

Bontchev, R. P.; Jacobson, A. J.; Gospodinov, M. M.; Skumryev, V.; Popov, B.Lorenz V. N.; Meng, R. L.; Litvinchuk, A. P.; Iliev, M. N. *Phys. Rev. B.* **2000**, 62, 12235-12240.

Gemmill, W.R.; Smith, M.D.; zur Loye, H-C. *Inorg Chem.* **2004**, 43, 4254-4261.

Gemmill, W. R.; Smith, M. D.; Mozharivsky, Y. A.; Miller, G. J.; zur Loye, H-C. *Inorg. Chem.* **2005,** 44, 7047-7055.

Groen, W. A.; van Berkel, F. P. F.; IJdo, D. J. W. *Acta Cryst.* **1987**, C43, 2262-2264.

Harada, D.; Hinatsu, Y. *J. Solid State Chem.* **2002**, 164, 163-168.

Hinatsu, Y.; Wakeshima, M.; Kawabuchi, N.; Taira, N. *J. Alloys Comp.* **2004**, 374, 79-83.

Ishizawa, N.; Hiraga, K.; du Boulay, D.; Hibino, H.; Ida, T.; Oishi, S. *Acta Cryst. Section E,* **2006**, E62, i13-i16.

Ishizawa, N.; Tateishi, K.; Kondo S.; Suwa, T. *Inorganic Chemistry* **2007**, 47[2], 558-566.

Ishizawa, N.; Suwa, T.; Tateishi, K. *Acta Cryst. Sect. E.,* **2007**, E63, i163

Robinson, K.; Gibbs, G. V.; Ribbe, P. H. *Science* **1971**, 172, 567-570.

Rossell, H. J. J. *Solid State Chem.* **1979**, 27, 115-122.

Available online at www.sciencedirect.com
ScienceDirect
Acta Materialia 55 (2007) 2423–2432
Acta MATERIALIA
www.actamat-journals.com

Grain shrinkage driven by surface and grain boundary energy in $Ba_5Nb_4O_{15}$ powder

Hidehiko Tanaka [a,*], Hiromi Nakano [b], Y. Suyama [c]

[a] Nano Ceramics Center, National Institute for Materials Science, 1-1 Namiki, Tsukuba, Ibaraki 305-0044, Japan
[b] Electron Microscope Laboratory, Faculty of Science and Technology, Ryukoku University, 1-5 Yokotani Seta-Ooe, Otsu, Shiga 520-2194, Japan
[c] Division for Research Science and Engineering, Shimane University, 1060 Nishikawatsu, Matsue, Shimane 690-8504, Japan

Received 1 March 2006; received in revised form 3 October 2006; accepted 21 November 2006
Available online 7 March 2007

Abstract

The shrinkage and disappearance of small $Ba_5Nb_4O_{15}$ grains in a large grain matrix at 1133 K observed by transmission electron microscopy (TEM), included grain volume and boundary shrinkage. Rate equations for these processes were formulated based on the concept that total excess free energy directly stimulates material transport in volume, surface, or grain boundary diffusion. Based on these equations, grain vanishing was simulated and it was found that volume diffusion combined with boundary diffusion occurred, and high grain boundary energy and low grain boundary diffusivity made grains vanish while maintaining a truncated spherical shape.

Keywords: Grain growth; Sintering; Theory; Surface energy; Grain boundary energy

1. Introduction

$Ba_5Nb_4O_{15}$ materials have excellent dielectric properties potentially applicable in microwave communication [1,2]. Fine, homogeneous, pure powders are required for realizing high performance dielectricity. We prepared very fine $Ba_5Nb_4O_{15}$ precursors from double-metal alkoxides by sol–gel mixing, and crystallized fine powder by heat treatment. We observed a polycrystalline structure in transmission electron microscopy (TEM) with a hot stage to clarify consolidation and crystallization [3]. We found that small grains joining to large-grain substrates shrank and vanished into the substrate – a phenomenon attracting much interest in sintering, grain growth and grain coalescence.

When ceramic powder compacts are heated at elevated temperatures, sintering, grain growth and coalescence occur in contacting grains. These processes have been widely analyzed theoretically, experimentally and numerically, yielding large numbers of reports on these phenomena. Classical theories proposed by Kuczynsky and coworkers [4–6] first showed that neck growth between grains was a characteristic feature of sintering and densification. The theories were refined [7–10] and expanded to include numerical treatment [11–19] and finite element method analysis [20–22]. Different morphological changes in grains such as rod arrays, three-dimensional grain compacts and packed grains with pores have been simulated. All of these analyses assumed that the chemical potential gradient made by differences in curvatures and tension on grain drives material transport for shape change. A mechanical approach to the sintering was undertaken by Bordia and Scherer [23]. They treated the deformation of materials as viscous flow using a constitutive model.

Svoboda and Riedel [16] had first taken into account the free energy dispersion rate in sintering. Their analytical solution of a quasi-equilibrium model yielded essentially almost the same results as the use of numerical methods on densification behavior of grain compacts. Wakai and Aldinger [24] numerically calculated the equilibrium configuration of joining grains by minimizing the total surface and grain boundary energy. In their work, the

* Corresponding author. Tel.: +81 29 860 4476; fax: +81 29 851 3613.
E-mail address: tanaka.hidehiko@nims.go.jp (H. Tanaka).

1359-6454/$30.00
doi:10.1016/j.actamat.2006.11.037

morphological evolutions during sintering and grain growth were well simulated. Computer simulations using the Monte-Carlo method and molecular dynamics [25–28] also succeeded in visualizing complicated sintering and grain growth behaviors. Energy changes during material transport appeared to control morphological evolutions in these latter studies.

We tried a new approach to sintering and grain growth, assuming that sintering and grain growth are driven directly by surface and grain boundary energy. Sintering and grain growth decrease the sum of surface energy and grain boundary energy, so an excess of this energy in grains drives material transport for powder densification or grain coarsening. Material transport is also proportional to the shape factor and mobility, i.e., the diffusion area divided by the diffusion length and diffusion coefficient. We previously proposed a simple rate equation for material transport driven by excess free energy [29–32]. From this concept, termed "free energy material transport theory", we succeeded in formulating new rate equations for sintering and grain growth of spherical grains, and simulated the grain shape evolution of small grains. The theory could directly take into account grain boundary energy, concluding that the ratio of grain boundary energy to surface energy was the most important controlling factor for sinterability of ceramic powders. It also made clear the non-sinterability of covalent bonding ceramic powders and a role of sintering additives.

TEM observation of $Ba_5Nb_4O_{15}$ powder in this study showed that grains on the flat surface shrank and quickly vanished, suggesting to us that the free energy material transport theory was applicable to this phenomenon, so we undertook simulation of grain evolution. Here, we first report the modeling of shrinkage on a flat surface and formulate two rate equations for grain shrinkage and boundary shrinkage, rigorously taking into account volume (bulk or lattice) diffusion, surface diffusion and grain boundary diffusion. We then simulate the grain vanishing actually observed on the TEM hot stage. We also discuss the role of surface and grain boundary energy and their diffusion.

2. Experiments and results of TEM observation

$Ba_5Nb_4O_{15}$ powder was synthesized by sol–gel mixing of $Nb(OEt)_5$ and $Ba(OEt)_2$. Powder crystallized in situ at 1133 K in a TEM using a thermal specimen stage. Grains on the large grain matrix found in agglomerated powder shrank and vanished after ~10 min at this temperature. Shrinking was recorded with a video camera as detailed elsewhere [3]. TEM photographs were copied from the video image files. Shape parameters – surface perimeter, *ps*; grain boundary diameter, *db*; and the area of grain projection, *ag* – were measured with an image analyzer. TEM photographs and shape parameters are shown in Fig. 1. White arrows in Fig. 1 indicate the shrinking grain. Table 1 shows that shape parameters *ag*, *ps* and *dg* decreased. Note that although the shape flattened as the grain shrank, it kept a truncated spherical shape, indicating that both surface and grain boundary decreased, as discussed in the sections that follow.

3. Modeling and derivation of rate equations

3.1. Modeling of shrinking grains

Grains observed in Fig. 1 are compared analogously to a truncated sphere on a flat surface. Grain volume and boundary area shrinkage are involved in these processes, denoted as grain shrinkage and reverse sintering. The shape evolution of the grain in Fig. 1 is modeled by the combination of grain shrinkage and reverse sintering (Fig. 2). In the model of grain shrinkage (Fig. 2a), grain volume decreases with constant grain boundary area. In reverse sintering (Fig. 2b), grain boundary area decreases without volume change in the grain. Material transport proceeds in volume, surface and grain boundary diffusion concurrently and independently.

Geometric parameters are defined by Eq. (1),

$$X = \frac{x}{r}, \quad R = \frac{r}{r_0}, \quad R_0 = \frac{r_0}{r_{0i}}, \quad \alpha = \frac{\varepsilon_{gb}}{\varepsilon_{sf}} \tag{1}$$

where x is the distance between the grain center and boundary; r, r_0 and r_{0i} are the radii of the truncated grain, the spherical grain with the same volume as the grain and the initial grain, respectively; ε_{sf} and ε_{gb} are surface and grain boundary energies; and α is the ratio of grain boundary to surface energy. R, R_0 and α are in the range from 0 to 1 and X from -1 to 1.

3.2. Material transport driven by excess free energy

Original sintering theories proposed by Kuczynsky and co-workers [4–6] had already treated almost all basic concepts of sintering. Material flux j flows according to Fick's law

$$j = \frac{\mathrm{d}v/\mathrm{d}t}{a_x} = -D_x\frac{\mathrm{d}C}{\mathrm{d}x} = -\frac{D_x\nabla\mu}{kT} \tag{2}$$
$$\mu = 2\gamma\kappa\Omega, \quad \nabla\mu = \mu_{source} - \mu_{sink}$$

where D is diffusion coefficient, μ is chemical potential, γ is capillary force or tension, κ is curvature. The source and sink are surface and neck at grain boundary. μ_{source} is usually neglected because $\kappa_{neck} \gg \kappa_{surface}$ and the driving force is surface tension γ_{sf}.

In the new models (Fig. 2), the surface and grain boundary are taken into account. The solid grain on a flat substrate has free energy associated with the surface and grain boundary. The grain shrinks and vanishes regardless of whether the grain boundary remains or disappears at equilibrium. The difference in free energy between these two states is thought to drive grain shrinkage and reverse sintering. In previous studies [29–32], Inomata and Tanaka proposed the rate equation for material transport, $\mathrm{d}v/\mathrm{d}t$, given by Eqs. (3) and (4)

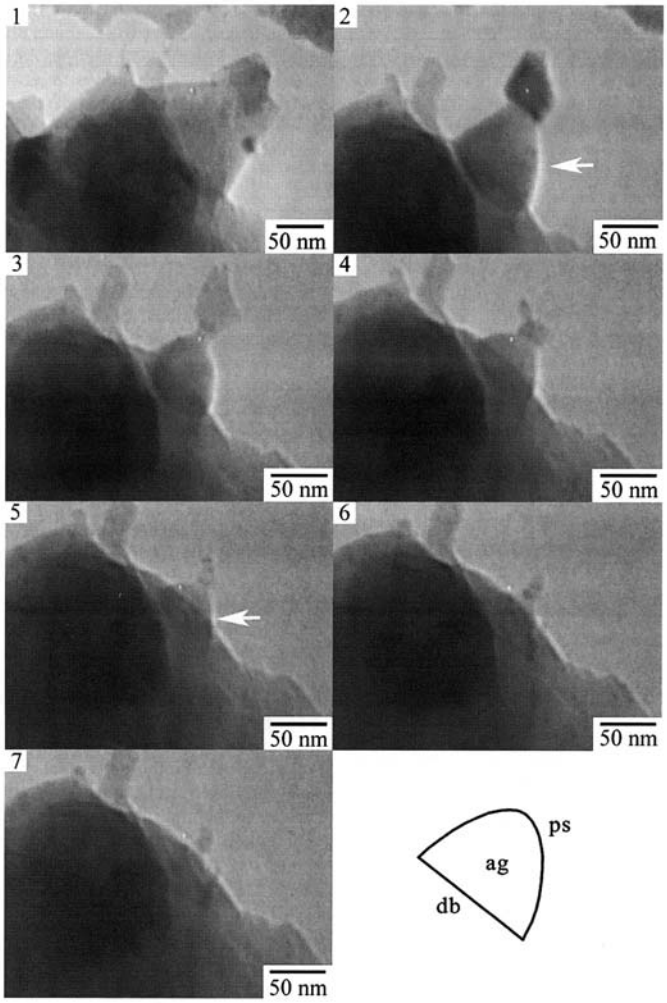

Fig. 1. Shape change and vanishing of $Ba_5Nb_4O_{15}$ grain at 1133 K on hot TEM stage. Times of observations are listed in Table 1. Shapes are compared analogously by a nearly truncated sphere with: *ag*, area of grain; *ps*, periphery of surface; *db*, grain boundary diameter.

$$\frac{dv}{dt} = D_x\left(\frac{a_x}{\lambda_x}\right)\exp\left(1-\frac{\Delta G}{RT}\right) \approx D_x\left(\frac{a_x}{\lambda_x}\right)\left(\frac{\Delta G}{RT}\right) \tag{3}$$

$$\frac{1}{\left(\frac{a_x}{\lambda_x}\right)} = \frac{\int \frac{1}{\frac{a_m(x)}{\lambda(x)}}\,dv}{\int dv} \quad \text{and} \quad \frac{1}{a_m(x)} = \frac{\int \frac{1}{a(x)}\,dx}{\int dx} \tag{4}$$

where D_x is the diffusion coefficient of the material, (a_x/λ_x) is the term of diffusion area and length, and R and T are the gas constant and temperature. The driving force for material transport for sintering and grain growth is

$$\Delta G = \Delta(\varepsilon_{sf}s_{sf} + \varepsilon_{gb}s_{gb})$$

for the models shown in Fig. 2, where ε_{sf} and ε_{gb} are surface and grain boundary energy, respectively, and s_{sf} and s_{gb} are areas of surface and grain boundary, respectively.

(a_x/λ_x) in Eq. (4) is obtained by harmonic averaging mean cross-sectional diffusion area $a_m(x)$ divided by effective diffusion length $\lambda(x)$ at x over the entire volume. Eq. (3) indicates that the rate of material transport is proportional to the diffusion coefficient D, the shape factor (a_x/λ_x) and the excess free energy of the system ΔG.

Table 1
Change in grain shape parameters measured from Fig. 1

Photo no.	Time (min)	Area of grain projection, *ag* (nm^2)	Grain radius r_0 (nm)	Surface Perimeter *ps* (nm)	Boundary Diameter *db* (nm)
1	0.00 (0.00)[a]	9047.3	53.6	262.6	140.1
2	4.12 (0.43)	4453.1	37.6	179.3	88.7
3	6.47 (0.67)	2599.6	28.7	134.4	70.8
4	7.69 (0.78)	1640.4	22.8	102.0	63.5
5	8.80 (0.91)	1025.8	18.0	80.8	55.7
6	9.48 (0.98)	314.8	10.0	43.3	34.6
7	9.63 (1.00)	0.0	0.0	0.0	0.0

[a] Time in parentheses is relative to grain vanishing.

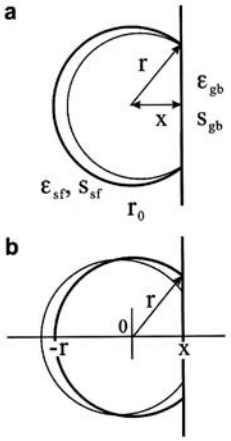

Fig. 2. Models for (a) grain shrinkage and (b) reverse sintering. x is the distance between the grain center and boundary; r and r_0 are the radius of the truncated grain and that of spherical grain with the same volume as the grain, respectively. ε_{sf}, s_{sf}, s_{gb} and ε_{gb} are the surface area, surface energy, grain boundary area and grain boundary energy, respectively.

Eq. (3) is obtained by integration of Eq. (2) over the whole system [33] and the equation is consistent with diffusion Eq. (2) [32].

3.3. Rate equations for grain shrinkage and reverse sintering

The grain in Fig. 2a shrinks to zero volume, leaving the constant grain boundary and decreasing surface area to the area equal to the grain boundary. Excess energy for grain shrinkage, ΔG_{gs}, is given by Eq. (5),

$$\Delta G_{gs} = \frac{(s_{sf}\varepsilon_{sf} + s_{gb}\varepsilon_{gb}) - (s_{gb}\varepsilon_{sf} + s_{gb}\varepsilon_{gb})}{\left(\frac{V}{V_m}\right)} = \frac{\varepsilon_{sf}V_m}{r_0} G_{gs}(R,X)$$

$$G_{gs}(R,X) = \frac{3}{R(2-X)} \tag{5}$$

where s_{sf} and s_{gb} are the areas of open surface and grain boundary, respectively, and V and V_m are the volume of the grain and the molar volume, respectively (for derivation of the equations, see Appendix A).

For the reverse sintering grain in Fig. 2b, the energy of the system E_{sys} is the sum of the surface energy and grain boundary energy, $E_{sys} = (s_{sf}\varepsilon_{sf} + s_{gb}\varepsilon_{gb})/(V/V_m)$. It has a minimum, $E_{sys,min}$, at $X = \alpha$. Excess free energy ΔG_{rs} for reverse sintering is $E_{sys} - E_{sys,min}$, calculated as Eq. (6)

$$\Delta G_{rs} = E_{sys} - E_{sys,min} = \frac{\varepsilon_{sf}V_m}{r_0} G_{rs}(R,X,\alpha) \quad \text{and}$$

$$G_{rs}(R,X,\alpha) = \frac{3}{2}\left[R^2\left\{(1+X) + \frac{1}{2}\alpha(1-X^2)\right\} - \{2(1+\alpha)^2(2-\alpha)\}^{1/3}\right] \tag{6}$$

At $X = \alpha$ and $\Delta G_{rs} = 0$, the grain is in an equilibrium state. $X = \cos\theta$ and $\varepsilon_{sf}\cos\theta = \varepsilon_{gb}$ in Fig. 2b where θ is the dihedral angle between the surface and substrate at the boundary; ε_{sf} and ε_{gb} balance with each other. The so-called Young–Dupré's relation holds if ε_{sf} and ε_{gb} are physically the same as γ_{sf} and γ_{gb}.

Four types of diffusion control grain shape change: volume diffusion, surface diffusion, grain boundary diffusion vertical to the grain boundary, and grain boundary diffusion radially in the grain boundary, as shown schematically in Fig. 3, where the diffusion path for volume diffusion is

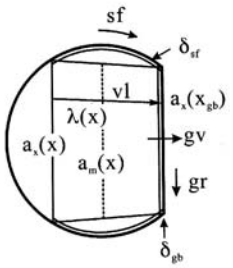

Fig. 3. Diffusion paths for volume diffusion vl, surface diffusion sf, grain boundary diffusion vertically to grain boundary gv, and grain boundary diffusion radially in grain boundary gr. $a_x(x)$, $a_m(x)$ and $a_x(x_{gb})$ are cross-sectional diffusion, mean cross-sectional diffusion area and outlet diffusion area, respectively. $\lambda(x)$ is effective diffusion length. δ_{gb} and δ_{sf} are thicknesses of grain boundary and surface layer, respectively.

shown by vl, surface diffusion by sf, grain boundary diffusion vertical to the grain boundary by gv, and grain boundary diffusion radially in the grain boundary by gr. Grain boundary diffusion vertical to and radially in the grain boundary contribute only to grain shrinkage and reverse sintering, respectively.

We calculate diffusion path terms from Eq. (4), resulting in Eq. (7)

$$\left(\frac{a_x}{\lambda_x}\right)_{\mathrm{vl}} = \pi r_0 L_{\mathrm{vl}}(R,X) \quad \text{and}$$

$$L_{\mathrm{vl}}(R,X) = \frac{4}{3}\frac{(1-X^2)^{1/2}}{R^2\left\{\frac{1}{2}X^2(1-X^2)^{1/2}+\frac{1}{2}X\arcsin X+\frac{1}{4}\pi X+\frac{1}{3}(1-X^2)^{3/2}\right\}}$$

for volume diffusion

$$\left(\frac{a_x}{\lambda_x}\right)_{\mathrm{sf}} = \pi\delta_{\mathrm{sf}} L_{\mathrm{sf}}(R,X) \quad \text{and}$$

$$L_{\mathrm{sf}}(R,X) = \frac{2(1+X)}{\ln\frac{2}{(1-X)}}$$

for surface diffusion, where δ_{sf} is surface thickness

$$\left(\frac{a_x}{\lambda_x}\right)_{\mathrm{sf}} = \pi r_0^2 \delta_{\mathrm{gb}}^{-1} L_{\mathrm{gv}}(R,X) \quad \text{and}$$

$$L_{\mathrm{gv}}(R,X) = R^2(1-X^2)$$

for vertical grain boundary diffusion, where δ_{gb} is grain boundary thickness and

$$\left(\frac{a_x}{\lambda_x}\right)_{\mathrm{sf}} = \pi\delta_{\mathrm{gb}} L_{\mathrm{gr}}(R,X) \quad \text{and} \qquad (7)$$

$$L_{\mathrm{gr}}(R,X) = 4$$

for radial grain boundary diffusion.

Material transport rates required for the two processes are the volume changing and grain boundary moving

$$\frac{\mathrm{d}v}{\mathrm{d}t} = -4\pi r_0^2\frac{\mathrm{d}r_0}{\mathrm{d}t} = -4\pi r_0^3\frac{1}{R_0}\frac{\mathrm{d}R_0}{\mathrm{d}t} \quad \text{for grain shrinkage}$$

$$\frac{\mathrm{d}v}{\mathrm{d}t} = -\pi(r-x)^2\frac{\mathrm{d}x}{\mathrm{d}t} = -\frac{2\pi r_0^3 R^3(1-X)}{(2-X)}\frac{\mathrm{d}X}{\mathrm{d}t}$$

for reverse sintering

(8)

From Eqs. (3) and (5)–(8), rate equations for grain shrinkage, $\mathrm{d}R_0/\mathrm{d}t$, and reverse sintering, $\mathrm{d}X/\mathrm{d}t$, are calculated and summarized using the following expressions:

$$\frac{\mathrm{d}R_0}{\mathrm{d}t} = -\left(\frac{\varepsilon_{\mathrm{sf}} D_x V_{\mathrm{m}}}{RT}\frac{1}{r_{0i}^3}\right)\left(\frac{\delta_x}{r_{0i}}\right)^n \frac{1}{R_0^l}\frac{1}{4}L_j(R,X)G_{\mathrm{gs}}(R,X,a)$$

$$\frac{\mathrm{d}X}{\mathrm{d}t} = -\left(\frac{\varepsilon_{\mathrm{sf}} D_x V_{\mathrm{m}}}{RT}\frac{1}{r_{0i}^3}\right)\left(\frac{\delta_x}{r_{0i}}\right)^n \frac{1}{R_0^m}\frac{(2-X)}{2R^3(1-X)}L_j(R,X)G_{\mathrm{rs}}(R,X) \qquad (9)$$

where δ_x is the diffusion layer thickness. Subscripts x and j depend on the types of diffusion. Superscripts n, m and l are exponents on the non-dimensional shape parameters of δ_x/r_{0i} and R_0. In volume diffusion, x and $j = \mathrm{vl}$, $n = 0$, $m = 3$ and $l = 2$; in surface diffusion, x and $j = \mathrm{sf}$, $n = 1$, $m = 4$ and $l = 3$; in vertical grain boundary diffusion for grain growth, $x = \mathrm{gb}$, $j = \mathrm{gv}$, $n = -1$ and $l = 1$; and in radial grain boundary diffusion for reverse sintering, $x = \mathrm{gb}$, $j = \mathrm{gr}$, $n = 1$ and $m = 4$.

4. Numerical calculation of shape parameters and simulation of grain vanishing

4.1. Change of R_0 and X in volume, surface and grain boundary diffusion

We calculated changes in R_0 and X assuming that grain shrinkage and reverse sintering took place simultaneously. We must estimate the diffusion layer thickness for these calculations. Few reports exist on grain boundary thickness in ceramics, either in theoretical or experimental studies [34–38]. Direct TEM observation of polycrystalline SiC materials showed that amorphous grain boundary phases were 0.8 and 1–2 nm thick, and the thickness of boundary segregation of cations in TZP (Tetragonal zirconia polycrystal) was 4–8 nm. A reasonable grain boundary thickness appeared to be 0.5–1 nm [36], so we assumed that δ_{gb} was 1 nm in $Ba_5Nb_4O_{15}$ and fixed $\delta_{\mathrm{gb}}/r_{0i}$ to 1/50 because r_{0i} was approximately 50 nm (Fig. 1 and Table 1). The literature did not provide appropriate values on surface thickness, δ_{sf}. We assumed that surface diffusion thickness was approximately the same as that of the grain boundary, i.e., $\delta_{\mathrm{sf}}/r_{0i}$ was 1/50.

The initial grain at time 0 in Fig. 1 was treated analogously by a truncated sphere with $X = 0.3$. Numerical calculation started from the initial value of $X = 0.3$. Changes in shape parameters X and R_0 are summarized in Fig. 4, plotted against dimensionless time Bt, where $B = (\varepsilon_{\mathrm{sf}} D_x V_{\mathrm{m}}/RTr_{0i}^3)$.

By volume and surface diffusion, grain radius R_0 decreased following convex curves for time, meaning that shrinkage became increasingly rapid as grains became smaller. R_0 suddenly dropped to 0 just before vanishing, corresponding to the TEM observation in Fig. 1.

The effects of grain boundary energy α on rates of shrinkage $\mathrm{d}R_0/\mathrm{d}t$ and reverse sintering $\mathrm{d}X/\mathrm{d}t$ were complicated. The driving force of ΔG_{gs} and ΔG_{rs} depended on α in calculation. The larger the α, the larger ΔG_{gs} and ΔG_{rs}. As X decreased with time, ΔG_{gs} and (a/λ) increased, but ΔG_{rs} decreased. Under the combination of these effects, grains shrank slightly more rapidly with smaller α in volume diffusion, and much more rapidly with larger α in surface diffusion (Fig. 4). $\mathrm{d}X/\mathrm{d}t$ depended on α in both volume and surface diffusion. X decreased more sharply with smaller α. X tended to decrease to -1 under all conditions, indicating that the grain became very thin or flat in the late stage.

By grain boundary diffusion, $\mathrm{d}R_0/\mathrm{d}t$ monotonously diminished and X rapidly decreased compared to the first two types of diffusion. α did not influence both parameter

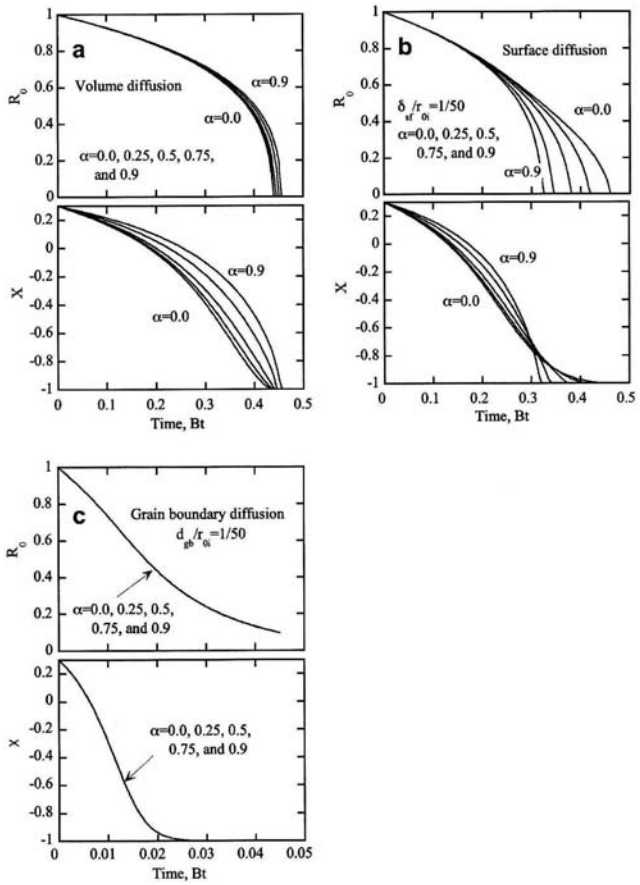

Fig. 4. Changes in shape parameters. R_0 and X are plotted against non-dimensional time Bt, where B is $\varepsilon_{sf} D_s V_m / RTr_{0i}^3$, by (a) volume diffusion, (b) surface diffusion and (c) grain boundary diffusion. Numerical calculation was started from $R_0 = 1$ and $X = 0.3$, varying α from 0 to 0.9.

changes due to the very rapid material transport vertically to the grain boundary, which favors grain shrinkage.

Fig. 5 shows grain shape changes over time from results in Fig. 4a, where material transport proceeded in volume diffusion, and $\alpha = 0.75$. In TEM observation (Fig. 1), however, the actual grain was seen to be somehow round even though it shrank to a very small size. Calculation did not simulate actual grain shape change well.

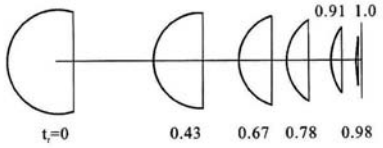

Fig. 5. Shape change until grain vanishing calculated with $\alpha = 0.75$ by volume diffusion. Grain shapes are schematically drawn at relative time t_r to grain vanishing (see Table 1).

4.2. Simulation in combination of volume, surface and grain boundary diffusion

Comparisons of the numerical calculation above with TEM observation indicated to us that grain shrinkage in simulation proceeded much faster than reverse sintering. The shape change did not appear to be simulated by a single diffusion process, but in a combination of volume or surface and grain boundary diffusion. We concluded that the process controlling the rate of grain shrinkage was grain boundary diffusion vertical to the grain boundary, which impedes grain shrinkage, while that for reverse sintering was volume, or surface diffusion.

We first combined the grain shrinkage in vertical grin boundary diffusion and the reverse sintering in volume diffusion by writing the right-hand term of R_0/dt in Eq. (8) as follows:

$$\frac{dR_0}{dt} = -\left(\frac{\varepsilon_{sf} D_{vl} V_m}{RT}\frac{1}{r_{0i}^3}\right)\cdot\left(\frac{D_{gb}}{D_{vl}}\right)\left(\frac{r_{0i}}{\delta_{gb}}\right) \cdot\frac{1}{R_0}\frac{1}{4}L_{gv}(R,X)G_{gs}(R,X,\alpha)$$
$$\frac{dX}{dt} = -\left(\frac{\varepsilon_{sf} D_{vl} V_m}{RT}\frac{1}{r_{0i}^3}\right)\frac{1}{R_0^3}\frac{(2-X)}{2R^3(1-X)}L_{vl}(R,X)G_{rs}(R,X,\alpha) \quad (10)$$

where $IB = (D_{gb}/D_{vl})(r_{0i}/\delta_{gb})$ is the impedance of grain boundary diffusion. The smaller the IB, the less material transported through the grain boundary or the slower the grain growth. Using Eq. (10), we calculated shape parameters of R_0, ps/ps_0, and db/db_0, where ps_0 and db_0 are the initial values (Table 1 and Fig. 1). Calculation was done by fixing $\alpha = 0.75$ and varying IB from 0.01 to 100 (Fig. 6a). Experimental values of these shape parameters calculated from Table 1 are also plotted as circles in the figure. Experimental data of R_0 approximate calculated results for $IB = 1$–100. Those of ps/ps_0 correspond to the curve for $IB = 1$, and those of bl/bl_0, for $IB = 0.1$–10. We concluded from these results that $\alpha = 0.75$ and $IB = 1$ gave the best-fitting curve to experimental data.

We secondly combined the grain shrinkage in vertical grin boundary diffusion and the reverse sintering in surface diffusion. Eq. (10) was rewritten as

$$\frac{dR_0}{dt} = -\left(\frac{\varepsilon_{sf} D_{sf} V_m}{RT}\frac{1}{r_{0i}^3}\right)\left(\frac{\delta_{sf}}{r_{0i}}\right)\cdot\left(\frac{D_{gb}}{D_{sf}}\right)\left(\frac{r_{0i}^2}{\delta_{sf}\delta_{gb}}\right) \cdot\frac{1}{R_0}\frac{1}{4}L_{gv}(R,X)G_{gs}(R,X,\alpha)$$
$$\frac{dX}{dt} = -\left(\frac{\varepsilon_{sf} D_{sf} V_m}{RT}\frac{1}{r_{0i}^3}\right)\left(\frac{\delta_{sf}}{r_{0i}}\right)\frac{1}{R_0^3}\frac{(2-X)}{2R^3(1-X)} \cdot L_{sf}(R,X)G_{rs}(R,X,\alpha) \quad (11)$$

The impedance of grain boundary IB is now $(D_{gb}/D_{sf})(r_{0i}^2/\delta_{sf}\delta_{gb})$. Calculation was done using Eq. (11) and nearly the same results as those from Eq. (10) were obtained (Fig. 6b). The rate of dR/dt and dX/dt did not differ so much between Eqs. (10) and (11), because $L_{vl}(R,X)/L_{sf}(R,X)$ was not large, ranging approximately from 0.5 to 10 for all X. The shape factors did not much affect the calculated results. Fig. 6b shows the calculated shape parameters ps/ps_0 and db/db_0 with $\alpha = 0.9$ and $IB = 0.01$–100 and the experimental values. The results again gave the best-fitting curve to the experimental data with $IB = 1$.

Fig. 7 shows shrinking grains calculated with $\alpha = 0.75$ and $IB = 1$ at each TEM observation. The grain shrank nearly spherically with a truncated base. Numerical calculation simulated the TEM observation in Fig. 1 well.

We next studied the effect of grain boundary energy on shape change. We calculated again by fixing $IB = 1$ and varying α from 0 to 0.9 (Fig. 8). Surface perimeter ps/ps_0 did not differ much with different α. Grain boundary

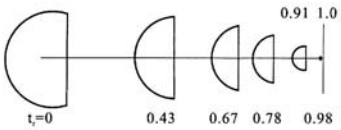

Fig. 7. Shape change until grain vanishing with $\alpha = 0.75$ in combination with the grain shrinkage in vertical grin boundary diffusion and the reverse sintering in volume diffusion. Grain shapes are schematically drawn at relative time t_r to grain vanishing.

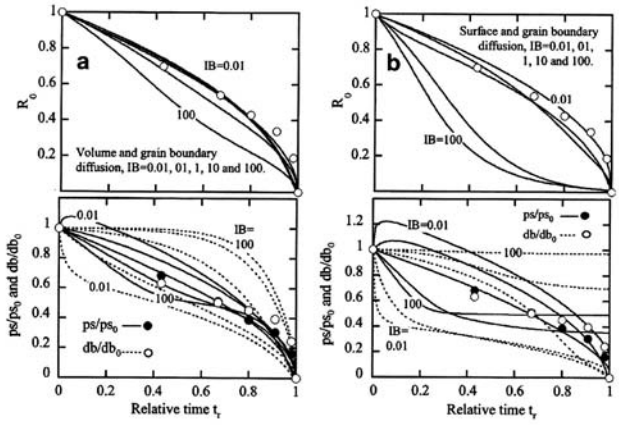

Fig. 6. Changes in shape parameters R_0, ps/ps_0 and db/db_0 calculated (a) in combination with the grain shrinkage in vertical grin boundary diffusion and the reverse sintering in volume diffusion with $\alpha = 0.75$ and $IB = 0.01$, 0.1, 1, 10 and 100 and (b) in combination with the grain shrinkage in vertical grin boundary diffusion and the reverse sintering in surface diffusion with $\alpha = 0.9$ and $IB = 0.01$, 0.1, 1, 10. Solid and dashed lines are calculated data and closed and open circles are experimental data for R_0, ps/ps_0 and db/db_0. These parameters are plotted against relative time t_r to grain vanishing.

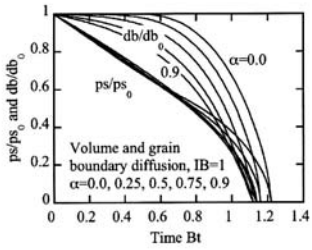

Fig. 8. Effect of grain boundary energy on ps/ps_0 and db/db_0. Grain boundary impedance IB was fixed at 1 and α varied from 0 to 0.9 in the calculations. Time is normalized by B, where B is $\varepsilon_{sd}D_vV_m/RTr_{0i}^3$.

diameter bl/bl_0, however, depended on α, decreasing more sharply with larger α than smaller α. The grain boundary with high energy easily diminished and promoted reverse sintering; in other words, relaxation of grain boundary energy is required in order to stimulate sintering. This result suggests that we must reduce grain boundary energy to consolidate ceramic powder and retard grain growth. Sintering additives often used in ceramic powders may decrease grain boundary energy and promote densification [29,30].

5. Discussion

We observed that very small grains of $Ba_5Nb_4O_{15}$ on a nearly flat matrix shrank and vanished. This phenomenon has been analyzed by sintering two spherical grains with different sizes or sintering a heterogeneous powder compact. The ratios of grain size and grain boundary diffusion to surface diffusion are the most important parameters controlling the sinterability of ceramics. They were first considered by Coble [6,39] with the classical theory. German [40] considered sintering of two grains with different sizes, showing that coalescence was driven by grain boundary curvature. Recently, many details of this phenomenon were simulated using numerical calculation. Pan et al. [18] succeeded well in simulating the coalescence of two grains and Cannon and Carter [41] in formulating a rate equation for sintering of a grain row. Zhang et al. [19] also simulated the coalescence of two grains, showing actual grain coalescence in experiments to examine the validity of the results. They assumed that grain boundary tension and surface tension were determined by the dihedral angle θ satisfying $\gamma_{sf} = 2\gamma_{gb}\cos(\theta/2)$. In this study, the reverse sintering rate equation (Eq. (9)) includes $\alpha = \gamma_{gb}/\gamma_{sf}$ directly and the term of diffusion path (a_x/λ_x) is exactly calculated.

Wakai and Aldinger [24] calculated the coalescence of two grains using the surface evolver program, in which configurations of grains were evolved to minimize surface and grain boundary energy. They also calculated change in the energy in relation to shape change. The Monte-Carlo method and molecular dynamics, mentioned above, were also successfully used to simulate coalescence of two grains [25–28]. The studies indicate that energy stored in a system drives coalescence.

In this study, we assumed that material transport was activated directly by excess free energy, and grain shrinkage and reverse sintering proceeded independently through volume, surface and grain boundary diffusion (Figs. 2 and 3). Calculations using rate equations (Eq. (9)) simulated shrinkage and vanishing of a $Ba_5Nb_4O_{15}$ grain observed on a hot TEM stage (Figs. 6 and 7). Our results enable us to discuss the effect of ratio of grain boundary energy to surface energy and the effect of diffusion paths on grain shape change. These results show that grain boundary energy is quite large and that grain boundary diffusion vertical to the boundary impedes grain growth to maintain round truncated spherical grains. In other cases, grains shrink rapidly, making grains flat.

Parameters α and IB play an important role in our calculations, as shown in the previous section. Grain shape became flatter as α decreased and IB increased. A large α and $IB = 1$ gave the calculation best fitted to TEM observations.

Values of α were estimated here to be 0.75 or 0.9. If α was smaller than these values, the grain boundary did not rapidly disappear as shown in Fig. 8. Uemura et al. [42] roughly estimated that α is 0.98 in a randomly orientated grain boundary of pure SiC bicrystals. The grain boundary can hardly relax surface energy by making grains in ceramics. The appropriate values for α are 0.75 or 0.9 for $Ba_5Nb_4O_{15}$ crystals.

We concluded that the impedance IB of the grain boundary is approximately 1. IB is $(D_{gb}/D_{vl})(r_{0i}/\delta_{gb})$ in a combination of volume and vertical volume diffusions. The grain boundary and surface thickness, δ_{gb}, and the diffusion coefficient of the grain boundary and volume, D_{gb} and D_{vl}, were not measured or known for $Ba_5Nb_4O_{15}$. The values of δ_{gb}/r_{0i} and δ_{sf}/r_{0i} were assumed to be 1/50. This is convincing, given that D_{gb} is 50 times smaller than D_{vl}.

The grain boundary diffusion coefficient was usually larger than that of volume diffusion. Grain boundary diffusion was reported to be from 2–3 to 10 times faster than volume diffusion in oxide crystals and oxide ceramics such as NiO–Al_2O_3, $YBa_2Cu_3O_{7-x}$, ZrO and $La_{1-x}Sr_xFeO_3$ [43–47], and from 3–5 to 10 times faster in SiC and metals [48,49]. We think that the coefficient of grain boundary diffusion may be smaller than that of volume diffusion if the boundary consists of an amorphous structure and has low density. Atomic mobility may be very slow, since atomic jumping sites are rare and the jumping barrier is very high in amorphous structures. Although the atomic structure of the boundary in $Ba_5Nb_4O_{15}$ specimens has not been observed in this study, it appears to be low-density. A low-density grain boundary cannot accommodate surface energy so much, and surface energy is nearly equal to a grain boundary energy corresponding to the results above, i.e., $\alpha = 0.74$

or 0.9. Hanada et al. [50] systematically measured oxygen diffusion in single-crystal and polycrystalline ZnO. The grain boundary diffusion coefficient from 2–3 to 10 times smaller than that of volume diffusion and did not depend on impurity levels. The reason for this is not clear, but the low diffusivity in the grain boundary may be attributed to the amorphous grain boundary structure in polycrystalline material. Such a grain boundary could act as a barrier to material transport in $Ba_5Nb_4O_{15}$ grains and in ZnO. The small $Ba_5Nb_4O_{15}$ grain appears to shrink while keeping its truncated spherical shape due to the impedance effect of the grain boundary and low grain boundary energy.

IB is $(D_{gb}/D_{sf})(r_{0i}^2/\delta_{sf}\delta_{gb})$ in a combination of surface and vertical volume diffusions. The experimental data showed that $IB = 1$. If $r_{0i}/r_{gb} = 50$ and $r_{0i}/r_{sf} = 50$ as we discussed in the previous section, $(r_{0i}^2/\delta_{sf}\delta_{gb})$ is 2500, so that D_{gb} is 2500 times smaller than D_{sf}. Hirota et al. [43] measured the diffusion coefficients of Ni in Al_2O_3 bicrystal and showed that D_{sf} is $8–1.3 \times 10^3$ times larger than D_{gb} at 1400–1700 K. Although the materials are different, their data suggest to us that values of $(r_{0i}^2/\delta_{sf}\delta_{gb}) \gg 1$ and $IB = 1$ are possible in $Ba_5Nb_4O_{15}$ grains. This condition – $(D_{gb}/D_{sf}) \ll 1$ – may be more realistic than values of $(D_{gb}/D_{vl}) \ll 1$ determined from other diffusion data.

In conclusion, grain shrinkage maintaining a hemispherical truncated shape occurred when α was as large as 0.75 and D_{gb} was smaller than D_{vl} or D_{gb} is greatly smaller than D_{sf}. Material transport for grain volume decrease was not faster than that for grain boundary reduction.

We do not take into account vaporization–condensation in grain shrinkage. Grain boundary diameter, *dg*, in Table 1 is not decreased by vaporization of matter from the surface. The shape parameter may change in the same way as that of grain boundary diffusion (Fig. 4c). We can safely rule out that process from the discussion.

6. Conclusions

Very small $Ba_5Nb_4O_{15}$ grains on a nearly flat surface were found to shrink and vanish on a hot stage in TEM. We analyzed the shape change during shrinkage using a new material transport theory in which we postulated that the rate of material transport is proportional to excess free energy in the system, and the diffusion coefficient and effective diffusion area are divided by effective diffusion length. We adopted simple models in which the shape change includes grain shrinkage and reverse sintering, and derived the rate equations of these processes. From these equations, grain shape change by volume diffusion, surface diffusion and grain boundary diffusion was simulated by using the variable of the ratio of grain boundary energy to surface energy. Calculations suggested that grain boundaries were high and that a single diffusion process did not fully simulate shape change. We assumed that the grain boundary impedes grain shrinkage. By combining two independent processes of grain shrinkage by grain boundary diffusion vertical to the boundary and reverse sintering by volume or surface diffusion, we succeeded in simulating the grain shape change. We concluded that grain shrinkage maintaining a hemispherical truncated shape occurred only in cases of high grain boundary energy and high impedance of grain boundary diffusion.

Appendix A

Derivation of Eqs. (5)–(7)

The geometry of the grain in Fig. 2 is given by

$$\begin{aligned}
&\text{volume } v = \frac{1}{3}\pi(r+x)^2(2r-x) = \frac{1}{3}\pi r_0^3 R^3(1+X)^2(2-X)\\
&\text{grain surface } s_{sf} = 2\pi r(r+x) = 2\pi r_0^2 R^2(1+X)\\
&\text{grain boundary surface } s_{gb} = \pi(r^2-x^2) = \pi r_0^2 R^2(1-X^2)
\end{aligned} \tag{A.1}$$

Excess energy per mole for grain shrinkage ΔG_{gs} is calculated as follows:

$$\begin{aligned}
\Delta G_{gs} &= \frac{(s_{sf}\varepsilon_{sf} + s_{gb}\varepsilon_{gb}) - (s_{gb}\varepsilon_{sf} + s_{gb}\varepsilon_{gb})}{\left(\frac{V}{V_m}\right)}\\
&= \frac{(s_{sf} - s_{gb})\varepsilon_{sf}}{\left(\frac{V}{V_m}\right)} = \frac{3\varepsilon_{sf}V_m}{r_0}\frac{1}{R(2-X)}
\end{aligned} \tag{A.2}$$

where

$$(s_{sf} - s_{gb}) = 2\pi r_0^2 R^2(1+X) - \pi r_0^2 R^2(1-X^2)$$
$$\left(\frac{V}{V_m}\right) = \tfrac{1}{3}\pi r_0^3 R^3(1+X)^2(2-X)/V_m$$

Total free energy of the grain, E_{sys} per mole, is

$$E_{sys} = \frac{(s_{sf}\varepsilon_{sf} + s_{gb}\varepsilon_{gb})}{\left(\frac{V}{V_m}\right)} = \frac{3\varepsilon_{sf}V_m}{2r_0}R^2\left\{(1+X) + \frac{1}{2}\alpha(1-X^2)\right\}$$

and differentiating by X under volume $v =$ constant (see model (b) in Fig. 2)

$$\begin{aligned}
\frac{d(E_{sys})}{dX} &= \frac{3\varepsilon_{sf}V_m}{2r_0}\left\{\frac{dR^2(1+X)}{dX} + \frac{1}{2}\alpha\frac{dR^2(1-X^2)}{dX}\right\}\\
&= \frac{3\varepsilon_{sf}V_m}{8r_0}R^5(1+X)^2(X-\alpha)
\end{aligned}$$

where

$$\frac{dR^2(1+X)}{dX} = \frac{1}{4}R^5X(1+X)^2 \quad \text{and} \quad \frac{dR^2(1-X^2)}{dX} = -\frac{1}{2}R^5(1+X)^2$$

E_{sys} has a minimum, $E_{sys,min}$, at $X = \alpha$

$$E_{sys,min} = \frac{3\varepsilon_{sf}V_m}{2r_0}\{2(1+\alpha)^2(2-\alpha)\}^{1/3}$$

The driving force for reverse sintering, ΔG_{rs}, is

$$\Delta G_{rs} = E_{sys} - E_{sys,min} = \left(\frac{\varepsilon_{sf} V_m}{r_0}\right)\frac{3}{2}\left[R^2\left\{(1+X)+\frac{1}{2}\alpha(1-X^2)\right\} - \{2(1+\alpha)^2(2-\alpha)\}^{1/3}\right] \quad (A.3)$$

The terms of the diffusion paths (a_x/λ_x) for the four types of diffusion are derived as follows. In volume diffusion, the material flow from diffusion areas $a_x(x)$ through $a_m(x)$ to grain boundary $a_x(x_{gb})$ (Fig. 3)

$$a_x(x) = \pi(r^2 - x^2), \quad a_x(x_{gb}) = \pi(r^2 - x_{gb}^2) \quad \text{and}$$
$$a_m(x) = \{\pi(r^2 - x^2)\pi(r^2 - x_{gb}^2)\}^{1/2} \quad (A.4)$$
$$\lambda(x) = x_{gb} - x, \quad dv = \pi(r^2 - x^2)dx$$

By integration of Eq. (4) using Eq. (A.4), we get

$$\left(\frac{a_x}{\lambda_x}\right)_{vl} = \frac{4}{3}\pi r_0 \frac{(1-X^2)^{1/2}}{R^2\left\{\frac{1}{2}X^2(1-X^2)^{1/2} + \frac{1}{2}X\arcsin X + \frac{1}{4}\pi X + \frac{1}{3}(1-X^2)^{3/2}\right\}} \quad (A.5)$$

(a_x/λ_x) for surface diffusion is calculated in the same way

$$a_x(x) = 2\pi(r^2 - x^2)^{1/2}\delta_{sf}, \quad dx = \frac{(r^2-x^2)^{1/2}}{r}dl, \quad \lambda(x) = dl$$
$$a_m(x) = 4\pi\delta_{sf}\lambda(x)\left\{\ln\frac{r+x}{r-x} - \ln\frac{r+x}{r_{gb}-x}\right\}^{-1} \quad \text{and}$$
$$dv = 2\pi r\delta_{sf}dx \quad (A.6)$$

Integration of Eq. (4) using Eq. (A.6) yields

$$\left(\frac{a_x}{\lambda_x}\right)_{sf} = \pi\delta_{sf}\frac{2(1+X)}{\ln\frac{2}{(1-X)}} \quad (A.7)$$

In vertical grain boundary diffusion, material flows through the disk of the grain boundary, giving

$$a_x = \pi r_{gb}^2 \quad \text{and} \quad \lambda_x = \delta_{gb} \quad \text{then} \quad \left(\frac{a_x}{\lambda_x}\right)_{gv} = \frac{\pi R^2(1-X^2)}{\delta_{gb}} \quad (A.8)$$

In transversal grain boundary diffusion, material flows along the disk of grain boundary

$$a_x(x) = 2\pi y\delta_{gb}, \quad dx = dy, \quad \lambda(x) = r_{gb} - y$$
$$a_m(x) = 2\pi\delta_{gb}(r_{gb} - x)\Big/\ln\frac{r_{gb}}{x} \quad \text{and} \quad dv = 2\pi y\delta_{gb}dy \quad (A.9)$$

Integration of Eq. (5) using Eq. (A.9) yields

$$\left(\frac{a_x}{\lambda_x}\right)_{gr} = 4\pi\delta_{gb} \quad (A.10)$$

We rewrite Eq. (A.2) to Eq. (5), Eq. (A.3) to Eq. (6), and Eqs. (A.5), (A.7), (A.8) and (A.10) to Eq. (9).

References

[1] Sreemoolanadhan H, Isaac J, Solomon S, Sebastian MT, Jose KA, Mohanan P. Phys Status Solidi 1994;143:K45.
[2] Ratheesh R, Sebastian MT, Mohanan P, Tobar ME, Hartnett J, Woode R, et al. Mater Lett 2000;45:279.
[3] Nakano H, Yano T, Suyama Y. J Ceram Soc Jpn 2005;113:59.
[4] Kuczynski GC. Trans Am Inst Miner Metall Eng 1949;185:169.
[5] Kingery WD, Berg M. J Appl Phys 1955;26:1205.
[6] Coble RL. J Am Ceram Soc 1958;41:55.
[7] Johnson DL. J Appl Phys 1969;40:192.
[8] Ashby MF. Acta Metall 1974;22:275.
[9] Mullines WW. J Appl Phys 1957;28:333.
[10] Nichols FA, Mullins WW. J Appl Phys 1965;36:1826.
[11] German RM, Lathrop JF. J Mater Sci 1978;13:921.
[12] Exner HE, Bross P. Acta Metall 1979;27:1007.
[13] De Jonge LC, Rahaman MN. Acta Metall 1988;36:223.
[14] Zhang W, Schneibel JH. Acta Metall Mater 1995;43:4377.
[15] Svoboda J, Riedel H. Acta Metall Mater 1995;43:1.
[16] Svoboda J, Riedel H. Acta Metall Mater 1995;43:499.
[17] Bouvard D, McMeeking RM. J Am Ceram Soc 1996;79:666.
[18] Pan J, Le H, Kucherenko S, Yeomans JA. Acta Mater 1998;46:4671.
[19] Zhang W, Sachenko P, Schneibel JH, Gladwell I. Philos Mag A 2002;82:2995.
[20] Ross JW, Miller WA, Weatherly GC. J Appl Phys 1981;52:3884.
[21] Jagota A, Dawson PR. Acta Metall 1988;36:2551.
[22] Zhou H, Derby JJ. J Am Ceram Soc 1998;81:533.
[23] Bordia RK, Scherer GW. Acta Metall 1988;36:2393.
[24] Wakai F, Aldinger F. Acta Mater 2003;51:4013.
[25] Matsubara H, Furukawa K, Brook RJ. Fourth Euro Ceram 1995;3:597.
[26] Tikare V, Braginsky M, Olevsky EA. J Am Ceram Soc 2003;86:49.
[27] Tsuruta K, Omeltchenko A, Kalia RK, Vashishta P. Europhys Lett 1996;33:441.
[28] Mazzone AM. Philos Mag B 2000;80:95.
[29] Inomata Y. In: Somiya S, Kanai E, Ando K, editors. First international symposium on ceramic components for engine. Tokyo, KTK Science, 1984. p. 753.
[30] Tanaka H. J Ceram Soc Jpn Int Edit 1995;103:138.
[31] Tanaka H. J Ceram Soc Jpn 1996;104:253.
[32] Tanaka H. J Euro Ceram Soc 2004;24:2763.
[33] Tanaka H. The 123rd meeting of the 124th committee of Japan Society for the Promotion of Science (JSPS), Tokyo, JSPS, 2006. p. 30.
[34] Fisher JC. J Appl Phys 1951;22:74.
[35] Suzuki H, Hase T. J Am Ceram Soc 1980;63:349.
[36] Peterson NL. Diffusion mechanisms in grain boundaries in solids. In: Yan MF, Heuer AH, editors. Advances in ceramics, vol. 6. Columbus (OH): American Ceramic Society; 1983. p. 36.
[37] Tanaka H. Sintering of silicon carbide. In: Somiya S, Inomata Y, editors. Silicon carbide ceramics – I. Elsevier; 1991. p. 213.
[38] Ikuhara Y, Thavorniti P, Sakuma T. Acta Mater 1997;45:5275.
[39] Coble RL. J Am Ceram Soc 1973;56:461.
[40] German RM. Liquid phase sintering. New York (NY): Plenum Press; 1985. p. 101.
[41] Cannon RM, Carter WC. J Am Ceram Soc 1989;72:1550.
[42] Uemura Y, Inomata Y, Inoue Z. J Mater Sci 1981;16:2333.
[43] Hirota K, Komatsu W. J Am Ceram Soc 1977;60:105.
[44] Strelkov AV, Rebane YA, Metlin YG. J Mater Chem 1993;3:735.
[45] Kowalski K, Bernasik A, Sadowski A. J Euro Ceram Soc 2000;20:2095.
[46] Kilo M, Taylor MA, Argirusis CH, Borchardt G, Lesage B, Weber S, et al. J Appl Phys 2003;94:7547.
[47] Wærnhus I, Sakai N, Yokokawa H, Grande T, Einarsrud MA, Wiik K. Solid State Ion 2004;175:69.
[48] Hong JD, Hon MH, Davis RF. Ceram Int 1979;5:155.
[49] Shewmon PG. Diffusion in solid. New York (NY): McGraw-Hill; 1963. p. 164.
[50] Hanada H, Sakaguchi I, Watanabe A, Ishigaki T, Tanaka J. J Electroceram 1999;4(S1):41.

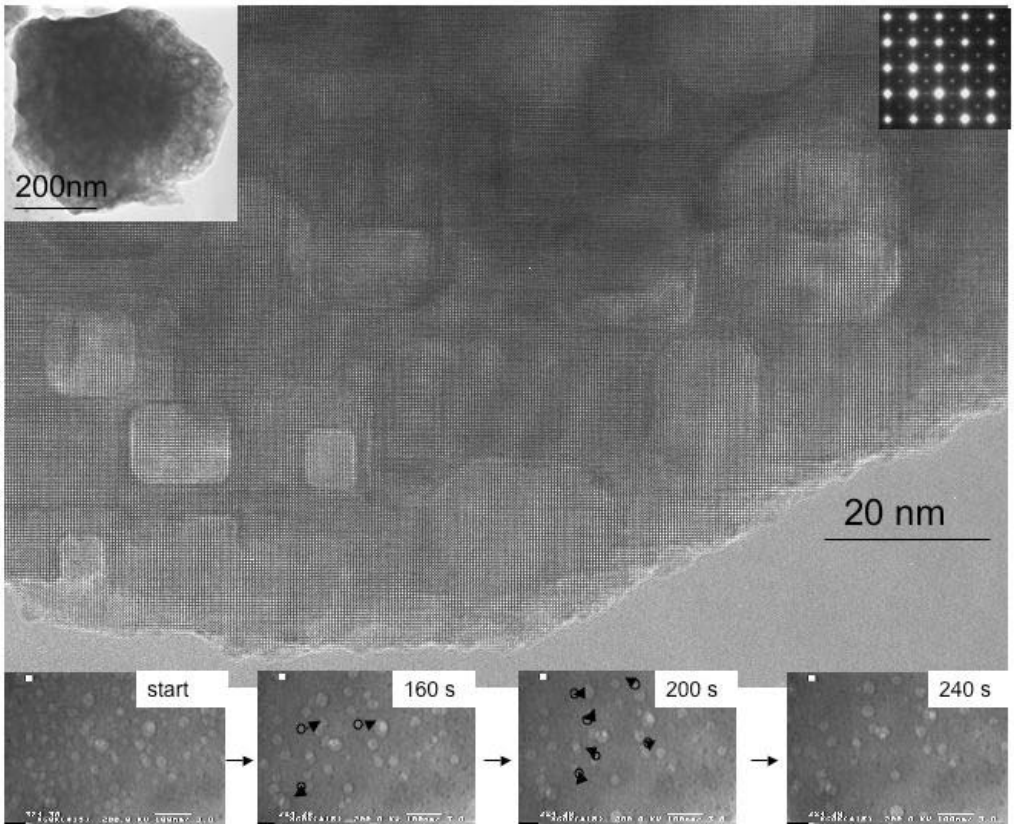

新奇なナノポーラス $NaNbO_3$ 粒子

“出品者所属・氏名：”（龍谷大）中野裕美・（島根大）陶山容子

“撮影者所属・氏名：”（龍谷大）中野裕美

“装置・撮影条件：”JEM-3000F,　JEM-2000EX　2 軸加熱ホルダー

今回、新たに合成した Na-Nb 複合エトキシド結晶を前駆体として $NaNbO_3$ の合成を行ったところ、直線的でユニークな形状のナノサイズの気孔を有するポーラスな $NaNbO_3$ 粒子が形成された。そこで、熱処理による $NaNbO_3$ 粒子の生成過程を詳しく解析し、新奇なナノポーラス粒子の形成プロセスを解明した。

写真は、873 K で 90 分間熱処理後に得られた試料で、X 線回折および電子回折により $NaNbO_3$ の単結晶粒子（斜方晶（*Pbcm*））であることが分った。粒子サイズは約 500 nm で、粒子内部に様々なサイズの気孔（＜50 nm）が観察される。高分解能写真は[001]方向からのもので、格子縞に沿って気孔が形成されている様子がわかる。これらの気孔は非晶質時には球状に近いが、結晶化にともない結晶形に沿って整形され、角が鋭角にならないのも特徴である。下部の 4 枚の写真は、Na-Nb 複合エトキシドを 623 K で前処理して、エトキシ基の分解を終了させた後の非晶質 $NaNbO_3$ 試料を用い、非晶質から結晶化過程における気孔の挙動を高温 TEM によりその場観察し、ビデオにより記録したものである。723 K で多結晶リングが観察され結晶化が開始したことを確認できたので、723 K で温度を保持してその場観察を行った。約 20 nm サイズの気孔が動き始め、矢印で示すように大きな気孔と合体したり、また試料外に消えたりしながら 240 秒後には観察領域全体が単結晶を示す電子回折パターンを示した。気孔の移動速度は約 10 nm/sec で、より小さい気孔はさらに早く移動し、複雑な動きで 150 nm 程度移動する様子も観察された。しかしながら、723 K では温度が低いため粒成長は起こらず、粒子内部に多くの気孔が取り残されたままで結晶性の良い粒子が形成された。この結果、ナノポーラス粒子が形成されたものと考えられる。結晶粒子中の残留気孔は、水熱合成 $BaTiO_3$ でも特徴的に見ることができ、稀に結晶形を反映した気孔も観察される。水熱合成 $BaTiO_3$ 中の気孔の形成について、その詳細なメカニズムは明らかになっていないが、今回の結果が解明の糸口になると考える。

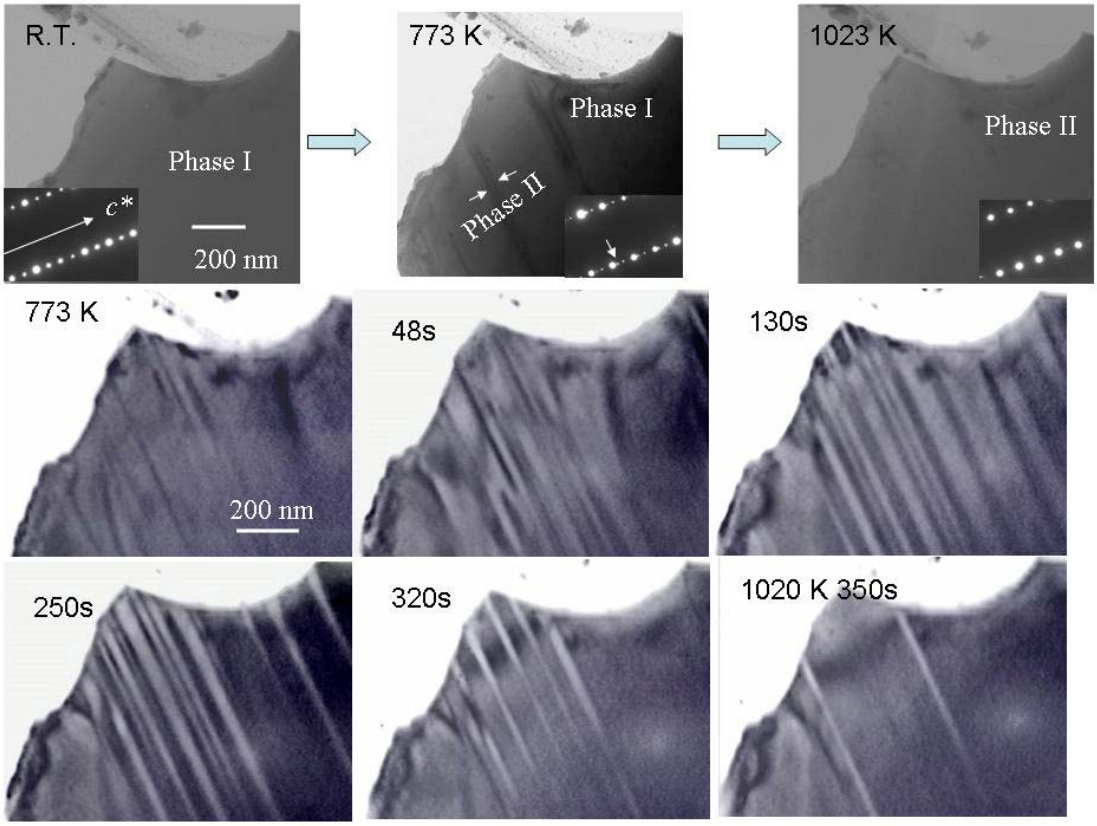

層状ペロブスカイト $BaGd_2Mn_2O_7$ の一次相転移その場観察
-高温相の出現から単一相に至るまでの変化-

“出品者所属・氏名：”（龍谷大）中野裕美・石沢伸夫・亀頭直樹

“撮影者所属・氏名：”（龍谷大）中野裕美

“装置・撮影条件：” JEM-2000EX, 200 kV　高温２軸ホルダー

$BaGd_2Mn_2O_7$（Ln =希土類）は、$AO(ABO_3)_2$ で表される Ruddlesden-Popper 型の homologous 化合物に属し、層状構造を有する。この酸化物は熱処理条件によって多くの相が発現する。今回、FZ 法による単結晶を用い、透過型電子顕微鏡(TEM)の 2 軸傾斜用高温ホルダーを使用して、構造相転移のその場観察を行った。室温で $P4_2/mnm$ (Phase I)の構造を有する $BaGd_2Mn_2O_7$ は、623 K 付近で基本反射の低角側に弱い反射が出現し始めた。これは、高温相(Phase II)が Phase I に比べて c-軸方向に約 1.5%程度大きい格子をもつことを意味し、Phase I と Phase II が同時に存在することから一次相転移であると推定された。773 K の TEM 像では、Phase II が層状に挿入されることが観察された。1023 K では、観察粒子は Phase II の単一相になり、電子回折図形にも明らかな変化が現れている。層状に出現した Phase II が Phase I を徐々に駆逐し、1023 K 以上で単一相になるまでの変化を動画から切り取り、６枚の写真で示す。昇温スピードは約 0.7 K/s で、昇温と共に、黒いコントラスト(Phase II)の領域が増加し、結晶全体に広がって行く様子が観察された。他の方位による解析の結果、Phase II は単斜晶系相の可能性を示唆した[1]。構造変化の理由として、岩塩層とペロブスカイト層の間のひずみの増加や、Mn 価数の変化とヤーンテラー効果との関連性などが考えられる。この一次相転移はこれまでに報告例がないが、同様の相転移が他の層状マンガナイトにも起きる可能性がある。

1）H. Nakano et al. J. Am. Ceram. Soc. 90(4)1342 (2007)